Imperial College London
Department of Electrical and Electronic Engineering

'THz Torch' Wireless Communications Links

Hang Ren

October 2020

Submitted in part fulfilment of the requirements for
the degree of Doctor of Philosophy in
Electrical and Electronic Engineering of Imperial College London and
the Diploma of Imperial College London

Abstract

The low-cost 'THz Torch' technology, which exploits the thermal infrared spectrum (*ca.* 10 to 100 THz), was recently introduced to provide secure low data rate communications links across short ranges. In this thesis, the channel model for 'THz Torch' wireless communications links is redeveloped from a thermodynamics perspective. Novel optimization-based channel estimators are also proposed to calibrate parameters in the channel model. Based on these theoretical advances, a cognitive 'THz Torch' receiver, which combines conventional digital communications with state-of-the-art deep learning techniques, is presented to achieve cognitive synchronization and demodulation. The newly reported 'THz Torch' wireless link is capable of bypassing the thermal time constant constraints normally associated with both the thermal emitter and sensor, allowing truly asynchronous data transfer with direct electronic modulation. Experimental results obtained in both laboratory environments and field trials demonstrate step-change improvements in channel range, bit rate, bit error rate and demodulation speed.

This work represents a paradigm shift in modulation-demodulation with a thermal-based physical layer and offers a practical solution for implementing future ubiquitous secure 'THz Torch' wireless communications links. The cognitive receiver concept also has wide-ranging implications for future communications and sensor technologies, making them more resilient when operating in harsh environments.

Statement of Originality

To the best of my knowledge and belief, the thesis contains no material previously published or written by another person except where due reference is made in the thesis itself. The research presented in the thesis is conducted by myself from Oct. 2016 to Oct. 2020, under the supervision of Prof. Stepan Lucyszyn.

Copyright Declaration

The copyright of this thesis rests with the author. Unless otherwise indicated, its contents are licensed under a Creative Commons Attribution-Non Commercial 4.0 International Licence (CC BY-NC). Under this licence, you may copy and redistribute the material in any medium or format. You may also create and distribute modified versions of the work. This is on the condition that: you credit the author and do not use it, or any derivative works, for a commercial purpose. When reusing or sharing this work, ensure you make the licence terms clear to others by naming the licence and linking to the licence text. Where a work has been adapted, you should indicate that the work has been changed and describe those changes. Please seek permission from the copyright holder for uses of this work that are not included in this licence or permitted under UK Copyright Law.

Acknowledgements

First, I would like to thank my supervisor, also my friend, Prof. Stepan Lucyszyn, for guiding me through this wonderful journey. Without the knowledge, patience, and encouragement from him, I will not be able to accomplish this work and finally reach this milestone.

Also, I would like to thank my colleagues and staff from the Electrical and Electronics Department, Imperial College London. They are Dr. Jingye Sun, Mr. Sang-Hee Shin, Mr. Liyan Zhu, Mr. Mayue Shi, Prof. Andrew Holmes, Dr. Munir M Ahmad, Ms. Susan Brace, Dr. Zahid Durrani, Dr. Dixi Liu, Mr. Victor Boddy, Ms. May Tang and Dr. Guangbin Dou. Many thanks for their help during my Ph.D.

Special thanks to the China Scholarship Council and Imperial College London for my joint Ph.D. scholarship.

Finally, I would like to sincerely thank my family, my wife Yuan Liang, my father Gang Ren, my mother Hua Ji, for their endless love and support.

Contents

Abstract **3**

Statement of Originality **3**

Copyright Declaration **7**

Acknowledgements **9**

1 Introduction **31**

1.1 Motivation and Objectives 31

1.2 Contributions 32

1.3 Outline of the thesis 33

2 Literature Review **35**

2.1 Terahertz and Infrared Technologies 35

2.1.1 Terahertz and Infrared Enabling Technologies 36

2.1.2 Terahertz and Infrared Systems and Applications 43

2.2 Machine learning in communications 48

2.2.1 Problems solved by machine learning 48

2.2.2 Deep learning 49

2.2.3 Machine learning in communications 51

3 Channel Architecture and Modelling **53**

3.1 Channel Architecture 53

3.1.1 Laboratory Experimental Setup 54

3.1.2 Non-laboratory Experimental Setup 57

3.1.3 Software Architecture 58

3.2 Channel Modelling 59

3.2.1 OOK Modulated Thermal Infrared Emitter 59

3.2.2 Free Space Transmission 67

3.2.3 Pyroelectric Sensor 68

3.2.4 Thermal Emitter Estimator 73

3.3 Noise Analysis 84

3.3.1 Intrinsic Noise 84

3.3.2 Environmental Noise 91

3.3.3 Noise Reduction 91

3.4 Summary 93

4 Cognitive 'THz Torch' Receiver **95**

4.1 Receiver Architecture 95

4.2 Cognitive Synchronization and Demodulation 97

4.2.1 Framework 97

4.2.2 Naive Template Matching 100

4.2.3 Matched Filter 104

4.2.4 Synchronization under Parameter Mismatch 108

4.2.5 LSTM-based Demodulator 111

4.3 Performance 118

4.3.1 Enhanced performance demonstration 118

4.3.2 Bit Error Rate 121

4.4 Summary 124

5 Conclusion and future work **126**

5.1 Summary of thesis achievements 126

5.2 Future work 127

5.3 Publications from this work 130

References **130**

Appendix **149**

List of Tables

3.1 Band-pass filter specifications. The aperture blockage is calculated with reference to an unblocked circular filter having diameter $\varnothing = 9$ mm. 55

3.2 U.S. Standard 1976 mean-latitude sea-level atmosphere model 67

3.3 Parameters for estimating the output voltage noise spectral density 89

4.1 Implementation and performance summary comparisons of reported 'THz Torch' wireless links 125

List of Figures

2.1 Electromagnetic spectrum with frequency bands and corresponding applications (adapted from [21]). 36

2.2 The typical architecture of photonics-based THz sources [42]. 38

2.3 Specifications of electronics and photonics CW THz sources (adapted from [24]). 39

2.4 The typical architecture of a terahertz time-domain transmission spectroscopy (TDS) system [98]. 43

2.5 Block diagrams of typical THz CW transmitters and receivers (adapted from [92]). 45

2.6 Markov decision process framework for reinforcement learning [124]. 50

2.7 Block diagram for a typical digital communications system [133]. 51

3.1 Typical 'THz Torch' wireless link. (**a**) Architecture. (**b**) Laboratory experimental setup with a range of 2 m. 56

3.2 Practical field trials for a 2 m 'THz Torch' wireless link. The insert in the lower figure shows the thermal image of the transmitter's front-end hardware with the thermal emitter in the ON-state (the cross-hairs from the camera indicate the centre of the Tx lens). 57

3.3 Software architecture diagram for the 'THz Torch' transceiver. 58

3.4 Measured angular distribution of radiation and fitted Lorentzian curve. . . 60

3.5 Channel characterization. (**a**) Theoretical thermal emitter power spectral density, measured channel band-pass filter and lens transmittance responses, and simulated free-space transmittance across the 2 m link under pristine conditions. (**b**) Predicted mean channel transmittance against range, using equation (3.11). (**c**) Theoretical radiated power within the channel filter passband, using equation (3.4), for a steady-state emitter temperature of 1,023 K; step incident power, using equation (3.20) with $L_c = 1$; and the resulting channel implementation efficiency. 61

3.6 Thermal emitter (**a**) Top-view illustration. (**b**) Side-view illustration with heat transfer mechanisms indicated. (**c**) Photograph with the filter and cone reflector removed. (**d**) Photograph with the filter, cone reflector and thin-film membrane removed. 62

3.7 Calculated ideal thermal emitter (INTX 17-0900) responses. (**a**) Transient turn-ON behaviour of emitter temperature, with 898 mW of emitter DC power, from OFF-state at 20 °C ambient room temperature. (**b**) Time-variant power spectral density of thermal radiation corresponding to Figure 3.7a at 10 ms intervals. (**c**) Transient behaviour for both emitter temperature and radiated power (using piecewise power series) for a '10101' transmitted symbol sequence when modulated at 100 baud, from OFF-state at ambient room temperature. (**d**) Time-variant power spectral density of thermal radiation corresponding to Figure 3.7c at 10 ms intervals. 66

3.8 Pyroelectric infrared sensor (LME-335): (**a**) Equivalent circuit model for all components integrated within the sensor. (**b**) Measured and fitted sensor step response demonstrated for the 2 m single-channel 'THz Torch' wireless link. The incident radiation step excitation is generated by the mechanical shutter and the thermal emitter at its steady-state temperature of 1,023 K. 68

3.9 Contour plot of the mean-square-error (MSE) function applied for sensor estimation. Here, p_1 and p_2 are not shown for visualization purposes. With the initial values (indicated by the red triangle), the error function is locally convex, and the Levenberg-Marquard algorithm converges to the optimal sensor parameters (indicated by the white triangle) in only four iterations. 72

3.10 Thermal emitter estimation demonstrated for the 2 m single-channel 'THz Torch' wireless link using Algorithm 1 with finite difference: (**a**) Contour plot of the error function in equation (3.22) that depends on W_R and C_e (k_e is fixed to 1.03×10^{-3} W/K for visualization purposes). Optimization progress of the gradient descent and the Newton-Raphson method are indicated by the triangular and circle markers, respectively. (**b**) Synchronized received noisy signal with two expected noiseless signals that adopt the initial and optimized emitter parameter values. For each noiseless expected signal, the absolute error $|error|$ between the expected and measured signals are also shown. For visualization purposes, this is scaled from $-2 \times |error|$ to $+2 \times |error|$. 77

3.11 Thermal emitter estimation demonstrated for the 2 m single-channel 'THz Torch' wireless link using Algorithm 1 with the evolution strategy: (**a**) Contour plot of the error function in equation (3.22). Optimization progress of the gradient descent and the Newton-Raphson methods are indicated by the triangular and circle markers, respectively. (**b**) Synchronized received noisy signal with two expected noiseless signals that adopt the initial and optimized emitter parameter values. For each noiseless expected signal, the absolute error $|error|$ between the expected and measured signals are also shown. For visualization purposes, this is scaled from $-2 \times |error|$ to $+2 \times |error|$. 83

3.12 External Back-end circuit of the PIR sensor. (**a**) Circuit schematic. (**b**) Four-layer PCB layout. 85

3.13 Electrical equivalent circuit models for intrinsic noise analysis. 86

3.14 (**a**) Calculated output voltage noise spectral density. The noise component $U_{V_{VF}}$ has a low spectral density (not plotted here). (**b**) Measured output voltage noise spectral density from [164]. 90

3.15 Measured noise and associated single-sided amplitude spectral density (dashed red lines indicate different symbol rates) in different environments. (**a**) Inside an electromagnetically-shielded microwave anechoic chamber. (**b**) Large air-conditioned room. (**c**) Outdoors. 92

3.16 Measured background noise over a 1 second period in the laboratory environment with PIR sensor shrouded. (**a**) output noise voltage. (**b**) associated single-sided amplitude spectral density. The red plots represent unfiltered measurements and the blue plots represents the addition of an anti-aliasing filter, inserted between the sensor back-end circuits and ADC, having a cut-off frequency of 2.5 kHz. 93

4.1 Block diagram for the 'THz Torch' transceiver architecture. 96

4.2 Demodulation using the naive template matching algorithm demonstrated for the 2 m single-channel 'THz Torch' wirless link. The transmitted data frame, including the fixed preamble, is a '111010100010' symbol sequence sent at 100 baud. (**a**) Expected thermal emitter temperature, using equation (3.6). (**b**) Expected normalized incident power at the PIR sensor, using equation (3.21). (**c**) Expected received noiseless signals (black for $v_{S0}^{s_1:(i-1)}[t]$ and red for $v_{S1}^{s_1:(i-1)}[t]$) and received signal with noise (blue). The resulting demodulated symbol sequence shows no errors. 103

4.3 Matched filter hypotheses in signal spaces. (**a**) One dimensional signal space for synchronization. (**b**) Two dimensional signal space (varying from symbol to symbol) for demodulation. 105

4.4 Timing synchronization for predefined training signals demonstrated for the 2 m single-channel 'THz Torch' wireless link. The naive template matching (NTM) objective in equation (4.8) and the matched filter (MF) objective in equation (4.12) are scaled and shifted to $[-1, 0]$ for visualization purposes. Each time delay estimation, indicated by a vertical dashed line, is obtained by locating the peak of its corresponding objective function. (**a**) Timing synchronization for PIR sensor estimation. The training sequence is a radiation step and the training signal is the step response of the sensor. (**b**) Timing synchronization for thermal emitter estimation. The training sequence includes four leading $S1$ followed by twenty $S0$, over 480 ms, sent at 50 Baud. (**c**) Timing synchronization for data frame. The training sequence is a fixed data frame preamble $\{S1, S1, S1, S0\}$, with random data following on. 107

4.5 Improved timing synchronization using change-point detection demonstrated on the 2 m single-channel 'THz Torch' wireless link. Compared with Figure 4.4a&b, the expected noiseless signal (training signal) in orange is produced by the mismatched emitter and sensor parameters. The coarse time delay δ_{tm} decided by the template-matching phase is indicated by the red dashed line. Black stars represent the detected five change points $\{\mathcal{I}_k^v\}_{k=1}^5$, and the black dashed line indicates the improved timing synchronization δ_{cp} after the change-point detection phase. (**a**) Timing synchronization for initial PIR sensor estimation. The training sequence is a step radiation and the training signal is the step response of the sensor. (**b**) Timing synchronization for initial thermal emitter estimation. The training sequence includes four leading $S1$ followed by twenty $S0$, over 480 ms, sent at 50 Baud. . . . 110

4.6 Unrolled computational graph for the complete LSTM-based cognitive demodulator with emitter and sensor parameter inputs and received noisy signal (cyan curve) input across a sequence of N symbols. 113

4.7 Training curve of a LSTM-based demodulator (**a**) Evaluated cross-entropy loss on training, validation and test datasets after each epoch. (**b**) Evaluated BER on training, validation and test datasets after each epoch. 116

4.8 Signal space decision boundaries for the LSTM-based demodulator (between the two colours) and the matched filter (green dashed line, mid-perpendicular of the line segment through $S0$ and $S1$). 117

4.9 Operation of demodulation demonstrated for the 2 m single-channel 'THz Torch' wireless link field trial. (**a**) NTM with initial thermal emitter parameters (16 symbol errors). (**b**) NTM with estimated thermal emitter parameters (7 symbol errors). (**c**) MF with initial thermal emitter parameters (9 symbols errors). (**d**) MF with estimated thermal emitter parameters (error free). The LSTM-based demodulator with and without estimated thermal emitter parameters (error-free) is also shown in (c)(d). Here, the LSTM-based demodulator is only trained on the simulated dataset without any fine-tuning using data from the real system. 120

4.10 Measured BER performance for the single-channel 2 m link in a laboratory environment with optical bench and precision alignment rails, as shown in Figure 3.1b. 121

4.11 Measured BER performance for the single-channel 2 m link in a non-laboratory environment (office corridor) with laser alignment, as shown in Figure 3.2. 122

4.12 Measured NTM BER performance for the multi-channel 0.5 m link in a laboratory environment with optical bench and precision alignment rails, as shown in Figure 3.1b. 123

5.1 Empirical $v_s(f)$ of the expected noiseless received signal under different symbol rates. 128

List of Symbols

Thermal Emitter

ϵ	emissivity	
λ	wavelength in free space	m
σ_e	Stefan-Boltzmann constant	$5.670 \times 10^{-8}\, W \cdot m^{-2} \cdot K^{-4}$
A_e	heated film area	m^2
c	speed of light in free space	$2.997 \times 10^{8}\, m/s$
C_e	emitter heat capacity	J/K
h	Planck constant	$6.626 \times 10^{-34}\, J \cdot s$
I	radiated spectral density	$W/Hz/sr/m^2$
k_B	Boltzmann constant	$1.381 \times 10^{-23}\, J/K$
k_e	emitter thermal conductance	W/K
P_e	radiated power	W
p_e	radiated power spectral density	W/Hz
T	emitter temperature	K
t	time	s

T_0	ambient temperature	K
T_s	steady-state temperature	K
W_e	emitter input power	W
W_R	emitter rated input DC power	W

Free Space Transmission

$\mathcal{T}_a$	atmospheric transmittance	
$\mathcal{T}_c$	mean channel transmittance	
$\mathcal{T}_f$	BPF transmittance	
$\mathcal{T}_f$	lens transmittance	
L_c	frequency-independent transmission losses	
R_c	channel range	m

Pyroelectric Sensor

η_p	absorptance of the absorption layer	
$\hat{P}_{RX}$	normalized incident radiated power	
A_p	surface area of the pyroelectric layer	m^2
C_{fb}	feedback capacitor	F
G_p	sensor thermal conductance	W/K
H_p	sensor heat capacity	J/K
i_{fb}	feedback current	A
p	pyroelectric coefficient	$C/K/m^2$

P_{RX}	incident radiated power	W
P_{step}	power of the step incident radiation	W
R_{fb}	feedback resistor	Ω
T_p	sensor temperature	K
v	sensor output voltage	V

Other Symbols

s_i	the $i-$th symbol	
T_S	number of samples per symbol	
v_n	noise signal	V
v_s	expected noiseless signal	V
v_{train}	training signal	V

Noise

C_d	sensor capacitance	C
C_p	capacitance equivalent to the sensor heat capacity H_p	C
C_{TIA}	input capacitance of the TIA amplifier	C
I_p	noise current equivalent to the thermal fluctuation noise	$A/\sqrt{Hz}$
I_{TIA}	input noise current of the TIA amplifier	$A/\sqrt{Hz}$
R_p	resistance equivalent to the sensor thermal conductance G_p	Ω
R_{TIA}	input resistance of the TIA amplifier	Ω

$tan\delta_d$ sensor loss tangent

V_{TIA} input noise voltage of the TIA amplifier $V/\sqrt{Hz}$

V_{VF} input noise voltage of the voltage follower $V/\sqrt{Hz}$

Acronyms and Abbreviations

ADC analogue-to-digital converter

AFM atomic force microscopy

ASK amplitude-shift keying

BER bit error rate

BPF bandpass filter

BPTT backpropagation through time

CNN convolutional neural network

CW continuous wave

DFG difference frequency generation

EM electromagnetic

FETs field-effect transistors

HBTs heterojunction bipolar transistors

HEMTs high-electron mobility transistors

I.I.D. independent and identical

LDO low-dropout

LEDs light-emitting diodes

LSTM long-short term memory

MAE mean-absolute-error

MAP maximum a posterior

MDP Markov decision process

MEMS micro-electromechanical systems

MF matched filter

MIMO multiple-input-multiple-output

MLP multi-layer perception

MSE mean-square-error

NN neural network

NTM naive template matching

OOK ON-OFF keying

PCB printed circuit board

PIR pyroelectric infrared

PSD power spectral density

QAM quadrature amplitude modulation

QCL quantum cascade laser

QPSK quadrature phase-shift keying

RNN recurrent neural network

RTD resonant tunnel diode

TDS time-domain spectroscopy

THz terahertz

TIA transimpedance amplifier

USART universal synchronous asynchronous receiver transmitter

USB universal serial bus

UTC uni-travelling-carrier

VCCS voltage-control-current-source

WGN white Gaussian noise

Chapter 1

Introduction

1.1 Motivation and Objectives

Wireless links represent the fastest growing area within the digital communications industry. The history of transmitting data wirelessly can be traced back to ancient China, using smoke signaling for long-distance communication. Other early examples of wireless communications include optical telegraphy (Heliography) from the 19th century and photophone in the early 20th century [1]. Today, wireless communications systems play a crucial role in every aspect of human life.

Modern wireless communications systems can be found in most parts of the electromagnetic (EM) spectrum; at radio frequencies that extend upwards into the far-infrared (i.e., covering the microwave [2], millimeter-wave [3] and terahertz bands [4, 5]) and at optical wavelengths that extend downwards (i.e., across the visible light spectrum [6] into the near-infrared [7]). However, little research and development have been reported on thermal infrared (i.e., around the far-infrared and mid-infrared bands, having atmospheric transmission windows from 20-40 THz and 60-100 THz) wireless communications links. Until recently, the thermal infrared spectrum has been generally confined to applications

that include motion sensing, target acquisition [8] and thermography [9] (e.g., digital thermometers and thermal cameras); having relatively low-cost components that work with incoherent radiation, when compared to extremely expensive components used in coherent systems [10] operating at radio frequencies and optical wavelengths.

The first thermal infrared wireless communications system, known as the 'THz Torch', was first introduced in 2011 [11]. The philosophy behind this technology is to implement a secure and robust communications channel, while being extremely low cost – making it affordable for future ubiquitous applications. Here, the thermal-based physical layer hardware consists of a transmitter (employing miniature incandescent light bulbs or thermal emitters) and receiver (employing pyroelectric infrared (PIR) motion sensors) that supports wireless data transfer via a modulated noise carrier. The same group then went on to investigate various aspects associated with the 'THz Torch' technology, from system-level architectures down to device level enabling technologies, while trying to maintain the low-cost philosophy [12–18].

However, the low-cost 'THz Torch' wireless link is still in its infancy. Until very recently, inherent limitations with available hardware have resulted in a modest operational figure of merit (range $\times$ bit Rate) and high bit error rate (BER) that can not support any real application. This work dedicates to significantly improve the performance of the 'THz Torch' wireless link by redeveloping the channel model and designing a cognitive 'THz Torch' receiver.

1.2 Contributions

The primary outcome of this work is a practical solution for future ubiquitous secure 'THz Torch' wireless links. Theoretical and experimental contributions of this work can be summarized as follows:

Theoretical contributions

- A channel model for the 'THz Torch' wireless link based on thermodynamics.
- A cognitive 'THz Torch' receiver includes a timing-synchronizer which is resilient to parameter mismatch, a channel estimator, and a deep learning-based demodulator.
- A gradient-free optimization algorithm for channel estimation, which can be scaled-up for high-dimensional complex systems.

Experimental contributions

- A re-implementation of the 'THz Torch' hardware and two experimental setups in the laboratory and non-laboratory environments.
- A user interface and modulator driver for the 'THz Torch' transmitter.
- A multi-processing software for the cognitive 'THz Torch' receiver, which supports real-time data transfer and BER measurement.

1.3 Outline of the thesis

The thesis is organized as follows:

- Chapter 1 introduces the background and motivation of this work and summarizes our main contributions.
- Chapter 2 first reviews THz and infrared technologies that include enabling technologies and developed systems. Previous works on 'THz Torch' wireless links are surveyed in a standalone subsection. The second half of this chapter covers the

machine learning methods and their applications in digital communications, which inspire our cognitive 'THz Torch' receiver design.

- Chapter 3 introduces the thermodynamics-based channel model. The dynamic models of the thermal emitter and PIR sensor, under fast modulation, are built. A novel estimator for channel model parameters is also presented, which serves as an indispensable block in the cognitive receiver. The free space propagation and noise mechanism are also investigated to complete our channel modelling.

- Chapter 4 introduces the cognitive 'THz Torch' receiver architecture. Following the classic hypothesis test framework, two template-matching based algorithms are proposed for timing synchronization and demodulation. A change-point detection method is exploited to improve the synchronization under parameter mismatch. A deep learning-based demodulator is also reported, which achieves fast and accurate demodulation. Finally, enhanced performances of the cognitive receiver are demonstrated experimentally.

- Chapter 5 concludes the thesis and proposes ideas for future research.

Chapter 2

Literature Review

2.1 Terahertz and Infrared Technologies

To avoid ambiguity, we first clarify all the frequency bands within our scope and regulate their corresponding ranges in the electromagnetic spectrum. As shown in Figure 2.1, the terahertz (THz) band covers the electromagnetic radiations from 300 GHz to 10 THz. However, both the lower and upper bound of this band are controversial and may vary between regulations and academic communities [19, 20]. The lower end of the terahertz band, from 300 GHz to 3 THz, is also known as the submillimeter band. The infrared band, whose lower end overlaps with the higher end of the terahertz band, ranges from 300 GHz to 400 THz. It can be further divided into three sub-bands: the far-infrared band from 300 GHz to 30 THz, the mid-infrared band from 30 to 120 THz, and the near-infrared band from 120 to 400 THz. The 'THz Torch' communications link reported in this work exploits broadband noise carriers ranging from 20 to 80 THz, spanning over the far-infrared and mid-infrared bands. The name of this technology, 'THz Torch', inherits from pioneering works on this topic [13–15] where the thermal infrared band covering high-THz frequencies from 10 to 100 THz is explicitly defined. The visible band ranges

from 400 to 750 THz, where most LED and laser technologies fall into.

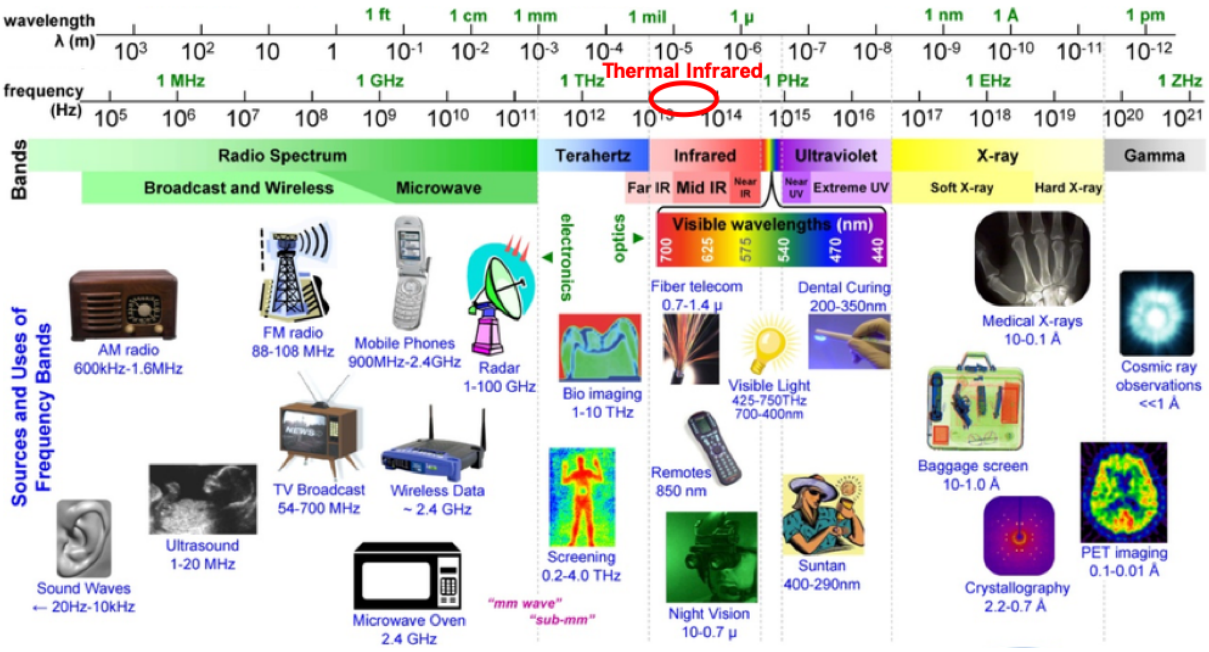


Figure 2.1: Electromagnetic spectrum with frequency bands and corresponding applications (adapted from [21]).

This section mainly reviews enabling technologies and applications which fall into the terahertz and infrared bands. Principles for the generation and detection of electromagnetic radiations are firstly investigated. Various active and passive components are then discussed as indispensable building blocks for manipulating the radiation. Finally, we survey both commercial and experimental applications, focusing on the 'THz Torch' system closely related to this work.

2.1.1 Terahertz and Infrared Enabling Technologies

Terahertz and infrared radiations can be categorized by following different criteria. According to the signal duration in the time domain, they can be divided into continuous-wave (CW) and pulse. Based on their frequency purity, radiations can be either monochromatic or polychromatic. Besides, radiations can be naturally divided into each band ac-

cording to their centre frequency. This section reviews terahertz and infrared enabling technologies from three aspects: sources for radiation generation [22], sensors for radiation detection [23], and passive components for radiation manipulation. Each topic is organized by the technologies' underlying mechanisms and the main radiation categories they deal with.

Sources

Solid-state electronics based on silicon and III-V semiconductors (such as InP, GaAs, and GaN) play an important role in generating monochromatic continuous-wave radiations in the lower terahertz band. These technologies are directly extended from the well-developed oscillator technologies in microwave and millimeter wave bands. Its inherent advantages include room-temperature operation, high compactness, and relatively low-cost [24]. In the past decade, both the power level and frequency of electronic THz sources have been significantly improved. High-performance III-V semiconductor transistors, such as InP heterojunction bipolar transistors (HBTs) [25–27], and high electron mobility transistors (HEMTs) [28], are employed in state-of-the-art THz sources and capable of maintaining a milliwatt power level above 500 GHz. One port diodes, having negative resistance, are competitive alternatives to high-frequency transistors [29]. Commonly used diodes include resonant tunnel diode (RTD) [30–32] and Gunn diode [33, 34]. Diode-based sources are able to generate radiations above 1 THz with a relatively lower power level below 100 microwatts. Silicon technology was meant to operate at lower frequencies. However, Recent progress on SiGe and bipolar-CMOS (BiCMOS) [35–37] makes it a reliable option with a higher level of integration below 500 GHz. Another approach for generating THz radiation is exploiting frequency multipliers to shift sub-THz oscillations into the target band. Conventional frequency multiplier implementations rely on Schottky diodes [38–40] and CMOS devices [41].

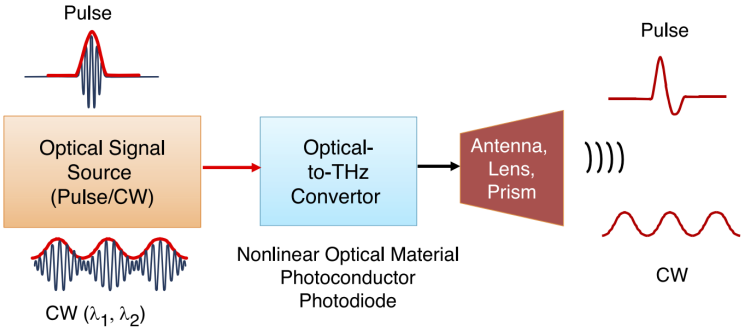


Figure 2.2: The typical architecture of photonics-based THz sources [42].

Photonics-based sources generate THz radiations indirectly by down-converting radiations in the optical band. Figure 2.2 [42] illustrates the typical architecture of photonics-based THz sources that are capable of generating monochromatic continuous-wave (CW) and polychromatic pulsed radiations. For polychromatic THz pulse generation, the input radiation is an ultra-short optical pulse lasting several femtoseconds. Both linear and nonlinear optics can be employed as the optical-to-THz converter here. Linear optics includes various photoconductive semiconductor (GaAs, InAs, and GaSe) switches [43–45]. The input optical pulse changes the conductance of a DC-biased photoconductive switch, generating a THz pulse whose power spectral density is jointly decided by the optical pulse and the switch. Nonlinear crystals (DAST, GaP), based on the optical rectification process, can also achieve the conversion and produce THz pulses with higher bandwidth [46, 47]. Monochromatic continuous-wave is generated from two CW laser inputs with their frequency difference falling into the THz band [48]. Photomixers based on photoconductors or photodiodes (e.g., uni-travelling-carrier (UTC) photodiode) are commonly used to mix two optical inputs into a THz output [49, 50]. Nonlinear approaches for CW are mainly based on optical parametric processes [51, 52] or difference frequency generation (DFG) [53, 54]. Photonics-based technology is capable of generating THz radiations spanning from the far-infrared to the mid-infrared band, with excellent tunability and satisfying power level. Its shortcomings include high cost and a low level of integration. Recent progress on electronics-photonics hybrid systems could be an attractive solution

to this [24]. Figure 2.3 [24] shows the operational frequencies and power levels of different electronics and photonics technologies.

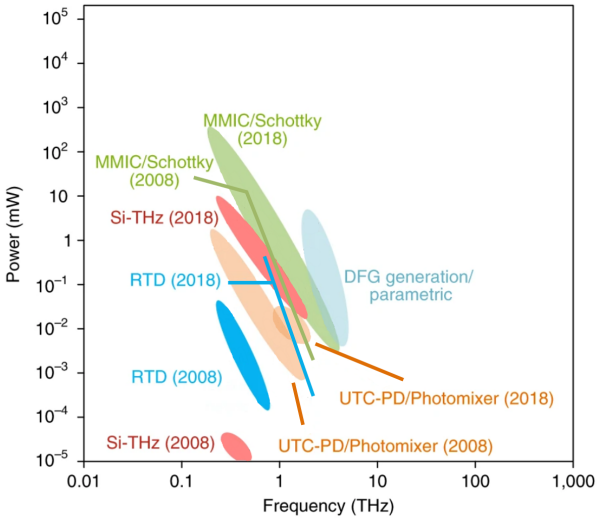


Figure 2.3: Specifications of electronics and photonics CW THz sources (adapted from [24]).

Without exploiting frequency down-conversion, laser technology has been applied to generate THz radiations directly. Gas lasers [55] are mature commercial products that produce infrared radiations based on the stimulated emission of gases (e.g., CO2, CO, and HeNe). Due to its poor programmability and tunability, high power gas lasers are only applied to special applications such as holography, cutting, and welding. Conventional semiconductor lasers based on interband transition are limited in THz bands due to the lack of small band-gap semiconductors. Recently, research interests have been focused on quantum cascade laser (QCL) technology, which provides great flexibility in the far-infrared and mid-infrared bands [56–58]. QCLs achieve intersubband transmission by employing a repeated stack of semiconductor multiple quantum well heterostructures, and thus their radiation frequencies can be tuned by engineering the layer thicknesses. Reported QCL systems can operate in both CW and pulse mode [59–61]. However, QCL technology still has several shortcomings, such as low wall plug efficient and low-temperature operation. Recent progress [62, 63] aims at addressing these problems, and

related commercial products start to show up.

Since any object above 0 K is a natural and 'free' radiator, THz radiations can also be generated by low-cost thermal sources with high emissivity. According to Planck's law, which describes the blackbody spectral radiance, the thermally-generated radiation is intrinsically polychromatic and unpolarized. Therefore, information can only be encoded into or decoded from its intensity. Commonly used thermal emitters, such as Globar lamp [64, 65], Mercury lamp [66], and carbon rod, are not very efficient THz sources due to their radiation peaks fall into the higher mid-infrared band. It has been shown that electromagnetic crystals can be employed to modify the power spectral density for enhancing radiations in the far-infrared band [67]. In addition, emissivities of thermal sources can be improved by metal or dielectric coating techniques [68].

Light-emitting diodes (LEDs) are semiconductor-based sources commonly seen in the near-infrared and visible bands [69]. Its radiation is polychromatic like thermal sources but has a much narrower bandwidth. LED technology is also capable of generating low-frequency radiations with limited power levels when operating at a low-temperature [70].

Sensors

Mechanisms for THz sensors and sources are closely related since an appropriate detection approach is ultimately decided by the properties of its targeted radiation.

Thermal-based sensors have a long history and can be applied to measure radiations' energy over a broadband [22]. All thermal detectors are essentially thermometers, which absorb the radiation energy and transduce the resulting temperature change to other measurable physical quantities. Various mechanisms can be employed to convert the temperature. Based on the thermal expansion phenomenon, radiation energy can be transformed into volume changes and measured mechanically [71]. Pyroelectric sensors electronically count the generated surface charges proportional to the temperature gradient [72, 73].

The resistance of various metal, insulator and semiconductor materials can be altered by temperature, which results in different kinds of bolometers [74, 75]. Besides, thermocouple and thermopile sensors [76] are based on temperature varied electric potential. The sensitivity and speed of thermal-based sensors can be generally improved by employing a cooling system.

Solid-state electronic sensors benefit from room temperature operation and high-level integration, mainly operating in the far-infrared band. Baseband signal carried by THz radiation can be obtained by either direct measurement or heterodyning, giving two categories of electronic sensors. While the direct measurement can only detect the radiation power, heterodyning is capable of retrieving the phase information from a monochromatic CW radiation, which is achieved by frequency down-conversion using local oscillators and frequency mixers. As essential components in frequency multiplier based THz sources, Schottky diodes are also widely used for detection purposes. High-speed Schottky diodes can perform direct measurement for both pulsed and CW radiations, like a THz video detector [77, 78]. In addition, mixers based on Shottky diodes are the core building block in most electronic heterodyning systems [79]. Other semiconductor diodes exploited in THz sensors, such as resonant tunnelling diode [80, 81] and backward tunnel diode, can provide higher nonlinearity and sensitivity. Another type of electronic sensor is based on the interaction between THz radiation and plasmons, which can be realized by field-effect transistors (FETs) [82, 83].

For pulsed THz radiation, the boundary between photonics-based sources and sensors are blurred. A pair of photoconductive antennas, one for pulse generation and another for detection, is a standard configuration for most THz time-domain systems [84, 85]. Sensors based on electro-optic rectification are also reported for THz pulse detection [86, 87]. For CW radiation detection, photomixers based on photoconductors or photodiodes can be seen in photonic heterodyning systems and electronic-photonic hybrid systems to achieve THz-to-baseband down-conversion [48, 88, 89].

Components

Some THz active components, such as transistors, mixers, and frequency multipliers, have been covered in previous sections. This section briefly reviews other active and passive components employed for radiation manipulation. One can refer to [23, 90–93] for more detailed surveys on related topics.

As the interface between the electric current and the electromagnetic wave propagating in free space, antennas are indispensable active components in most THz systems. Two promising antenna structures are planar antenna [94] on dielectric lenses and waveguide feed horns [95]. THz power amplifiers are usually combined with active antennas to boost their transceived power [24, 96].

The transfer of passive component technologies from millimeter wave and optical bands to our target bands is straight forward. Filters are manually designed optical paths to select required frequencies. Two commonly used types in the THz and infrared bands are the metal mesh filter [97] and the thin-film filter. The former is based on stacking capacitive and inductive metallic meshes. The latter utilizes the thin-film interference effect, coating materials with different refractive indexes onto a substrate. The frequency bands of these two technologies are complementary. While the mesh filter is widely used in the lower THz band, the thin film filter mainly operates in the far-infrared and mid-infrared bands. Other passive components, like off-axis parabolic mirrors and lenses, are exploited to collimate the beam for reducing spreading loss or focus the beam for illuminating the sample under test. In addition, reflective mirrors with metal coating are commonly used to implement delay stages in THz time-domain systems. Besides, beam splitters are important passive components in THz time-domain systems and Fourier transform spectrometers.

2.1.2 Terahertz and Infrared Systems and Applications

Combining enabling technologies for radiation generation, detection, and manipulation, various THz and infrared systems have been reported, empowering a broad range of communications, imaging, and spectroscopy applications. This section reviews the architecture and implementation of several representative systems.

Terahertz time-domain system

Terahertz time-domain systems exploit polychromatic pulsed THz radiations. Building blocks in a typical architecture include photonics-based pulse generator/sensor and quasi-optics tailored for specific applications.

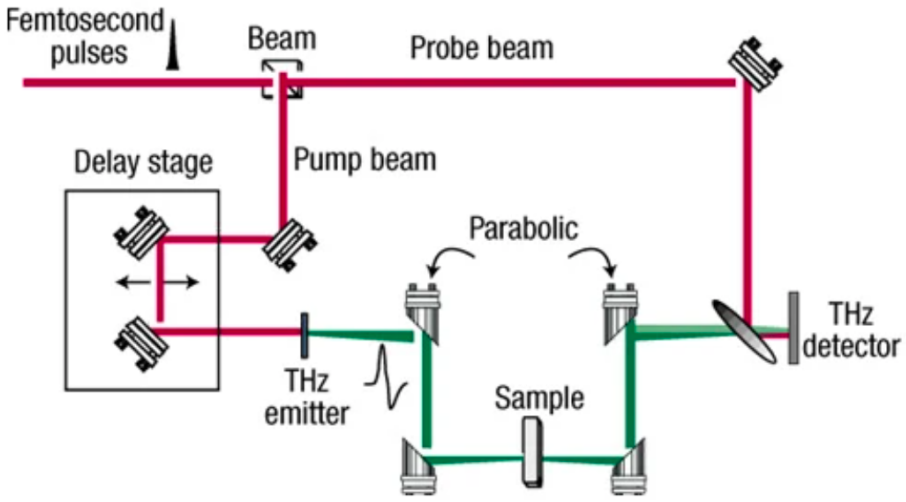


Figure 2.4: The typical architecture of a terahertz time-domain transmission spectroscopy (TDS) system [98].

Figure 2.4 [98] shows the typical architecture shared by most THz time-domain systems. Photoconductive antennas or non-linear electro-optic devices can be used to implement both the emitter and the detector. The femtosecond optical pulse from a laser is split into a pump beam and a probe beam. The pump beam stimulates the emitter to generate a THz pulse while the probe beam triggers the detector to measure the instantaneous

electric field of the THz pulse. The measuring timing, determined by the optical path difference between the pump and probe beam, can be controlled by the delay stage. For the illustrated transmission spectroscopy application, a group of off-axis parabolic mirrors is used to focus the beam on the sample under test. Once the received THz pulse has been measured by moving the delay stage, the sample's amplitude and phase responses can be obtained by studying the received power spectral density. By rearranging the quasi-optics and introducing reference measurements, the architecture in Figure 2.4 can be easily adapted to other spectroscopy systems [99]. Similar systems are also used for imaging applications such as near-field microscopy [100, 101] and diffraction/computed tomography [102]. For the former, sub-wavelength apertures and atomic force microscopy (AFM) tips are employed to overcome the diffraction limit and improve the spatial resolution. For the latter, a CCD camera can be combined with electro-optic detectors to achieve two-dimensional measurement, which greatly accelerates the imaging process. The THz time-domain system can also support analog and digital communications by modulating the optical pump beam [103, 104]. Here, incoherent sensors can be exploited to detect the pulse intensity if spectral and phase information is not required. However, communications based on pulsed THz radiations are limited by the repetition rate of the expensive femtosecond laser.

Terahertz continuous-wave system

As distinguished from thermally-generated polychromatic CW radiation, systems reviewed in this section employ monochromatic CW radiations generated and detected by electronics and photonics-based approaches [92, 105, 106]. Figure 2.5 shows block diagrams of typical THz CW transmitters and receivers, which are commonly used for digital communications purposes. Both electronic and photonic transmitters have a heterodyning architecture to up-convert the baseband signal to the THz band. The simple receiver architecture based on a diode detector can only perform a direct measurement

of the radiation intensity. Therefore, it's only suitable for amplitude-shift keying (ASK) modulation. The heterodyning receiver, which includes a local oscillator and a down-converter, is capable of extracting both amplitude and phase of the THz carrier and can be used with more complicated modulation schemes, such as quadrature phase-shift keying (QPSK) and quadrature amplitude modulation (QAM). Similar systems can be found in the near-infrared band (IrDA [7]) and visible band (visible light communications [107]).

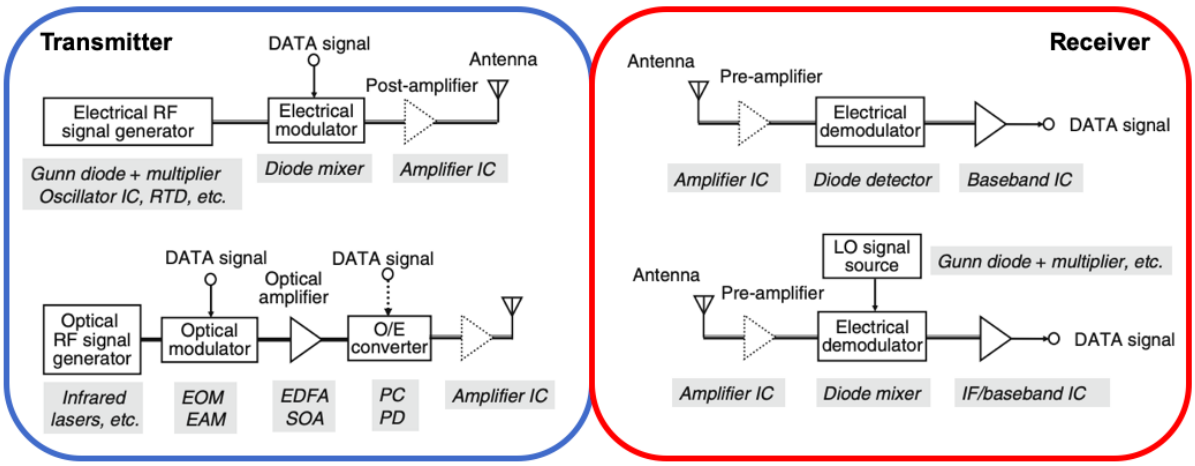


Figure 2.5: Block diagrams of typical THz CW transmitters and receivers (adapted from [92]).

THz CW radiations also find their application in imaging [48, 108, 109]. The advantage of using monochromatic CW radiation is that heavy atmospheric attenuation can be avoided by carefully choosing the radiation frequency, enabling imaging at a stand-off distance. For imaging purposes, it is usually sufficient to measure the radiation intensity and, thus, diode detectors and even broadband thermal-based detectors can be employed. Here, the modulator can be used to implement a lock-in amplifier with an improved signal-to-noise ratio. It's also possible to combine the transmitter and receiver, giving a compact homodyne architecture [48]. Most reported CW imaging systems could only scan static samples fixed on a translation stage. Further research could focus on sensitive imaging

arrays for moving targets.

Thermal-based system

Thermally generated polychromatic CW radiation is conventionally exploited for thermal imaging [110], Fourier-transform spectroscopy [111], and sensor/filter calibration [112]. Thermal imaging is based on detecting the radiations from objects at different temperatures. Its sensor component is essentially an array of thermometers. Room temperature thermal imaging commonly employs bolometers or pyroelectric sensors. In comparison, high-quality and fast thermal imaging can be achieved by using semiconductor-based photodetectors and cooling systems. Fourier-transform spectroscopy relies on the broadband nature of thermally generated radiations. Its basic mechanism is extracting the spectral density from the measured interferogram. Compared to THz-TDS, Fourier-transform spectroscopy is low-cost, less accurate, and more time-consuming. Recent works also demonstrate the use of thermal sources in microspectroscopy [113] and tomography [114].

'THz Torch' communications links

In 2011, the first thermal infrared wireless communications system [11] was reported, which exploited the use of extremely low-cost thermal emitters (miniature incandescent light bulb arrays) and pyroelectric infrared (PIR) motion sensors; collectively referred to as the 'THz Torch' technology within the physical layer. Here, an amplitude-modulated noise carrier is incoherently detected to support wireless data transfer. Over the past eight years, various aspects have been investigated, from system-level architectures [12] down to device level enabling technologies [13–15], while maintaining the underlying ethos of employing inherently low-cost components − making the technology affordable for future ubiquitous low data rate wireless links that can be used for secure applications (e.g., private key fobs, covert remote controls, secure device-to-device data links, etc.). Proof-

of-principle single [11, 16] and multi-channel [12, 17] demonstrations have been previously reported.

The first reported demonstrator [11] employed a direct electronic modulation scheme, having the advantages of simplicity, reliability, and low cost, but the maximum bit rate for sending arbitrary data is of the order of 10 bps. With subsequent prototypes [12, 15–17], the emitters generated a constant thermal radiation power (i.e., time-invariant) and employed mechanical choppers as an indirect modulation mechanism. This solution mitigates against thermal time constant constraints, offering the advantage of faster data rates. Maximum bit rates for sending arbitrary data are of the order of 640 bps using mechanical choppers [17], limited by the moment of inertia and angular momentum; faster speeds are possible with mechanical shutters. However, all mechanical solutions are expensive and have limited working lifetimes of operation (short-lifetimes with shutters and medium-lifetimes with choppers). To date, the reported operational figure of merit (Range × Bit Rate) for 'THz Torch' wireless communications links have been limited by either thermal mass (direct electronic modulation) or physical mass (indirect mechanical modulation). With the former, solid-state solutions may be needed; with the latter, one possible solution could be to employ micro-electromechanical systems (MEMS) technology.

In the following chapters, the basic principles behind the 'THz Torch' physical layer are redeveloped from a stationary radiation perspective (with operation constrained by the inherent thermal time constants associated with the thermal source and sensor) to one that truly exploits natural thermodynamic behaviour. The underlying theory is proved experimentally, demonstrating significantly reduced bit-error-rate (BER) with increased transmission range and bit rate.

2.2 Machine learning in communications

Machine learning [115, 116] is a successful interdisciplinary field that employs computational statistics to discover underlying mapping, pattern, or optimal decision rule from data. Recent developments in neural network-based deep learning [117] significantly improve the flexibility and expressiveness of machine learning models, providing new perspectives and tools for other research fields. This section first introduces three broad categories of problems that can be solved using machine learning. Then, an overview of the neural network and deep learning, with their strength and weakness, is presented. Finally, we review recent works that combine machine learning techniques into communication system design. These advances inspire our channel estimator and the neural network-based demodulator for 'THz Torch' communications links.

2.2.1 Problems solved by machine learning

Machine learning problems can be divided into three categories: supervised learning, which finds a mapping from the input to the output; unsupervised learning, which discovers hidden structures from data; and reinforcement learning, which learns a decision process to control a system optimally. Any applications of machine learning can be abstracted as one of these problems.

Given a training dataset $\{(x_i, y_i)\}_{i=1}^{N}$ which contains N input-output pairs (x_i, y_i), the task of supervised learning is to learn a function (model) $y = f(x)$ to approximate the real underlying mapping from the input to the output. According to whether the output is continuous or discrete, supervised learning problems can be further categorized into regression and classification problems. The learned function is evaluated by its performance on unseen data, which is known as the generalization ability of the model. The most commonly-used supervised learning model is linear regression [115], which serves as

a workhorse in many engineering areas. More complicated supervised learning models are based on geometry [118], frequentist statistics [119], and Bayesian statistics [120]. The main concern of these algorithms is the bias-variance trade-off [121]. A model with good generalization should have a carefully-controlled complexity, so it does not under-fit or over-fit to the training dataset.

Unsupervised learning algorithms aim at discovering patterns from an unlabelled dataset $\{x_i\}_{i=1}^{N}$. One example is the clustering analysis, which segments the whole dataset into groups according to the properties of samples. It can be achieved by density-based or Bayesian models [115]. More powerful unsupervised learning models are capable of finding low dimensional representations for high dimensional x_i and even modelling the generation process (the marginal distribution) of the dataset [122, 123]. These models can be exploited as a dimension reduction step for supervised models. They also provide insight into the structure hidden in data and a method to generate artificial data.

Reinforcement learning, as a unique paradigm in machine learning, solves an optimal control problem [124]. As illustrated in Figure 2.6 [124], it can be formalized as a Markov Decision Process (MDP): the agent interacts with the environment by choosing an action based on to its current observation; the environment is transitioned to a new state according to its current state and the action, returning a new observation (a representation of its new state) and a reward to the agent; then the agent makes its next move. The target of reinforcement learning is to find an optimal decision rule for the agent to maximize the obtained cumulative reward. Algorithms falling into this class can be either value function-based [125] or policy gradient-based [126].

2.2.2 Deep learning

Deep learning focuses on the theory and applications of deep neural networks, which provides powerful function approximators for solving machine learning problems [117]. The

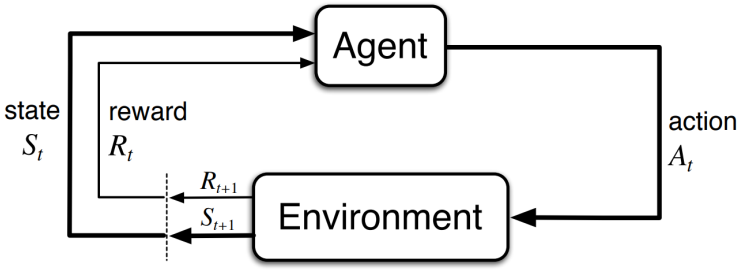


Figure 2.6: Markov decision process framework for reinforcement learning [124].

neural network has a fully differential architecture which is composed of parameterized non-linear functions (layers). These parameters in layers can be optimized using gradient-based methods by minimizing a predefined loss function between the expected output and the neural network's output. The method for computing the gradient is known as back-propagation, which is essentially a large scale application of the chain rule for multi-variable vector-valued functions [127]. The main strength of the neural network is its high flexibility. Even a simple network architecture is able to achieve complex input-to-output mappings. The output from a network's intermediate layers can be treated as high-level features (representations), which are automatically extracted from the raw input. For conventional machine learning algorithms, these features have to be engineered manually, and there is no guarantee of their predictive power.

The basic theoretical ground of deep learning was established in the last century. Recent fast-paced progress in this field is driven by hardware advances which enable fast training and inference in large scale (wider and deeper) neural networks with millions of parameters [128]. Various network architecture is proposed to adapt to different structures of inputs. For example, the convolutional neural network (CNN) for imaging processing takes the spatial structure of its input images into account [129]. Architectures customized for time series, such as the recurrent neural network (RNN) and long-short term memory (LSTM), utilize the temporal structures of their input sequences [130]. Besides extending the deep learning applications, more theoretical works contribute to the non-convex optimization

problem originated from the neural network training.

The major shortcoming associated with highly flexible deep learning models is over-fitting. To overcome this problem, it requires a large amount of data for network training, which is not feasible for specific real-world applications. In addition, deep learning models usually lack interpretability. It is hard to intuitively explain the decision rule operated by a trained neural network. This weakness stops discovering new knowledge from the trained model and employing this technology in risk-averse applications. Recent research topics, such as few-shot learning and interpretable deep learning, are proposed to tackle these shortcomings [131, 132].

2.2.3 Machine learning in communications

Machine learning provides powerful statistic tools to model and optimize communication systems. This data-driven approach has demonstrated its potential to outperform classic communication theories and models, especially for complex systems. This section reviews existing works that abstract functions of individual components or the whole transceiver into machine learning problems and solve them with carefully designed models.

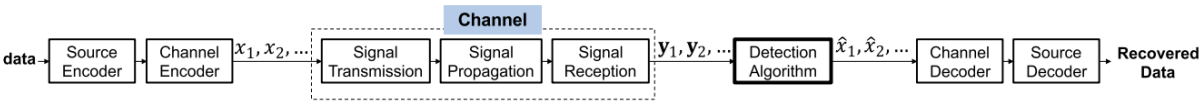


Figure 2.7: Block diagram for a typical digital communications system [133].

Figure 2.7 [133] shows the block diagram for a typical digital communications system. Data in different formats, such as video, audio, and text, is first compressed and transformed into a symbol sequence by the source encoder. For error correction purpose, extra redundant symbols are injected into the sequence by the channel encoder. The channel represents the transmitting and receiving of the symbol sequence in the form of a contin-

uous electric signal. The detection algorithm demodulates the received signal to retrieve the transmitted symbols. Finally, the channel decoder uses the redundant symbols for error correction, and then the source decoder reconstruct the raw data from corrected symbols. Most steps in this procedure can be translated into machine learning problems and solved accordingly.

Core functions of the source encoder and decoder are compressing and decompressing the raw data for reducing the communication cost. Its counterpart is an unsupervised learning problem that seeks a bijection from the data space to a low-dimensional latent space. Recent works exploit deep neural network-based encoder and decoder to achieve this bijection mapping for text [134], image [135], and video [136] compression.

A channel estimator, which estimates the parameters in the channel model or senses the channel state information, is a key component for signal detection. Its abstraction is a supervised regression problem with some training signals as its input and the channel information as its output. Advanced deep learning-based channel estimators for millimeter-wave massive multiple-input-multiple-output (MIMO) systems have been reported [137–139].

The detection algorithm performs a mapping from the sampled received signals to discrete symbols. Therefore, it can be abstracted as a classification problem. Considering the temporal structure of the received signal, deep learning models for time-series, such as RNN and LSTM, are perfect fits for demodulation purposes [133, 140–144]. In addition, the channel decoder, which achieves a sequence-to-sequence transformation, can also exploit similar models [145, 146].

Except for employing machine learning to improve individual blocks, machine learning-based end-to-end communications systems are also reported [147, 148]. Other machine learning applications in communications include resource allocation, user localization, and interference mitigation. More detailed surveys on these topics can be seen in [149, 150].

Chapter 3

Channel Architecture and Modelling

In this chapter, we first introduce the channel architecture for the 'THz Torch' wireless link. Two experimental setups in different environments are implemented as hardware test benches for this work and multi-processing software code for this link is implemented in Python. In Section 3.2, all the transceiver building blocks are well characterized by modelling their thermodynamic behaviour when being modulated beyond their thermal time constants. We also present novel optimization-based channel estimators to extract the sensor and emitter parameters from the corresponding training signals. The cognitive 'THz Torch' receiver introduced in Chapter 4 heavily relies on the channel model and estimator developed here. Finally, a noise analysis for our system is conducted in Section 3.3, providing a theoretical tool for signal-to-noise ratio improvement.

3.1 Channel Architecture

The typical architecture for our 'THz Torch' wireless link is illustrated in Figure 3.1a, consisting of a transmitter (Tx) and a receiver (Rx). Two experimental setups for a 2 m link are shown in Figure 3.1b and Figure 3.2, respectively. According to the transmitted

symbol sequence, the thermal emitter is modulated using the simple ON-OFF keying (OOK) scheme. The generated thermal radiation is spectrally filtered using a thin-film bandpass filter (BPF), which defines the frequency range of the incoherent noise carrier for a specific channel (listed in Table 3.1). To minimize spreading loss, the thermal emitter has a conical horn; a plano-convex optical lens is added to collimate the diverging beam of thermal radiation. After propagating through the free-space, the collimated thermal radiation is focused by an identical lens, through a matched BPF, onto a PIR sensor. The analogue voltage signal from the sensor is fed into an analogue-to-digital converter (ADC) and processor, from which the transmitted symbol sequence is recovered. A mechanical shutter is included to generate a thermal radiation step function needed for channel estimation.

3.1.1 Laboratory Experimental Setup

The implementation of the wireless link in a laboratory environment, shown in Figure 3.1b, is detailed as follows. The transmitter is composed of a commercial infrared thermal emitter (INTX 17-0900) modulated by a switchable constant current source (RCD-24-0.70). The current source can deliver a quoted current of 134 mA to maintain the emitter at a steady-state temperature of 1,023 K. To modulate the thermal emitter according to the transmitted symbol sequence, a microprogrammed control unit (Arduino-DUE) is employed to switch the driver (current source) between the ON/OFF states. For the single-channel prototype, the noise carrier is defined by a matched pair of 8 - 14 μm silicon wide-BPFs. The multi-channel prototype exploits eight matched pairs of thin-film narrow-BPFs, fabricated by Northumbria Optical Coatings Ltd. A matched pair of ZnSe lenses are used for beam collimation (Tx) and focusing (Rx). At the receiver, the incident radiated power is transduced to a voltage by a pyroelectric sensor (LME-335). The signal is then sampled by a National Instruments (NI) data acquisition card and sent to a computer to perform cognitive synchronization and demodulation.

Table 3.1: Band-pass filter specifications. The aperture blockage is calculated with reference to an unblocked circular filter having diameter $\varnothing = 9$ mm.

	50% cut-off, λ_1 to λ_2, bandwidth μm (THz)	Aperture size mm^2	Aperture blockage* %
ch#1	4.48 - 4.54 (65.95 - 66.88)	4.6 × 4.6	67
ch#2	4.74 - 4.79 (62.57 - 63.25)	4.9 × 4.9	63
ch#3	5.09 - 5.31 (56.44 - 58.83)	3.8 × 3.8	78
ch#4	7.01 - 7.11 (42.19 - 42.79)	5.6 × 5.6	51
ch#5	7.37 - 7.48 (40.08 - 40.67)	5.6 × 5.6	51
ch#6	8.22 - 8.62 (34.81 - 36.45)	3.8 × 3.8	78
ch#7	9.61 - 10.03 (29.92 - 31.23)	3.7 × 3.7	69
ch#8	10.09 - 10.54 (28.46 - 29.74)	4.7 × 4.7	65
Single	8.03 - 13.74 (21.83 - 37.33)	4.6 × 4.6	67

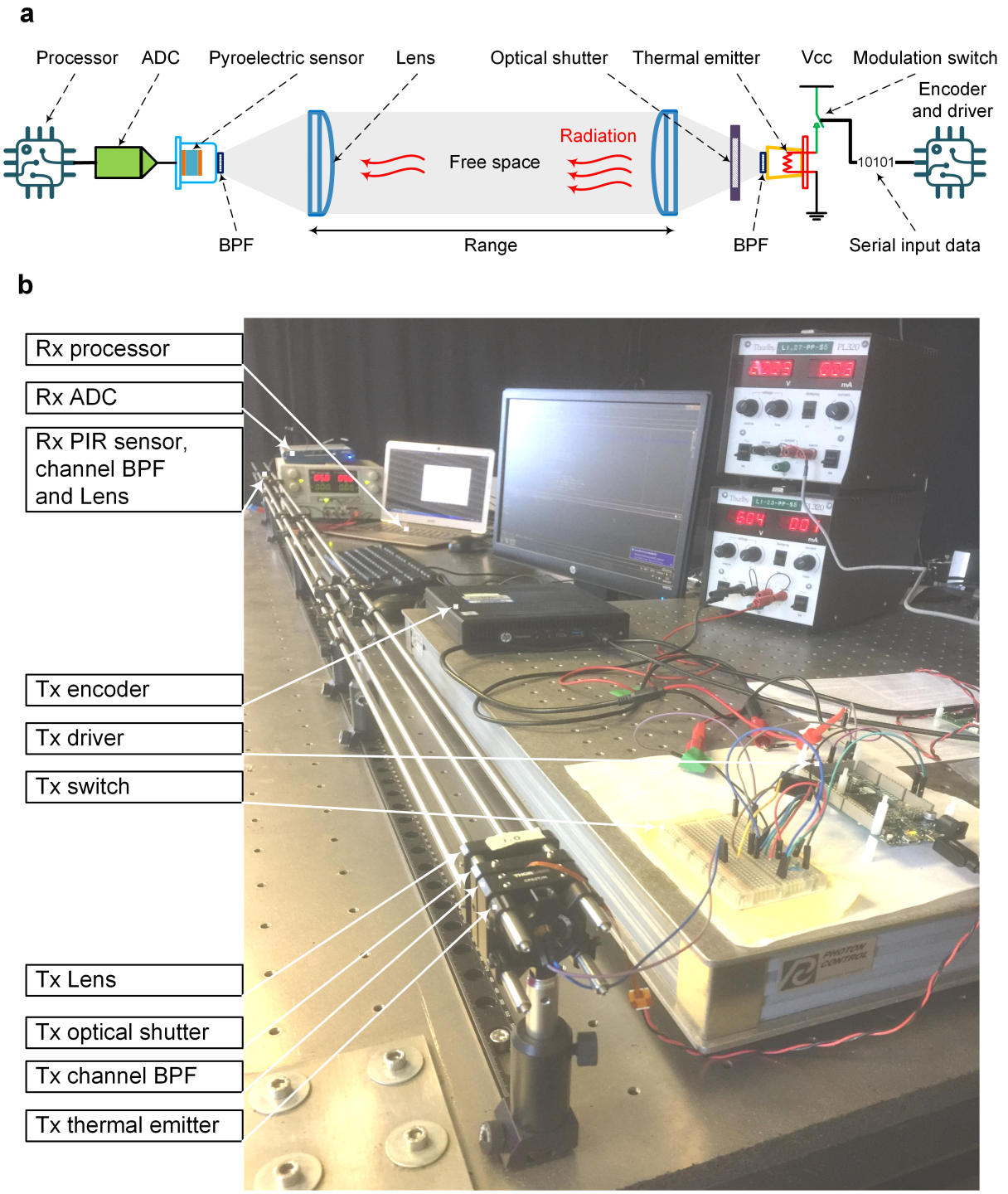


Figure 3.1: Typical 'THz Torch' wireless link. (**a**) Architecture. (**b**) Laboratory experimental setup with a range of 2 m.

3.1.2 Non-laboratory Experimental Setup

As shown in Figure 3.1, the laboratory setup employs an optical bench and precision alignment rails. Experiments are also performed in a non-laboratory setting (within an office corridor, as shown in Figure 3.2). Instead of using precision alignment rails, the field trials employ simple laser alignment, with the use of two 3D-printed guide holes in both the transmitter (Tx) and receiver (Rx) setups. In addition, a 3D-printed shroud is used by the receiver to suppress microphonic noise and ambient temperature fluctuations.

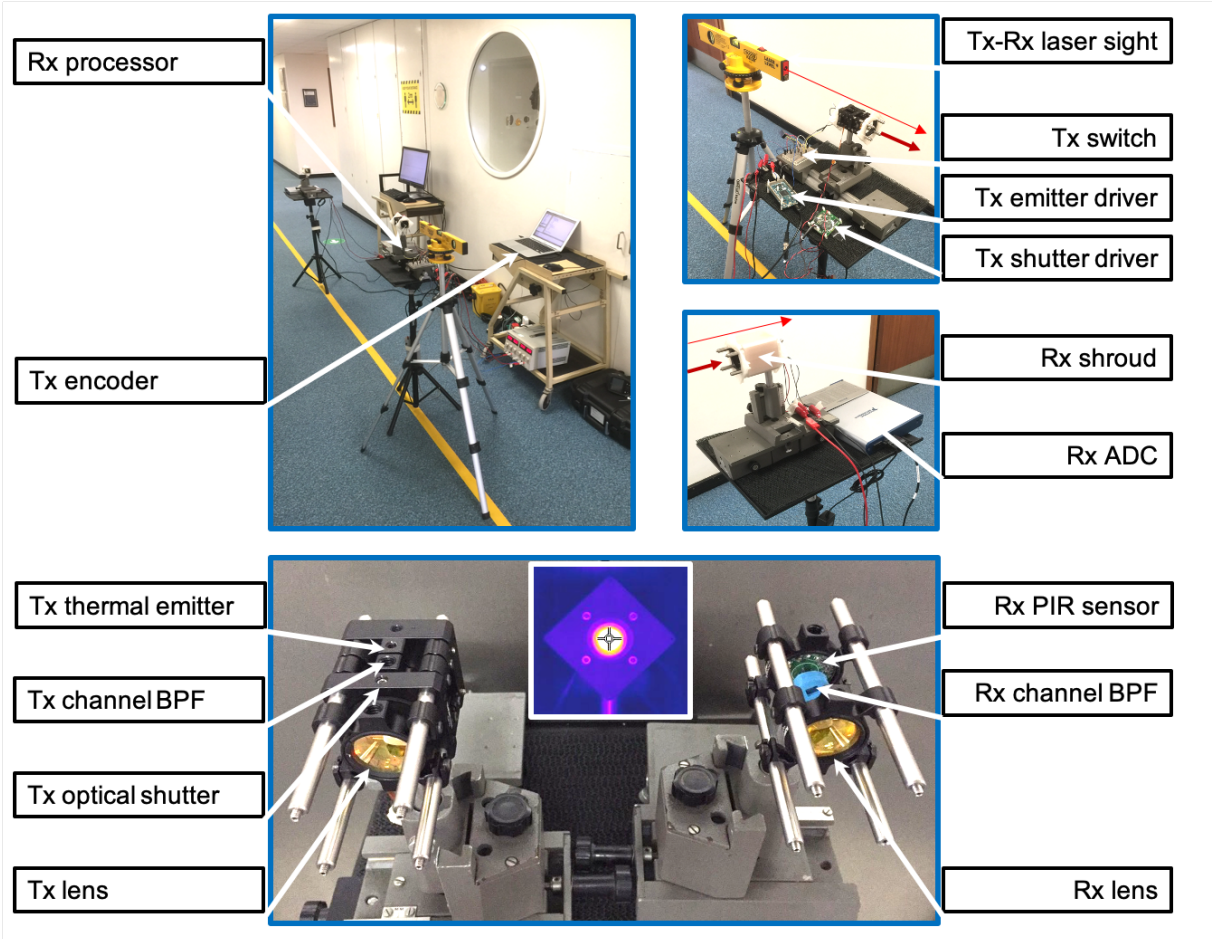


Figure 3.2: Practical field trials for a 2 m 'THz Torch' wireless link. The insert in the lower figure shows the thermal image of the transmitter's front-end hardware with the thermal emitter in the ON-state (the cross-hairs from the camera indicate the centre of the Tx lens).

3.1.3 Software Architecture

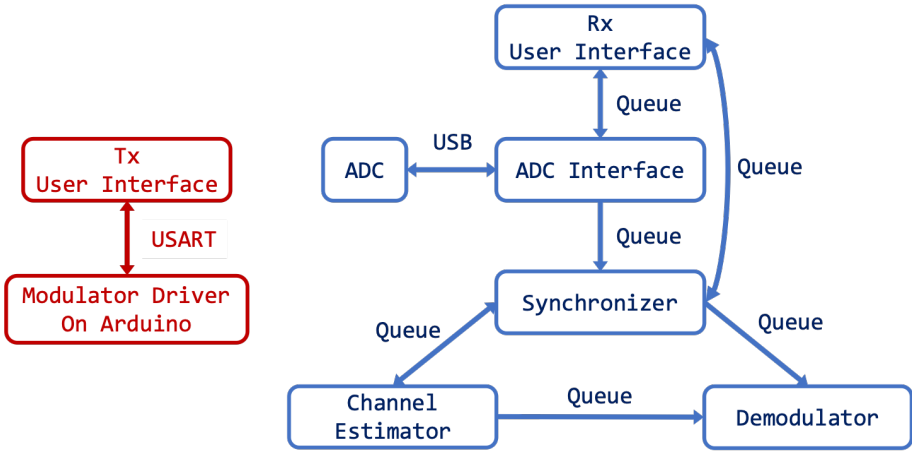


Figure 3.3: Software architecture diagram for the 'THz Torch' transceiver.

Figure 3.3 shows the top-level structure of the implemented 'THz Torch' software code. At the transmitter end, the Tx User Interface encodes the information from the operator and the encoded result is sent to the Modulator Driver, through a serial communications interface (USART). The Modulator Driver then switches the ON/OFF state of the thermal emitter by controlling the logic level of its digital pin. At the receiver end, each block (except the ADC) represents a standalone process and the inter-process communications are achieved by message queues. The ADC Interface is used to configure the ADC and read the sampled signal into an internal buffer, through a Universal Serial Bus (USB). The sampled signal is then forwarded to a cognitive receiver, which consists of the synchronizer, the channel estimator and the demodulator (See Chapter 4). All these receiver blocks report their status to the Rx User Interface and receive commands from the interface to adjust their configurations. A detailed code overview for this software will be given in Appendix A.

3.2 Channel Modelling

3.2.1 OOK Modulated Thermal Infrared Emitter

The 'THz Torch' transmitter consists of a thermal emitter and a regulated power supply, connected via a switch whose ON/OFF state is controlled by 100% duty cycle pulses corresponding to the transmitted symbol sequence. In other words, an amplitude shift keying is employed with a binary constellation (symbol set) $\{S0, S1\}$. When transmitting a symbol $S1$, the power supply is connected to this crude thermal emitter, thereby heating it up during this symbol interval. When transmitting a symbol $S0$, the power supply is disconnected from the thermal emitter, thereby cooling it down naturally during this symbol interval. The symbol rate equals the reciprocal of the pulse width duration, and the bit rate is the same as the symbol rate. We now study the polychromatic radiation and the thermodynamics of the emitter under OOK modulation.

The spectral density of the polychromatic radiation generated by an ideal blackbody emitter can be expressed by Planck's law:

$$I(\lambda, T) = \frac{2hc^2}{\lambda^5} \frac{1}{e^{hc/(\lambda k_B T)} - 1} \tag{3.1}$$

where λ is the wavelength in free space; h is the Planck constant; c is the speed of light in free space; T is emitter temperature; and k_B is the Boltzmann constant. Unlike an isotopic source that radiates over a perfect sphere, our thermal emitter has a heated film (with area A_e) that is better modelled by radiation over a half-sphere. As shown in Figure 3.4, this radiation is efficiently confined by a reflecting conical horn, giving a beam whose angular power distribution can be fitted by a Lorentzian curve in equation (3.2).

$$B(\alpha) = \frac{0.142^2}{\alpha^2 + 0.142^2} \tag{3.2}$$

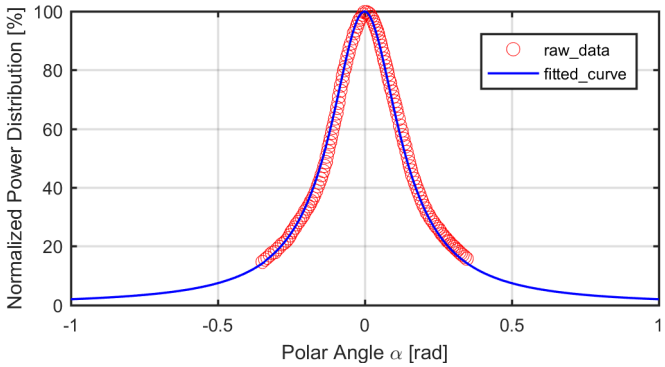


Figure 3.4: Measured angular distribution of radiation and fitted Lorentzian curve.

Moreover, unlike a blackbody radiator, our emitter has an emissivity ϵ. As a result, the theoretical thermal emitter power spectral density p_e can be given as:

$$p_e(\lambda, T) = \epsilon A_e I(\lambda, T) \int_0^{2\pi} cos(\theta) d\Omega = \int_0^{2\pi} d\varphi \int_0^{\frac{\pi}{2}} cos(\theta) sin(\theta) d\theta = \pi \epsilon A_e I(\lambda, T) \quad (3.3)$$

where Ω is the solid angle; θ and φ are the zenith and azimuth angles in spherical coordinates, satisfying $d\Omega = sin(\theta) d\theta d\varphi$. The $cos(\theta)$ term is due to the Lambertian nature of the thermal emitter. By integrating equation (3.3), over the passband of the predefined channel, the theoretical power of the thermally generated noise carrier is given by:

$$P_e(T) = \int_{\lambda_1}^{\lambda_2} p_e(\lambda, T) d\lambda \quad (3.4)$$

where the lower and upper cut-off wavelengths for the channel passband are λ_1 and λ_2, respectively, given in Table 3.1 and showed in Figure 3.5a. The radiated power calculated using equation (3.4) with the emitter steady-state temperature T_s is shown in Figure 3.5c, for each channel.

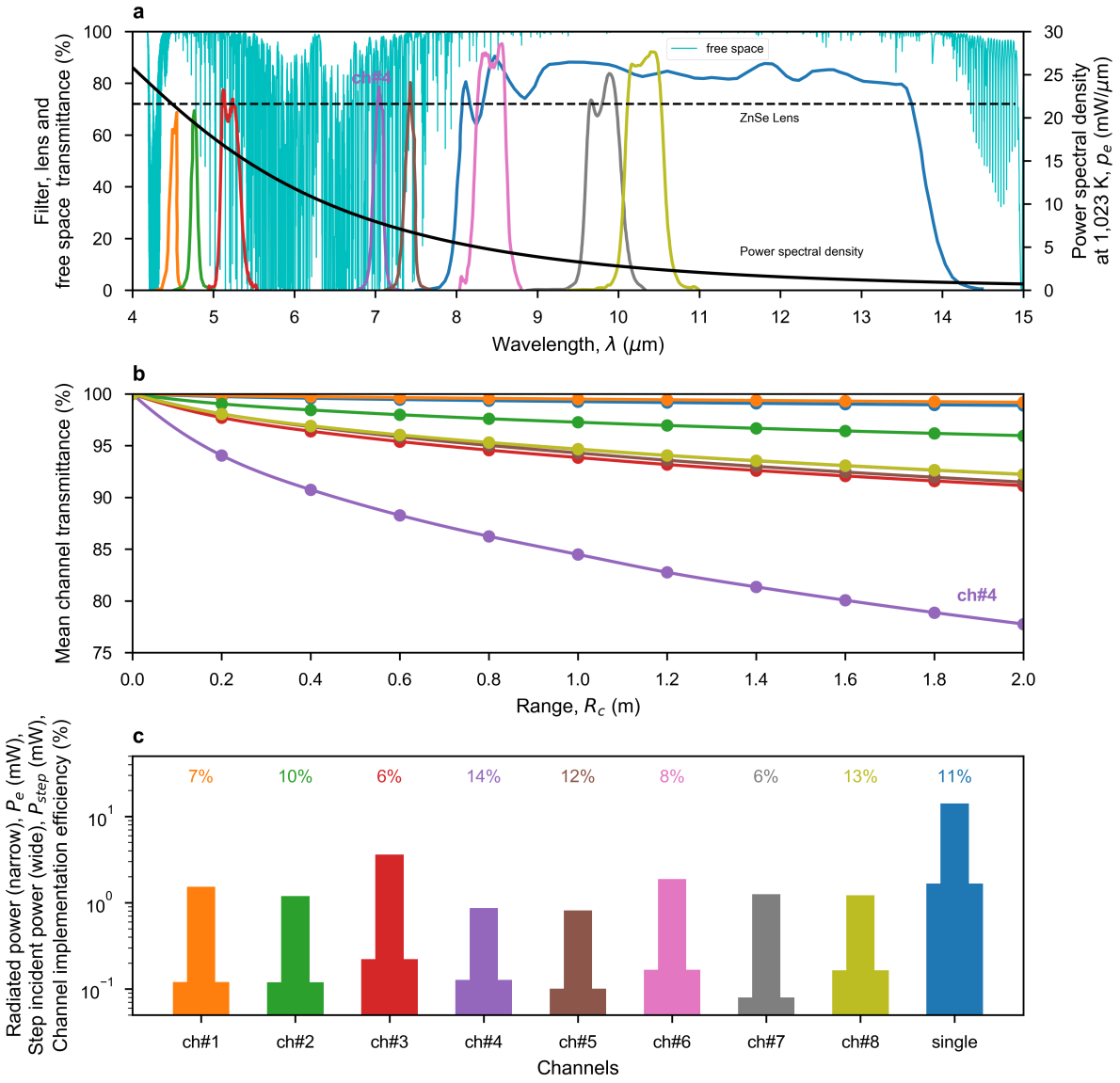


Figure 3.5: Channel characterization. (**a**) Theoretical thermal emitter power spectral density, measured channel band-pass filter and lens transmittance responses, and simulated free-space transmittance across the 2 m link under pristine conditions. (**b**) Predicted mean channel transmittance against range, using equation (3.11). (**c**) Theoretical radiated power within the channel filter passband, using equation (3.4), for a steady-state emitter temperature of 1,023 K; step incident power, using equation (3.20) with $L_c = 1$; and the resulting channel implementation efficiency.

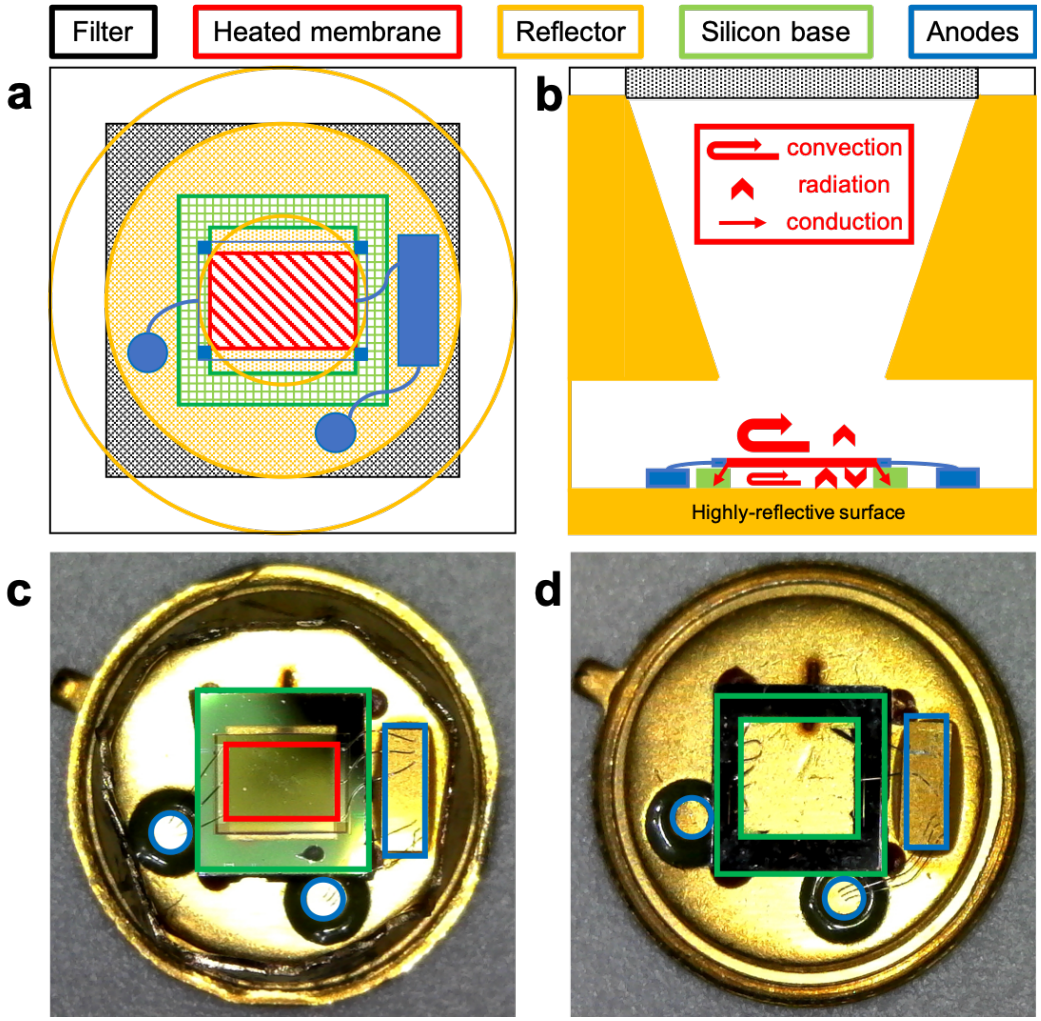


Figure 3.6: Thermal emitter (**a**) Top-view illustration. (**b**) Side-view illustration with heat transfer mechanisms indicated. (**c**) Photograph with the filter and cone reflector removed. (**d**) Photograph with the filter, cone reflector and thin-film membrane removed.

With direct electronic OOK modulation, the thermal emitter's transient temperature $T(t)$ varies between the extreme limits of the ambient temperature T_0 and its steady-state temperature T_s. Obeying the principle of conservation of energy, the following analytical expression has been formulated:

$$W_e(t) = C_e \frac{dT(t)}{dt} + k_e[T(t) - T_0] + \sigma_e \epsilon A_e T^4(t) \tag{3.5}$$

where $W_e(t)$ is the thermal emitter's input power, varying with the transmitted symbols; C_e is the heat capacity of the thermal emitter; The k_e term collectively represents both

the thermal conduction and convection which are both linear w.r.t. the temperature difference; σ_e is the Stefan-Boltzmann constant. Equation (3.5) describes a dynamic process in which the input power contributes to a change in emitter temperature, thermal conduction and convection between the emitter and the environment, and black-body radiation. This equation can be justified using Figure 3.6, which shows the internal structure of the thermal emitter. Here, the metal reflector surface can be treated as a heat-sink having a constant-temperature. The k_e term is dominated by thermal convection. The backward radiation is not shown in the equation because it is reflected by the highly-reflective surface and re-absorbed by the thin-film membrane (a quasi-black body). The equation also represents the thin-film membrane as a thermal lumped element, assuming a uniform temperature distribution. According to the measured temperature distribution from the data-sheet, given in Appendix B, the uniform assumption may not hold over the whole area and, thus, we exploit an effective "emission area" for A_e, as suggested by the datasheet.

Using equation (3.5), the thermal conductance and convection k_e can be estimated by substituting $W_e(t)$ with the manufacturer's rated emitter DC power W_R and setting $T(t) = T_s$; In this steady-state, the temperature gradient term goes to zero, and thus k_e can be solved. A grid search method is then exploited to find the value of C_e that gives a calculated thermal time constant that equals the measured value given by the manufacturer.

The commercial thermal emitter INTX 17-0900 used for prototyping has turn-ON and turn-OFF thermal time constants of 14.4 ms and 16.8 ms, respectively. In its steady-state, the INTX 17-0900 emitter requires a typical value of $W_R = 897.8$ mW to keep its temperature at $T_s = 1{,}023$ K. With its emissivity $\epsilon = 0.8$ and heated membrane area $A_e = 2.89$ mm^2, equation (3.5) can be used to estimate its $k_e = 1.03\text{e}^{-3}$ W/K. Given its measured thermal time constant of 14.4 ms, the heat capacity $C_e = 1.9\text{e}^{-5}$ J/K can be obtained. In Section 3.2.4, we will introduce an optimization-based emitter estimator for

calibrating these parameters. Values obtained here serve as a good initialization.

Equation (3.5) does not have a closed-form solution for the transient emitter temperature $T(t)$. It can be generally solved by numerical methods, which could be time-consuming. A power series, given in equation (3.6), can be used to approximate the solution to this differential equation.

$$T(t) = T(0) + a_1 t + a_2 t^2 + a_3 t^3 + O(t^4) \tag{3.6}$$

where $T(0)$ is the initial emitter temperature, and a_1 to a_3 are the first three polynomial coefficients whose value can be found by substituting equation (3.6) into equation (3.5):

$$\begin{aligned} C_e[a_1 + 2a_2 t + 3a_3 t^2 + O(t^3)] + k_e[T(0) + a_1 t + a_2 t^2 + a_3 t^3 + O(t^4) - T_0] \\ +\sigma\epsilon A_e[T(0) + a_1 t + a_2 t^2 + a_3 t^3 + O(t^4)]^4 - W_e = 0 \end{aligned} \tag{3.7}$$

where the dependency of W_e on time t is dropped due to W_e can only take the value of W_R or zero with the OOK modulation. Since all coefficients on the right-hand side, including the constant term, have to be zero, the values of a_1 to a_3 can be solved recursively. Setting the constant term to zero gives:

$$\begin{aligned} C_e a_1 + k_e[T(0) - T_0] + \sigma\epsilon A_e T^4(0) - W_e = 0 \\ a_1 = \frac{W_e + k_e[T_0 - T(0)] - \sigma\epsilon A_e T^4(0)}{C_e} \end{aligned} \tag{3.8}$$

a_2 is then solved by using the first-order coefficient:

$$\begin{aligned} 2C_e a_2 + k_e a_1 + {}^4C_1 \sigma\epsilon A_e T^3(0) a_1 = 0 \\ a_2 = -\frac{a_1[k_e + 4\sigma\epsilon A_e T^3(0)]}{2C_e} \end{aligned} \tag{3.9}$$

where ${}^nC_k = \frac{n!}{k!(n-k)!}$ is the combination function. Similarly, the value of a_3 can be solved

by studying the second-order coefficient:

$$\begin{aligned} 3C_e a_3 + k_e a_2 + {}^4C_1 \sigma \epsilon A_e T^3(0) a_2 + {}^4C_2 \sigma \epsilon A_e T^2(0) a_1^2 = 0 \\ a_3 = -\frac{a_2 k_e + 4 a_2 \sigma \epsilon A_e T^3(0) + 6 a_1^2 \sigma \epsilon A_e T^2(0)}{3C_e} \end{aligned} \tag{3.10}$$

As shown in Figure 3.7a, the power series, including the first three order terms, represents a good approximation over a duration around 12 ms. A better approximation over a longer duration can be obtained by taking higher-order terms $O(t^4)$ in the power series into account. We empirically find that the derived third-order power series achieves a good trade-off between accuracy and complexity.

In practice, time is divided into short segments of Δt (e.g., $\Delta t = 5$ ms in this case), and this power series is reinitialized at the start of each time segment with a revised value of $T(0) = T(\Delta t)$, giving the piecewise power series result shown in Figure 3.7a. Substituting equation (3.6) into equation (3.3) gives a time-variant power spectral density, shown in Figure 3.7b. The OOK modulation is essentially switching $W_e(t)$ between zero (OFF state for $S0$) and W_R (ON state for $S1$) according to the transmitted symbol sequence. As an example, the transient behaviour of the thermal emitter for a '10101' symbol sequence, when modulated at 100 baud, is given in Figure 3.7c,d.

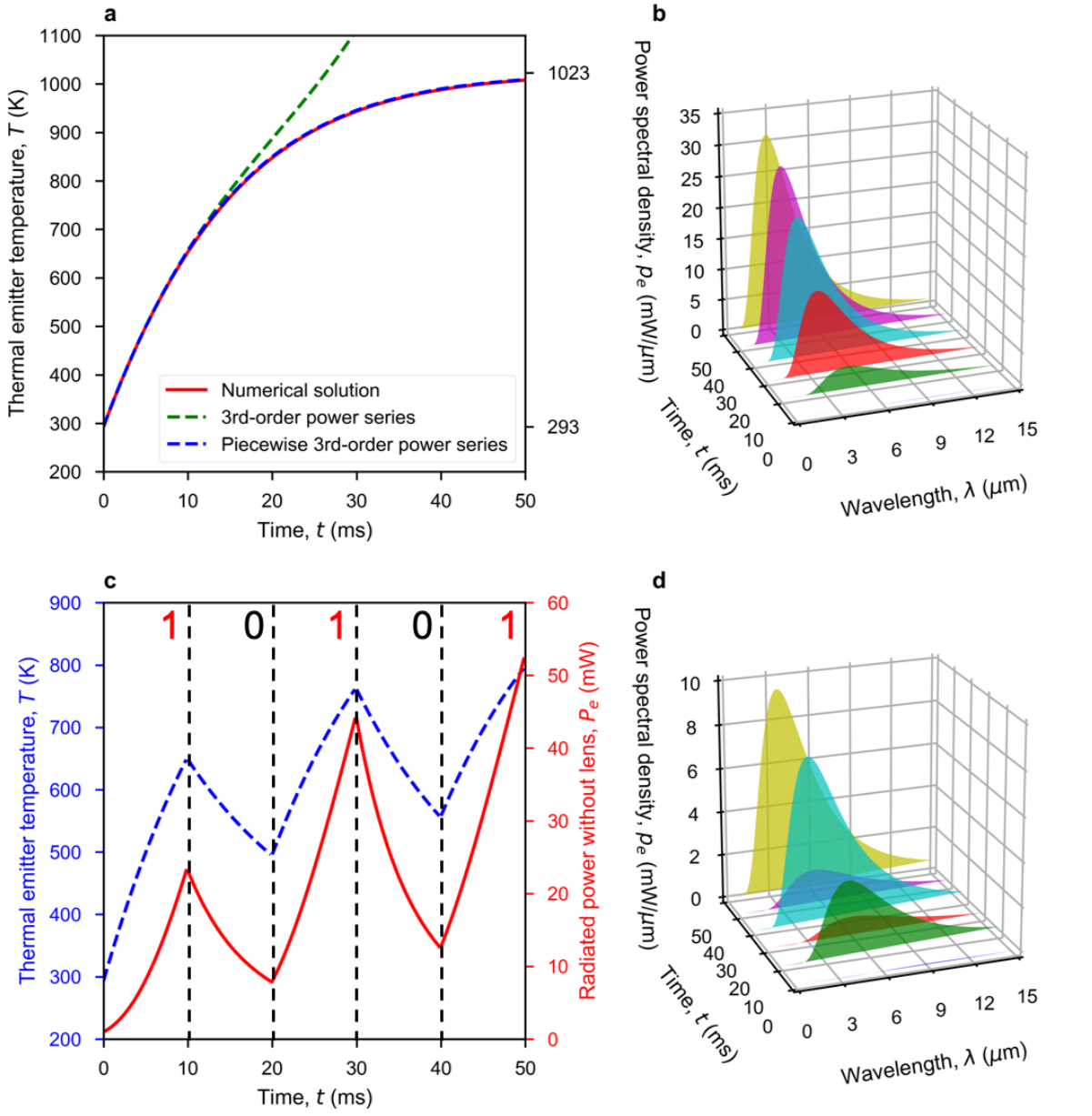


Figure 3.7: Calculated ideal thermal emitter (INTX 17-0900) responses. (**a**) Transient turn-ON behaviour of emitter temperature, with 898 mW of emitter DC power, from OFF-state at 20 °C ambient room temperature. (**b**) Time-variant power spectral density of thermal radiation corresponding to Figure 3.7a at 10 ms intervals. (**c**) Transient behaviour for both emitter temperature and radiated power (using piecewise power series) for a '10101' transmitted symbol sequence when modulated at 100 baud, from OFF-state at ambient room temperature. (**d**) Time-variant power spectral density of thermal radiation corresponding to Figure 3.7c at 10 ms intervals.

3.2.2 Free Space Transmission

When propagating through free space, the thermally generated radiated power suffers from spreading loss and atmospheric attenuation. While spreading loss can be mitigated by collimating the diverging beam and improving the alignment, atmospheric attenuation is inevitable and frequency-dependent. It originates from the absorption and scattering caused by molecules, particle, and liquid droplets. Previous work [151] has demonstrated the effectiveness of modelling atmospheric attenuation under pristine conditions (e.g., indoor and dry outdoor environments) employing the 'HITRAN on the Web' simulator, using the U.S. Standard 1976 mean latitude atmosphere model developed by NASA:

Table 3.2: U.S. Standard 1976 mean-latitude sea-level atmosphere model

	Summer	Winter
H_2O	1.86 %	0.43 %
CO_2	3.3×10^{-2} %	3.3×10^{-2} %
O_3	3.0×10^{-6} %	3.0×10^{-6} %
N_2O	3.2×10^{-5} %	3.2×10^{-5} %
CO	1.5×10^{-5} %	1.5×10^{-5} %
CH_4	1.7×10^{-4} %	1.7×10^{-4} %
O_2	20.9 %	20.9 %
N_2	77.2 %	78.6 %

Figure 3.5a shows the simulated atmospheric transmittance $\mathcal{T}_a$ of a homogeneous 2 m free-space under pristine atmospheric conditions. Mean channel transmittance $\mathcal{T}_c$, given by equation (3.11), is used to quantify a channel's resilience to atmospheric attenuation:

$$\mathcal{T}_c(T, R_c) = \frac{\int_0^{+\infty} p_e(\lambda, T)\mathcal{T}_f(\lambda)\mathcal{T}_a(\lambda, R_c)d\lambda}{\int_0^{+\infty} p_e(\lambda, T)\mathcal{T}_f(\lambda)d\lambda} \tag{3.11}$$

where, $\mathcal{T}_f(\lambda)$ is the transmittance of the channel's BPF shown in Figure 3.5a. As shown in Figure 3.5b, most channels have a relatively constant mean channel transmittance with range by trying to avoid absorption lines. The result demonstrates that the 'THz Torch' system is resilient to atmospheric attenuation across short-range links. Channel 4 has been highlighted, as it has a noticeably lower mean channel transmittance due to

atmospheric attenuation from water vapour absorption lines.

3.2.3 Pyroelectric Sensor

PIR sensors [72, 73, 152] are commonly used in low-end applications, such as ubiquitous motion detection and thermal imaging. However, the thermodynamic model developed in this section opens-up the PIR sensor to new applications; for example, in wireless receivers as an infrared radiation power-to-voltage transducer. The current-mode PIR sensor and its equivalent circuit model are shown in Figure 3.8a.

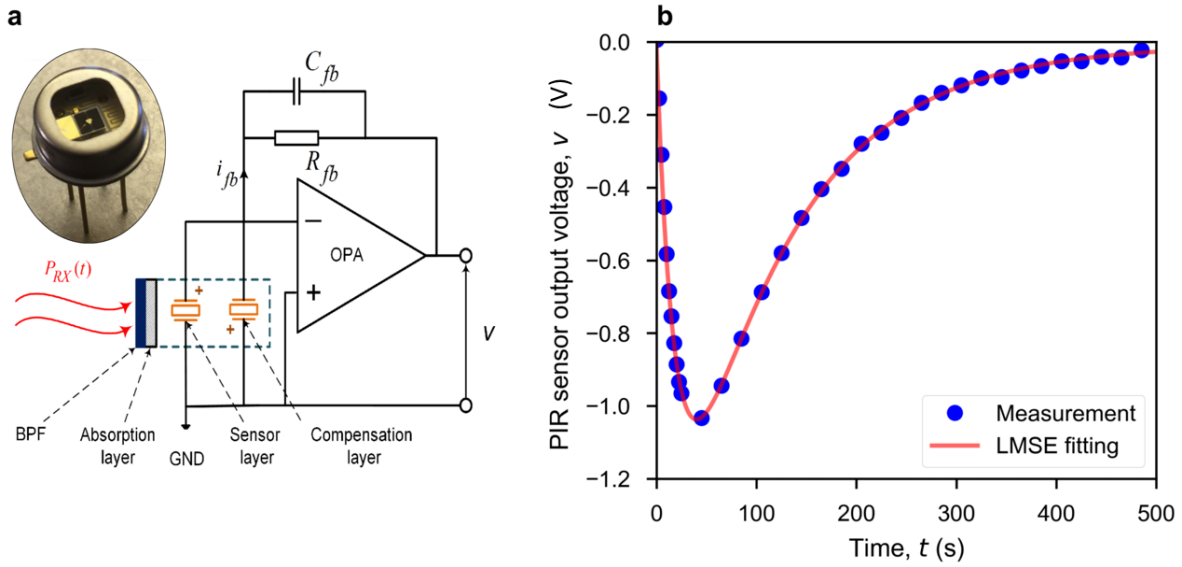


Figure 3.8: Pyroelectric infrared sensor (LME-335): (**a**) Equivalent circuit model for all components integrated within the sensor. (**b**) Measured and fitted sensor step response demonstrated for the 2 m single-channel 'THz Torch' wireless link. The incident radiation step excitation is generated by the mechanical shutter and the thermal emitter at its steady-state temperature of 1,023 K.

For detecting the radiation, a channel BPF first rejects out-of-band power, allowing only the in-band radiation to be incident onto the sensor's absorption layer. The resulting temporal temperature gradient generates a pyroelectric current by altering the electrical polarization magnitude within the pyroelectric layer. A compensation layer that is not

exposed to the incident radiation is connected in parallel with the sensor, having an inverse polarity to cancel out environmental noise. Current flows through the feedback network of the transimpedance amplifier to give an output voltage. This combination of thermodynamics and transient behaviour of the circuit is represented by equation (3.12).

$$\begin{aligned} \eta_p P_{RX}(t) &= H_p \frac{dT_p(t)}{dt} + G_p T_p(t) \quad (a) \\ q(t) &= pA_p T_p(t) \quad (b) \\ i_{fb}(t) &= \frac{dq(t)}{dt} \quad (c) \\ -i_{fb}(t) &= C_{fb} \cdot \frac{dv(t)}{dt} + \frac{v(t)}{R_{fb}} \quad (d) \end{aligned} \tag{3.12}$$

where η_p is the absorptance of the absorption layer; P_{RX} is the incident radiated power onto the sensor; H_p, G_p and A_p are the heat capacity, thermal conductance, and surface area of the pyroelectric layer, respectively; T_p is the temperature difference between the sensor and its metal encapsulation, which is assumed to be a heatsink at constant ambient temperature; p and q are the pyroelectric coefficient and generated charge, respectively; i_{fb}, R_{fb} and C_{fb} are the feedback current, resistor, and capacitor, respectively; v is the output voltage of the sensor. Equation (3.12a) follows the principle of conservation of energy, where the absorbed radiation power (left-hand side) contributes to the change of sensor temperature and the thermal conduction between the sensor and its encapsulation. The pyroelectric effect is expressed by equation (3.12b). By rearranging equation (3.12), the output voltage can be solved from:

$$\begin{aligned} -\eta_p P'_{RX}(t) &= \frac{H_p C_{fb}}{pA_p} v''(t) + \left[\frac{H_p}{pA_p R_{fb}} + \frac{G_p C_{fb}}{pA_p} \right] v'(t) + \frac{G_p}{pA_p R_{fb}} v(t) \\ P'_{RX}(t) = \frac{dP_{RX}(t)}{dt} \quad v''(t) &= \frac{d^2 v(t)}{dt^2} \quad v'(t) = \frac{dv(t)}{dt} \end{aligned} \tag{3.13}$$

Transforming both sides of equation (3.13) into the Laplace-domain gives:

$$\begin{aligned} &-\eta_p[sP_{RX}(s) - P_{RX}(0)] = \\ &\frac{H_p C_{fb}}{pA_p}[s^2 v(s) - sv(0) - v'(0)] + \left[\frac{H_p}{pA_p R_{fb}} + \frac{G_p C_{fb}}{pA_p}\right][sv(s) - v(0)] + \frac{G_p}{pA_p R_{fb}} v(s) \end{aligned} \tag{3.14}$$

where $v(0)$, $v'(0)$ and $P_{RX}(0)$ are initial conditions within the time-domain. The output voltage $v(s)$ in the Laplace-domain can then be solved and transformed back into the time-domain $v(t)$. However, the incident power P_{RX} does not normally have a closed-form expression in either the time or Laplace domains. As a result, a numerical method has to be employed.

PIR Sensor Estimator

The direct measurement or estimation of all parameters found in equation (3.12) can be problematic. To this end, a novel sensor estimator, based on a step-response measurement, is proposed to calibrate these parameter values.

In the time-domain, step radiation, having a constant power amplitude P_{step}, is defined by:

$$P_{RX}(t) = \begin{cases} 0 & \text{when } t \leq 0 \\ P_{step} & \text{when } t > 0 \end{cases} \tag{3.15}$$

Substituting the Laplace transform of the step incident power $P_{RX}(s) = \frac{P_{step}}{s}$, and initial incident power $P_{RX}(0) = 0$ into equation (3.14), the sensor step response in the Laplace-domain $v_{step}(s)$ is:

$$\begin{aligned} v_{step}(s) &= -\frac{a_1 v(0)s + a_1 v'(0) + a_2 v(0) + \eta_p P_{step}}{a_1 s^2 + a_2 s + a_3} \\ a_1 = \frac{H_p C_{fb}}{pA_p} \quad a_2 &= \frac{H_p}{pA_p R_{fb}} + \frac{G_p C_{fb}}{pA_p} \quad a_3 = \frac{G_p}{pA_p R_{fb}} \end{aligned} \tag{3.16}$$

Transforming the solution back into the time-domain gives:

$$\begin{aligned} v_{step}(t) =& \frac{[G_p R_{fb} C_{fb} v(0) + H_p R_{fb} C_{fb} v'(0) + p A_p R_{fb} \eta_p P_{step}] e^{-\frac{1}{R_{fb} C_{fb}} t}}{H_p - G_p R_{fb} C_{fb}} \\ & - \frac{[H_p v(0) + H_p R_{fb} C_{fb} v'(0) + p A_p R_{fb} \eta_p P_{step}] e^{-\frac{G_p}{H_p} t}}{H_p - G_p R_{fb} C_{fb}} \end{aligned} \tag{3.17}$$

With initial response $v(0) = v'(0) = 0$, equation (3.17) can be simplified to:

$$\begin{aligned} & v_{step}(t) = p_0 \cdot (e^{-p_1 t} - e^{-p_2 t}) \\ & p_0 = \frac{p A_p R_{fb} \eta_p}{H_p (1 - p_2/p_1)} P_{step} \quad p_1 = \frac{1}{R_{fb} C_{fb}} \quad p_2 = \frac{G_p}{H_p} \end{aligned} \tag{3.18}$$

As given in equation (3.18), the step-response includes two exponential terms, corresponding to rising and recovery phases. To estimate the values of $\{p_0, p_1, p_2\}$, one can measure the step-response directly and then fit to equation (3.18). This curve fitting represents a nonlinear least-mean-square-error (LMSE) problem, which can be solved by the Levenberg-Marquard algorithm [153].

To generate the step radiation used for sensor estimation, the mechanical shutter is first closed to block the beam. The emitter is heated-up to its steady-state temperature, and then the shutter is opened to let the constant radiation through. As illustrated in Figure 3.1, the hardware setup for a step response measurement is the same as that for regular data transfer. Therefore, sensor estimation can be performed as a regular routine, making the communications link robust to channel environmental changes and component ageing.

Instead of fitting the measured step response directly to equation (3.18), in practice, an additional term p_3 is added to compensate for any offset voltage from the sensor's back-end circuit. Since this curve fitting is a nonlinear LMSE problem, convergence to the global optimum cannot be guarantee without suitable initial values. While p_1, p_2 and p_3 are solely decided by the PIR sensor and its back-end circuit, p_0 varies with other factors,

such as the emitter power, channel range and optical alignment. With the PIR sensor LME-335, initial values $p_1 = 50$ and $p_2 = 5$ can be estimated using equation (3.18) with the following typical parameter values: $R_{fb} = 100$ GΩ, $C_{fb} = 0.2$ pF, $G_p = 4.32$ mW/K and $H_p = 0.864$ mJ/K, given by the sensor manufacturer. The p_0 and p_3 are initialized to 1.0 and 0.0, respectively. The optimization procedure in the parameter space is illustrated in Figure 3.9. Figure 3.8b shows excellent agreement between the measured and fitted step responses, demonstrating the effectiveness of our thermodynamic pyroelectric model.

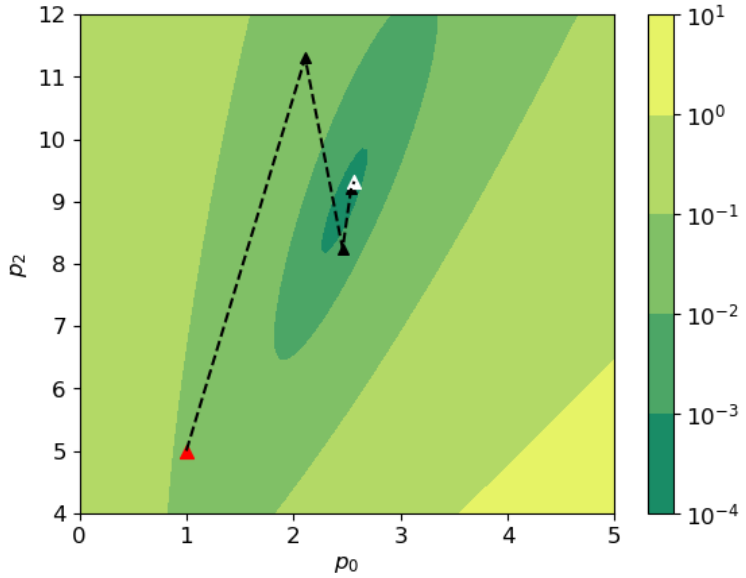


Figure 3.9: Contour plot of the mean-square-error (MSE) function applied for sensor estimation. Here, p_1 and p_2 are not shown for visualization purposes. With the initial values (indicated by the red triangle), the error function is locally convex, and the Levenberg-Marquard algorithm converges to the optimal sensor parameters (indicated by the white triangle) in only four iterations.

With parameters $\{p_0, p_1, p_2\}$, equation (3.13) can be reformulated as:

$$-v''(t) = (p_1 + p_2)v'(t) + p_1 p_2 v(t) + p_0 \hat{P}'_{RX}(p_1 - p_2) \tag{3.19}$$

where $\hat{P}_{RX} = \frac{P_{RX}}{P_{step}}$ is the normalized incident power and $\hat{P}'_{RX}$ is its gradient with respect to time. Calibrated values of $\{p_0, p_1, p_2\}$ now fully define the thermodynamic behavior of

the pyroelectric sensor. The P_{step} can be estimated by:

$$P_{step} = L_c \int_0^{+\infty} p_e(\lambda, T_s)\mathcal{T}_f^2(\lambda)\mathcal{T}_l^2(\lambda)\mathcal{T}_a(\lambda, R_c)d\lambda \tag{3.20}$$

From equation (3.3), $p_e(\lambda, T_s)$ is the thermal emitter power spectral density at steady-state temperature T_s; $\mathcal{T}_l$ is the transmittance of the lens; L_c represents all the uncharacterized frequency-independent losses (e.g., conical horn losses, filter aperture blockage, and misalignment). When the thermal emitter operates at temperature T, the normalized incident power onto the sensor $\hat{P}_{RX}$ is given by:

$$\begin{aligned}\hat{P}_{RX}(T) &= \frac{L_c \int_0^{+\infty} p_e(\lambda, T)\mathcal{T}_f^2(\lambda)\mathcal{T}_l^2(\lambda)\mathcal{T}_a(\lambda, R_c)d\lambda}{P_{step}} \\ &= \frac{\int_0^{+\infty} p_e(\lambda, T)\mathcal{T}_f^2(\lambda)\mathcal{T}_l^2(\lambda)\mathcal{T}_a(\lambda, R_c)d\lambda}{\int_0^{+\infty} p_e(\lambda, T_s)\mathcal{T}_f^2(\lambda)\mathcal{T}_l^2(\lambda)\mathcal{T}_a(\lambda, R_c)d\lambda}\end{aligned} \tag{3.21}$$

In equation (3.21), the unknown term L_c is conveniently cancelled. Moreover, a trapezoidal approximation can be exploited to compute the integration in the numerator numerically. In practice, $\hat{P}_{RX}(T)$ at a fine grid of temperatures from the ambient temperature T_0 to T_s is computed offline and saved in a lookup table. $\hat{P}_{RX}(T)$ at any temperature T can then be obtained using linear interpolation, which significantly reduces the computation cost at runtime.

3.2.4 Thermal Emitter Estimator

This section introduces a thermal emitter estimator to complete the parameter estimation of the entire channel. Obeying the principle of conservation of energy, the following differential equation has been formulated in equation (3.5) to describe the thermodynamics of the emitter:

$$W_e(t) = C_e\frac{dT(t)}{dt} + k_e[T(t) - T_0] + \sigma_e\epsilon A_e T^4(t)$$

where $W_e(t)$ is the thermal emitter's input power, as a function of time t; C_e is the heat capacity of the thermal emitter; $T(t)$ is the transient temperature that varies between the lower extreme limit of the ambient temperature T_0 and its steady-state temperature T_s; k_e collectively represents the thermal conduction and convection; σ_e is the Stefan-Boltzmann constant; ϵ is the emissivity of the emitter; and A_e is the heated surface area of the thin-film thermal emitter.

The values of the relevant parameters, such as W_e, C_e, and k_e, is critical for our cognitive receiver introduced later. In Section 3.2.1, these values are simply estimated from typical specifications given by the manufacturer and, thus, do not take account of variations due to batch-to-batch manufacturing, component aging, and environmental changes. Here, we introduce an optimization-based emitter estimator that does not require hardware changes.

Applying the channel modelling in Section 3.2.1 to 3.2.3, when transmitting a predefined training symbol sequence, the expected noiseless signal can be predicted by iteratively solving a series of differential equations and numerical integration, i.e., equation (3.5), then equation (3.21) and finally equation (3.19). According to the transmitted symbols, $W_e(t)$ is switched between 0 and a constant power W_R under OOK modulation. Assuming the channel filters, atmospheric attenuation and pyroelectric sensor are all adequately characterized, the mean-absolute-error (MAE) between the expected and received signals ($v_{train}[t]$ and $v[t]$, respectively) is a non-analytical function of the emitter parameter values:

$$f(W_R,\ C_e,\ k_e) = \frac{1}{N}\sum_{t=1}^{N} \left| v_{train}[t](W_R,\ C_e,\ k_e) - v[t] \right| \tag{3.22}$$

where W_R is also considered as a parameter to deal with potential power supply drift.

Minimizing this error function gives adaptive emitter parameter values, making the prediction more consistent with the measurement. For solving this optimization problem, we introduce Algorithm 1, which combines gradient descent or Newton-Raphson method

with line search.

Algorithm 1: Gradient Descent/Newton-Raphson with Line Search

Input: Maximal number of iterations I_{max}, maximal learning rate α_{max}, maximal steps of line search J_{max}, initial thermal emitter parameter x_{init} ;
Begin:
$x = x_{init}$;
for $i \leftarrow 0$ **to** I_{max} **do**
    $\nabla_x f(x) = \text{GradientEstimator}(x)$;
    if *use Gradient Descent* **then**
        $\Delta x = \nabla_x f(x)$;
    else
        $\nabla_x^2 f(x) = \text{HessianEstimator}(x)$;
        $\Delta x = [\nabla_x^2 f(x)]^{-1} \nabla_x f(x)$;
    Learning rate $\alpha = \text{LineSearch}(x, \Delta x, \alpha_{max}, J_{max})$;
    $x = x - \alpha \Delta x$;
    break the loop if x converges;
return x;

Algorithm 2: Line Search Subroutine

Input: current value x, attempt direction Δx, maximal learning rate α_{max}, maximal steps of line search J_{max}.
Begin:
$\alpha = \alpha_{max}$;
for $j \leftarrow 0$ **to** J_{max} **do**
    A descent attempt $x_{new} = x - \alpha \Delta x$;
    if $f(x_{new}) \leq f(x)$ **then**
        break the loop;
    else
        reduce the learning rate to $\alpha = 0.8 \times \alpha$;
return α;

Due to the error function is non-analytical, we can only evaluate $f(W_R,\ C_e,\ k_e)$ at any given point $x_0 \doteq (W_{R0},\ C_{e0},\ k_{e0})$ without any knowledge of its gradient vector $\nabla_x f(x_0)$ and Hessian matrix $\nabla_x^2 f(x_0)$. For small scale problems with few parameters, the gradient $\nabla_x f(x)$ and Hessian matrix $\nabla_x^2 f(x)$ required in Algorithm 1 can be approximated by the

finite-difference method given below:

$$\nabla_x f\left(x\right)_i = \frac{\partial f}{\partial x_i} = \frac{f(x + \delta e_i) - f(x)}{\delta} \tag{3.23}$$

$$\nabla_x^2 f\left(x_0\right)_{i,j} = \frac{\partial^2 f}{\partial x_i \partial x_j} = \frac{f(x + \delta e_i + \delta e_j) - f(x + \delta e_i) - f(x + \delta e_j) + f(x)}{\delta^2} \tag{3.24}$$

where e_i are the $i-$th standart unit vector.

In practice, the predefined training sequence for emitter estimation includes four leading $S1$ followed by twenty $S0$, sent at 50 Baud. After timing synchronization (see Section 4.1), the channel estimator calls Algorithm 1 as a subroutine to update the emitter parameters. The parameter values estimated in Section 3.2.1 are used as the initial values x_{init}. To ensure a physically meaningful value, an appropriate box constraint is applied to each emitter parameter. We also normalize each parameter to make them have a similar scale. A small diagonal term may be added to the estimated Hessian matrix when it is not positive definite.

Figure 3.10 shows the result of introducing the thermal emitter estimation using the finite-difference as the gradient and Hessian matrix estimator. It can be seen from the contour plot in Figure 3.10a that the evolution of the optimization process converges into the minimum area of the error function (3.22). Furthermore, the Newton-Raphson algorithm demonstrates a faster convergence rate by exploiting second-order derivatives. As shown in Figure 3.10b, the expected noiseless signal with optimized emitter parameter values gives a better match with the received noisy signal. This clearly demonstrates the adaptive nature of our emitter estimator.

Extended Algorithm for Large-Scale Problems

Although the finite-difference method manages to solve the low-dimensional optimization here, it does not scale-up very well to large-scale problems. For optimizing an objec-

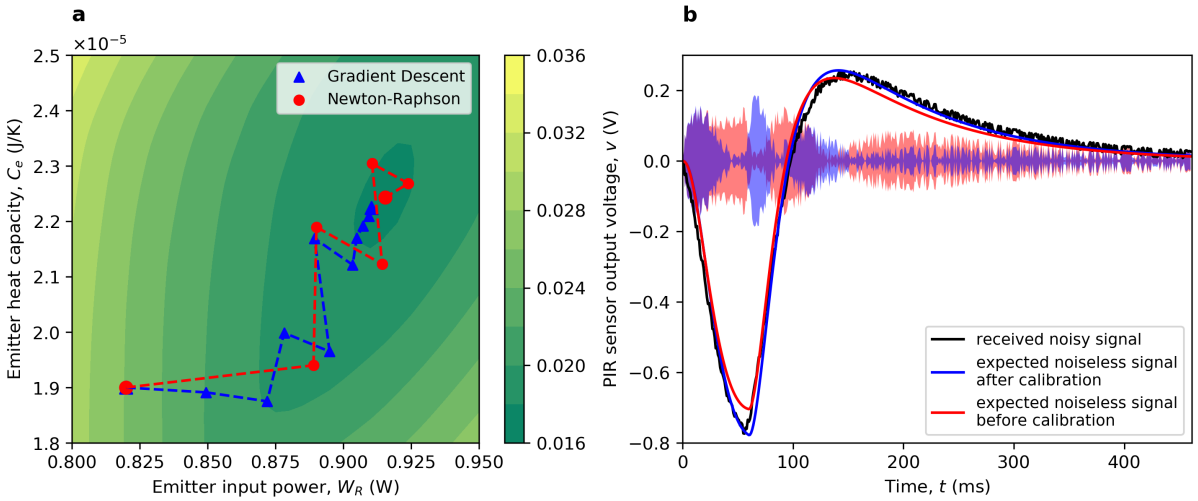


Figure 3.10: Thermal emitter estimation demonstrated for the 2 m single-channel 'THz Torch' wireless link using Algorithm 1 with finite difference: (**a**) Contour plot of the error function in equation (3.22) that depends on W_R and C_e (k_e is fixed to 1.03×10^{-3} W/K for visualization purposes). Optimization progress of the gradient descent and the Newton-Raphson method are indicated by the triangular and circle markers, respectively. (**b**) Synchronized received noisy signal with two expected noiseless signals that adopt the initial and optimized emitter parameter values. For each noiseless expected signal, the absolute error $|error|$ between the expected and measured signals are also shown. For visualization purposes, this is scaled from $-2 \times |error|$ to $+2 \times |error|$.

tive function $f(x)$ with $d-$dimensional variable x, the time complexities (counted by the number of function calls) for the gradient and Hessian estimation are $\mathcal{O}(d)$ and $\mathcal{O}(d^2)$, respectively. The gradient descent algorithm uses only gradient estimation but suffers from slow convergence. In contrast, the Newton-Raphson method has a faster convergence but consumes a large number of function calls for the Hessian matrix estimation. Besides, the finite-difference method is only theoretically meaningful for small perturbation δ and thus not applicable to a noisy objective function. We now extend Algorithm 1 to large scale problems where the complexity of the finite-difference method is no longer acceptable. The main idea is to adopt an evolution strategy in place of the finite-difference.

Evolution strategy [154] is a well developed heuristic derivative-free optimization algorithm. Recent works [155–157] link this method to finite-difference. It forms a gradient estimator at any point x_0 by evaluating the function $f(x)$ at x_0 with added noise vectors

ξ sampled from a diagonal multivariate Gaussian distribution. A brief proof is given as follows.

Proof: Applying a second-order Taylor expansion on $f(x)$ at x_0 gives:

$$f\left(x_0+\xi\right)=f\left(x_0\right)+\ \xi^T\nabla_x f\left(x_0\right)+\frac{1}{2}\xi^T\nabla_x^2 f\left(x_0\right)\xi+O(\xi^3) \tag{3.25}$$

where ξ^T is the transpose of ξ. When sampling ξ from $N(0,\ \sigma^2 I)$, a diagonal multivariate Gaussian distribution with zero-mean and $\sigma^2 I$ covariance matrix, we neglect the higher-order terms $O(\xi^3)$, multiple both sides of equation (3.25) by ξ and take the expectation to give:

$$\begin{aligned}\mathbb{E}_{\xi\sim N(0,\ \sigma^2 I)}\left[\xi f\left(x_0+\xi\right)\right]&\approx\mathbb{E}_{\xi\sim N(0,\ \sigma^2 I)}\left[\xi f\left(x_0\right)+\ \xi\xi^T\nabla_x f\left(x_0\right)+\frac{1}{2}\xi\xi^T\nabla_x^2 f\left(x_0\right)\xi\right]\\&=\ \sigma^2\nabla_x f\left(x_0\right)\end{aligned} \tag{3.26}$$

A Monte Carlo estimator for the gradient can then be constructed by drawing K independent and identical (I.I.D.) samples from $N(0,\ \sigma^2 I)$:

$$\nabla_x f\left(x_0\right)=\frac{1}{K\sigma^2}\sum_{k=1}^{K}\xi_k f\left(x_0+\xi_k\right) \tag{3.27}$$

□

To take advantage of the Newton-Raphson method, having faster convergence, we extend the evolution strategy to Hessian matrix estimation [158]:

$$\nabla_x^2 f\left(x_0\right)\approx\frac{1}{\sigma^2}\mathbb{E}_{\xi\sim N(0,\ \sigma^2 I)}\left[\frac{1}{\sigma^2}f(x_0+\xi)\xi\xi^T-f(x_0+\xi)I\right] \tag{3.28}$$

Similarly, a Monte Carlo estimator for the Hessian matrix can be expressed by:

$$\nabla_x^2 f\left(x_0\right) = \frac{1}{K\sigma^2} \sum_{k=1}^{K} \frac{1}{\sigma^2} f\left(x_0 + \xi_k\right) \xi_k \xi_k^T - f\left(x_0 + \xi_k\right) I \tag{3.29}$$

Here, we can recycle the sampled $\{\xi_k\}_{k=1}^K$ and function evaluations $\{f(x_0+\xi_k)\}_{k=1}^K$ used for the gradient estimation in equation (3.27). Unlike the finite-difference method, theoretically, the Hessian estimator does not require an extra computational cost. In addition, the complexity of the evolution strategy is decided by the number of noise samples K and not directly dependent on the variable dimension d. Therefore, K can be chosen appropriately to achieve a good trade-off between the accurate and speed. Algorithm 3 summarizes the evolution strategy based gradient and Hessian estimators, which can be directly combined with the Algorithm 1.

Algorithm 3: Evolution Strategy based Gradient/Hessian Estimator

Input: current value $x \in \mathcal{R}^d$, number of noise samples K, noise variance σ^2
Begin:
$\nabla_x f\left(x\right) = 0_{d\times 1}$ and $\nabla_x^2 f\left(x\right) = 0_{d\times d}$;
for $k \leftarrow 0$ **to** K **do**
  sample ξ_k from $\mathcal{N}(0, \sigma^2 I)$ and evaluate $f(x + \xi_k)$;
  $\nabla_x f\left(x\right) = \nabla_x f\left(x\right) + \xi_k f(x + \xi_k)$;
  $\nabla_x^2 f\left(x\right) = \nabla_x^2 f\left(x\right) + \frac{1}{\sigma^2} f\left(x_0 + \xi_k\right) \xi_k \xi_k^T - f\left(x_0 + \xi_k\right) I$;
$\nabla_x f\left(x\right) = \frac{1}{K\sigma^2} \nabla_x f\left(x\right)$ and $\nabla_x^2 f\left(x\right) = \frac{1}{K\sigma^2} \nabla_x^2 f\left(x\right)$;
return $\nabla_x f\left(x\right)$ and $\nabla_x^2 f\left(x\right)$;

The detailed proof for equation (3.28) is given below:

Proof: Apply a second-order Taylor approximation on $f(x)$ at x_0, the right-hand-side (RHS) of equation (3.28) can be reformulated as:

$$\begin{aligned} RHS &= \frac{1}{\sigma^2} \mathbb{E}_{\xi\sim\mathcal{N}(0,\sigma^2 I)} \left[\frac{1}{\sigma^2} f(x_0 + \xi) \xi\xi^T - f(x_0 + \xi) I \right] \\ &\approx \frac{1}{\sigma^4} \mathbb{E}_{\xi\sim\mathcal{N}(0,\sigma^2 I)} \left[f(x_0) \xi\xi^T + \xi\xi^T \nabla_x f(x_0) \xi^T + \frac{1}{2} \xi\xi^T \nabla_x^2 f\left(x_0\right) \xi\xi^T \right] \\ &\quad - \frac{1}{\sigma^2} \mathbb{E}_{\xi\sim\mathcal{N}(0,\sigma^2 I)} \left[f(x_0) I + \xi^T \nabla_x f(x_0) I + \frac{1}{2} \xi^T \nabla_x^2 f\left(x_0\right) \xi I \right] \end{aligned} \tag{3.30}$$

Now, we study each term in the RHS of equation (3.30) separately. To facilitate the further derivation, we define the following notations:

$$g = \nabla_x f(x_0) \qquad H = \nabla_x^2 f(x_0)$$
$$A = \xi\xi^T g\xi^T \qquad B = \xi\xi^T H\xi\xi^T$$
$$C = \xi^T H\xi$$

Starting with A, the component at i-th row and j-th column in A can be written as:

$$A_{i,j} = \sum_{n=1}^{d} \xi_i\xi_j\xi_n g_n \tag{3.31}$$

where ξ_i and g_i are the i-th components in ξ and g, respectively. d is the dimension of ξ which is same as the number of the emitter parameters. We now consider two cases:

Case 1: When $i = j = n$, we have:

$$\mathbb{E}_{\xi\sim\mathcal{N}(0,\sigma^2 I)}[\xi_i\xi_j\xi_n g_n] = g_n\mathbb{E}_{\xi\sim\mathcal{N}(0,\sigma^2 I)}[\xi_i^3] = g_n\mathbb{E}_{\xi_i\sim\mathcal{N}(0,1)}[\xi_i^3] = 0 \tag{3.32}$$

Case 2: When at least one of i, j, n are unique, we assume that i is unique without loss of generality:

$$\mathbb{E}_{\xi\sim\mathcal{N}(0,\sigma^2 I)}[\xi_i\xi_j\xi_n g_n] = g_n\mathbb{E}_{\xi\sim\mathcal{N}(0,\sigma^2 I)}[\xi_j\xi_n]\cdot\mathbb{E}_{\xi_i\sim\mathcal{N}(0,1)}[\xi_i] = 0 \tag{3.33}$$

Therefore, we conclude that $\mathbb{E}_{\xi\sim\mathcal{N}(0,\sigma^2 I)}[A_{i,j}] = \mathbb{E}_{\xi\sim\mathcal{N}(0,\sigma^2 I)}\left[\sum_{n=1}^{d}\xi_i\xi_j\xi_n g_n\right] = 0$ for any i, j. Equivalently, $\mathbb{E}_{\xi\sim\mathcal{N}(0,\sigma^2 I)}[A] = 0_{d\times d}$.

Continuing with the next term B, the (i, j) component of B can be written as:

$$B_{i,j} = \sum_{n=1}^{d}\sum_{m=1}^{d} \xi_i\xi_j\xi_n\xi_m H_{m,n} \tag{3.34}$$

Then we study the diagonal and off-diagonal components separately:

Case 1: For diagonal elements ($i = j$), the derivation can be further divided into three sub-cases as following:

Sub-case 1.1: If $i = j = m = n$,

$$\mathbb{E}_{\xi\sim\mathcal{N}(0,\sigma^2 I)}[\xi_i\xi_j\xi_n\xi_m H_{m,n}] = H_{i,i}\mathbb{E}_{\xi_i\sim\mathcal{N}(0,1)}[\xi_i^4] = 3\sigma^4 H_{i,i} \tag{3.35}$$

Sub-case 1.2: If $i = j \neq m = n$,

$$\mathbb{E}_{\xi\sim\mathcal{N}(0,\sigma^2 I)}[\xi_i\xi_j\xi_n\xi_m H_{m,n}] = H_{m,m}\mathbb{E}_{\xi_i\sim\mathcal{N}(0,1)}[\xi_i^2]\cdot\mathbb{E}_{\xi_m\sim\mathcal{N}(0,1)}[\xi_m^2] = \sigma^4 H_{m,m} \tag{3.36}$$

Sub-case 1.3: If $m \neq n$, we assume $i = j \neq m$ without loss of generality:

$$\mathbb{E}_{\xi\sim\mathcal{N}(0,\sigma^2 I)}[\xi_i\xi_j\xi_n\xi_m H_{m,n}] = H_{m,n}\mathbb{E}_{\xi_m\sim\mathcal{N}(0,1)}[\xi_m]\cdot\mathbb{E}_{\xi\sim\mathcal{N}(0,\sigma^2 I)}[\xi_i\xi_j\xi_n] = 0 \tag{3.37}$$

Based on sub-cases 1.1 to 1.3, we can conclude that the expectation of the diagonal component $B_{i,i}$ is:

$$\mathbb{E}_{\xi\sim\mathcal{N}(0,\sigma^2 I)}[B_{i,i}] = \mathbb{E}_{\xi\sim\mathcal{N}(0,\sigma^2 I)}\left[\sum_{n=1}^{d}\sum_{m=1}^{d}\xi_i\xi_i\xi_n\xi_m H_{m,n}\right] = 2\sigma^4 H_{i,i} + \sigma^4 Tr(H) \tag{3.38}$$

where $Tr(\cdot)$ is the operator to get the trace of a matrix.

Case 2: For off-diagonal elements ($i \neq j$), the derivation can also be split into three sub-cases as following:

Sub-case 2.1: If $i = m \neq j = n$,

$$\mathbb{E}_{\xi\sim\mathcal{N}(0,\sigma^2 I)}[\xi_i\xi_j\xi_n\xi_m H_{m,n}] = H_{i,j}\mathbb{E}_{\xi_i\sim\mathcal{N}(0,1)}[\xi_i^2]\cdot\mathbb{E}_{\xi_j\sim\mathcal{N}(0,1)}[\xi_j^2] = \sigma^4 H_{i,j} \tag{3.39}$$

Sub-case 2.2: If $i = n \neq j = m$,

$$\mathbb{E}_{\xi\sim\mathcal{N}(0,\sigma^2 I)}[\xi_i\xi_j\xi_n\xi_m H_{m,n}] = H_{j,i}\mathbb{E}_{\xi_i\sim\mathcal{N}(0,1)}[\xi_i^2]\cdot\mathbb{E}_{\xi_j\sim\mathcal{N}(0,1)}[\xi_j^2] = \sigma^4 H_{j,i} \tag{3.40}$$

Sub-case 2.3: If at least one of m, n is not equal to i and j, we have a case which is similar to sub-case 1.3:

$$\mathbb{E}_{\xi\sim\mathcal{N}(0,\sigma^2 I)}[\xi_i\xi_j\xi_n\xi_m H_{m,n}] = H_{m,n}\mathbb{E}_{\xi_m\sim\mathcal{N}(0,1)}[\xi_m]\cdot\mathbb{E}_{\xi\sim\mathcal{N}(0,\sigma^2 I)}[\xi_i\xi_j\xi_n] = 0 \tag{3.41}$$

Summarizing sub-cases 2.1 to 2.3 and using the fact that the Hessian matrix H is symmetric, the expectation of the (i, j) off-diagonal element in B is given by:

$$\mathbb{E}_{\xi\sim\mathcal{N}(0,\sigma^2 I)}[B_{i,j}] = \mathbb{E}_{\xi\sim\mathcal{N}(0,\sigma^2 I)}\left[\sum_{n=1}^{d}\sum_{m=1}^{d}\xi_i\xi_j\xi_n\xi_m H_{m,n}\right] = 2\sigma^4 H_{i,j} \tag{3.42}$$

Following the derivation above, the expectation of C can be obtained

$$\mathbb{E}_{\xi\sim\mathcal{N}(0,\sigma^2 I)}\left[\sum_{i=1}^{d}\sum_{i=1}^{d}\xi_i\xi_j H_{i,j}\right] = \sigma^2 Tr(H) \tag{3.43}$$

The expectations of rest terms in equation (3.30) are straight-forward as listed below:

$$\begin{aligned}\mathbb{E}_{\xi\sim\mathcal{N}(0,\sigma^2 I)}\left[f(x_0)\xi\xi^T\right] &= \sigma^2 f(x_0)I\\ \mathbb{E}_{\xi\sim\mathcal{N}(0,\sigma^2 I)}\left[f(x_0)I\right] &= f(x_0)I\\ \mathbb{E}_{\xi\sim\mathcal{N}(0,\sigma^2 I)}\left[\xi^T\nabla_x f(x_0)I\right] &= 0_{d\times d}\end{aligned} \tag{3.44}$$

Equation (3.28) can then be proved by substituting all intermediate results above into equation (3.30).

□

Figure 3.11 shows the thermal emitter estimation using Algorithm 1 with the evolution

strategy. Although the finite-difference method is comparable in this simple case, gradient and Hessian estimators introduced in this section open the opportunity to generalize the algorithm for channel estimation in large-scale communications systems. Other advantages of using the evolution strategy can be seen in [156, 157].

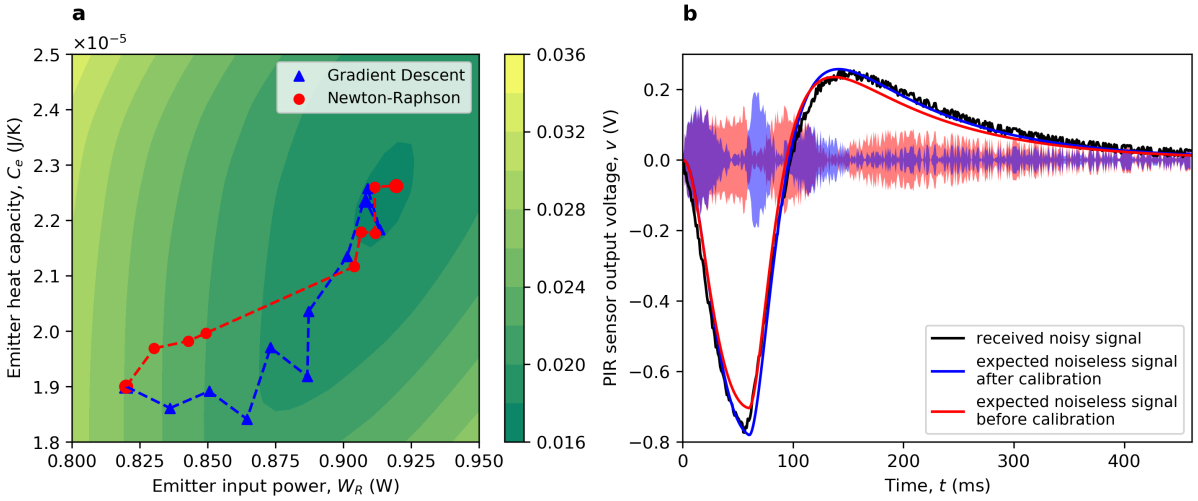


Figure 3.11: Thermal emitter estimation demonstrated for the 2 m single-channel 'THz Torch' wireless link using Algorithm 1 with the evolution strategy: (**a**) Contour plot of the error function in equation (3.22). Optimization progress of the gradient descent and the Newton-Raphson methods are indicated by the triangular and circle markers, respectively. (**b**) Synchronized received noisy signal with two expected noiseless signals that adopt the initial and optimized emitter parameter values. For each noiseless expected signal, the absolute error $|error|$ between the expected and measured signals are also shown. For visualization purposes, this is scaled from $-2 \times |error|$ to $+2 \times |error|$.

3.3 Noise Analysis

In practice, unwanted intrinsic and environmental noise are also injected into the sensor output. The intrinsic noise is introduced by the PIR sensor and its back-end electronics, while the environmental noise sources mainly include microphonic noise, electromagnetic inference, and low-frequency ambient temperature fluctuation.

3.3.1 Intrinsic Noise

Figure 3.12a shows the schematic of the PIR sensor's external back-end electronics (The internal back-end electronics is a built-in transimpedance amplifier as shown in Figure 3.8). A positive and negative low-dropout (LDO) voltage regulator TPS7A39 is exploited as a power supply. The sensor output is buffer by a voltage follower, using the operational amplifier OPA227. The whole circuit is compactly implemented on a four-layer printed circuit board (PCB) whose layout is shown in Figure 3.12b.

The equivalent circuit of the sensor and its electronics, with all associated noise sources, consists of the four blocks shown in Figure 3.13. The noise modelling presented here is adapted from [14, 159, 160].

The first block represents a circuit equivalence of the thermal to electrical conversion process. With thermodynamic modelling, represented by equation 3.12a, the thermal fluctuation noise, also known as phonon noise, has a noise power spectral density $\sqrt{4k_BT_p^2G_p}\,W/\sqrt{Hz}$; This is associated with P_{RX}. The electrical equivalent circuit model analogy ($\equiv$) has a noise current spectral density $I_p \equiv \sqrt{4k_BT_p^2G_p}\;A/\sqrt{Hz}$. The heat capacity H_p (in J/K) and thermal conductance G_p (in W/K) of the PIR sensor turn into their analogous equivalent capacitance $C_p \equiv H_p\;F$ and $R_p \equiv \frac{1}{G_p}\;\Omega$. The variation of the sensor temperature T_p caused by phonon noise will lead to a pyroelectric noise current, which is represented by a voltage-control-current-source (VCCS) whose transfer admittance is given by ωpA_p.

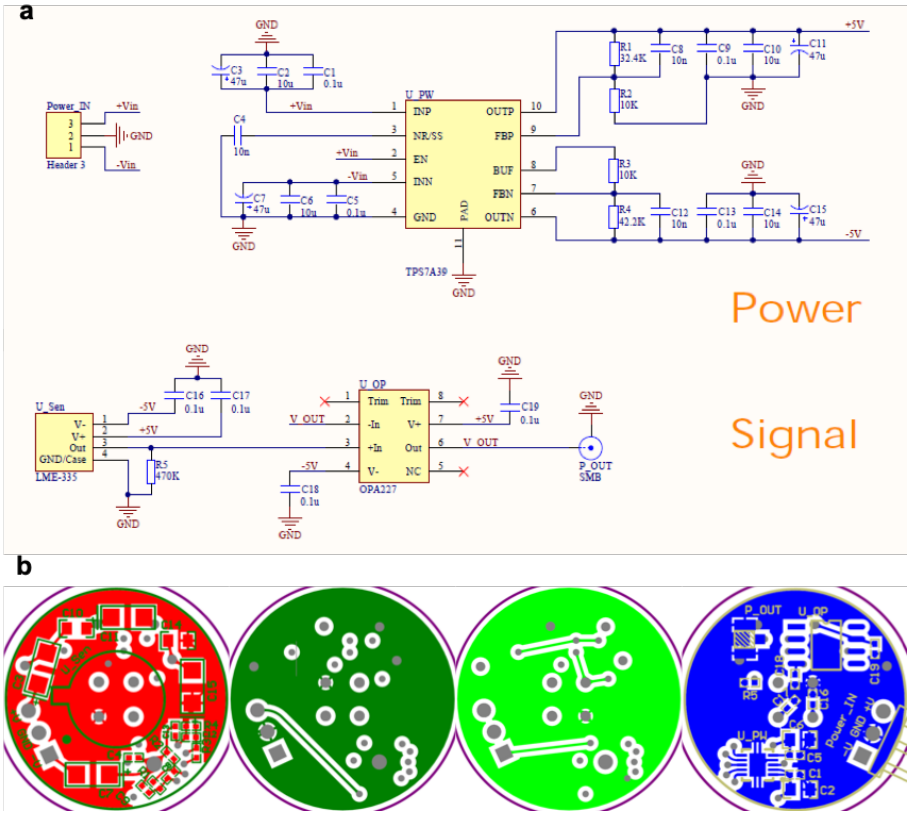


Figure 3.12: External Back-end circuit of the PIR sensor. (**a**) Circuit schematic. (**b**) Four-layer PCB layout.

The second block gives the lumped-element model of the sensor component. C_d is the sensor capacitance and its dielectric loss is represented by the conductance $R_d = \omega C_d tan\delta_d$. Johnson noise current generated by R_d has a noise current spectral density $I_{R_d} = \sqrt{4k_B T_p \omega C_d tan\delta_d}$.

The third block shows the sensor integrated transimpedance amplifier (TIA). C_{TIA} and R_{TIA} are input impedances of the TIA amplifier and $I_{R_{TIA}} = \sqrt{\frac{4k_B T_p}{R_{TIA}}}$ is the Johnson noise generated by R_{TIA}. The amplifier's input noise includes the input noise voltage V_{TIA} and the input noise current I_{TIA}. The input noise current from TIA's positive input to the ground is ignored since it doesn't contribute to the output noise voltage. Considering both flicker $(1/f)$ noise and white noise, the noise voltage spectral density V_{TIA} is given

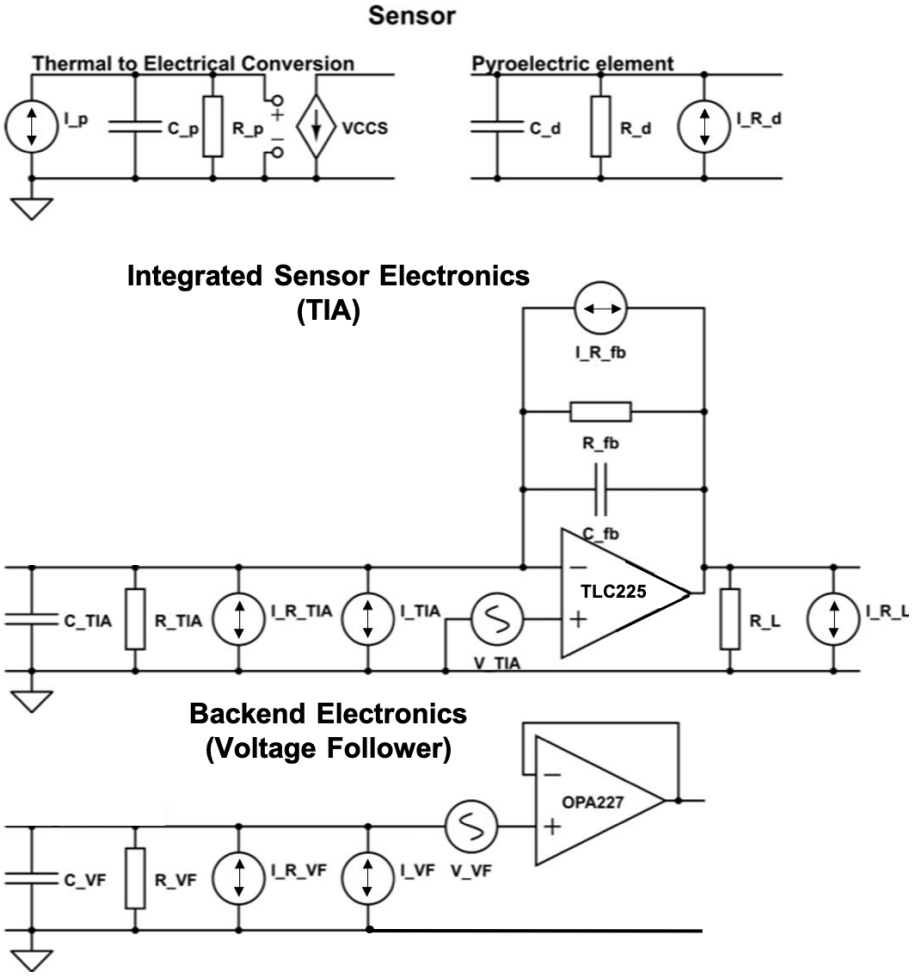


Figure 3.13: Electrical equivalent circuit models for intrinsic noise analysis.

by [161]:

$$V_{TIA} = \sqrt{\frac{10830}{f} + 361} \quad nV/\sqrt{Hz} \tag{3.45}$$

The integrated operational amplifier TLC225 [161] is based on LinCMOS technique, which has a low-input bias-current requirements [162]. Its input noise current is extremely low and the manufacturer only provides a typical value [161]. Therefore, we assume the input current noise is only white with a spectral density equal to the value provided [161]. This assumption is consistent with the measured result in Figure 3.14b. The large feedback resistor R_{fb} also generates Johnson noise, with current spectral density $I_{R_{fb}} = \sqrt{\frac{4k_B T_p}{R_{fb}}}$. The load resistor R_L, with its noise current source, is connected to the TIA output.

The last block is the backend voltage follower stage. The input noise current from the

negative input of the OPA227 to the ground is ignored here, because it does not contribute to the output. The noise voltage spectral density V_{VF}, which includes both flicker and white noise, is given by [163]:

$$V_{VF} = \sqrt{\frac{32.5}{f} + 9} \quad nV/\sqrt{Hz} \tag{3.46}$$

Equation (3.47) to (3.53) express the output noise voltage spectral densities contributed by different noise sources (indicated by the subscripts).

$$U_{I_p} = \omega A_p p \frac{R_{fb}}{G_p} \frac{1}{\sqrt{1+(\omega\tau_p)^2}} \frac{1}{\sqrt{1+(\omega\tau_{fb})^2}} \sqrt{4k_B T_p^2 G_p} \tag{3.47}$$

where $\tau_p = \frac{H_p}{G_p}$ is the thermal time constant of the PIR sensor and $\tau_{fb} = R_{fb}C_{fb}$ represents a 20 ms time constant for this first-order low-pass filter (integrator) associated with the TIA; This corresponds to a -3dB bandwidth of 8Hz shown in Figure 3.14. The values of these two time constants can be calibrated by the sensor estimator introduced in section 3.2.3, recalling that $\tau_p = \frac{1}{p_2}$ and $\tau_{fb} = \frac{1}{p_1}$.

$$U_{R_d} = R_{fb} \frac{1}{\sqrt{1+(\omega\tau_{fb})^2}} \sqrt{4k_B T_p \omega C_d tan\delta_d} \tag{3.48}$$

$$U_{R_{TIA}} = R_{fb} \frac{1}{\sqrt{1+(\omega\tau_{fb})^2}} \sqrt{\frac{4k_B T_p}{R_{TIA}}} \tag{3.49}$$

$$U_{I_{TIA}} = R_{fb} \frac{1}{\sqrt{1+(\omega\tau_{fb})^2}} I_{TIA} \tag{3.50}$$

$$U_{V_{TIA}} = V_{TIA} \frac{R_{fb}}{R'} \sqrt{\frac{1+(\omega\tau')^2}{1+(\omega\tau_{fb})^2}} \tag{3.51}$$

where $R' = R_d//R_{TIA}//R_{fb}$, $C' = C_d + C_{TIA} + C_{fb}$ and $\tau' = R'C'$.

$$U_{R_{fb}} = R_{fb}\frac{1}{\sqrt{1+(\omega\tau_{fb})^2}}\sqrt{\frac{4k_BT_p}{R_{fb}}} \tag{3.52}$$

$$U_{V_{VF}} = V_{VF} \tag{3.53}$$

The output voltage noise contributed by R_L, R_{VF} and I_{VF} is not considered here since the TIA has a low output impedance. Assuming all the noise sources are mutually independent, the overall voltage noise spectral density can be calculated using equation (3.54).

$$U_n = \sqrt{U_{I_p}^2 + U_{R_d}^2 + U_{R_{TIA}}^2 + U_{I_{TIA}}^2 + U_{V_{TIA}}^2 + U_{R_{fb}}^2 + U_{V_{VF}}^2} \tag{3.54}$$

$$V_{n_RMS} = \sqrt{\int_{f_L}^{f_H} U_n^2 \, df} \tag{3.55}$$

Using the parameters listed in Table 3.3, the output voltage noise spectral density and its components are shown in Figure 3.14a. Our simulation predicts a slightly higher noise when comparing to the measurement given by the manufacturer. In the low-frequency region, the main contributors of the output noise voltage include the TIA input resistor R_{TIA}, the TIA input current noise I_{TIA}, and the feedback resistor R_{fb}. All of them start to decay near 10 Hz, and the TIA input voltage noise dominates at higher frequencies. The output root-mean-square (RMS) noise voltage can be calculated by integrating the noise spectral density over the signal bandwidth, as shown in equation (3.55). The peak-to-peak noise voltage will be limited below $6 \times V_{n_RMS}$ with a 99.7% probability.

Table 3.3: Parameters for estimating the output voltage noise spectral density

Parameter	Value	Unit	Reference
A_p	4.0×10^{-6}	m^2	[164]
p	1.7×10^{-4}	$C/K/m^2$	[165]
R_{fb}	1.0×10^{11}	Ω	[164]
C_{fb}	2.0×10^{-13}	F	[164]
G_p	3.1×10^{-3}	W/K	Calculated using $\tau_p = 0.1$ and $H_p = 0.31\ mJ/K$ from [165]
τ_p	1.0×10^{-1}	s	Calibrated
τ_{fb}	2.0×10^{-2}	s	Calibrated
C_d	6.2×10^{-11}	F	[165]
$tan\delta_p$	3.0×10^{-3}	NA	[14]
R_{TIA}	1.0×10^{12}	Ω	[161]
C_{TIA}	8.0×10^{-12}	F	[161]
I_{TIA}	6.0×10^{-16}	$A/\sqrt{Hz}$	[165]
V_{TIA} (1 kHz)	1.9×10^{-8}	$V/\sqrt{Hz}$	[165]
V_{VF} (1 kHz)	3.0×10^{-9}	$V/\sqrt{Hz}$	[163]
T_p	3.0×10^{2}	K	Room temperature assumption

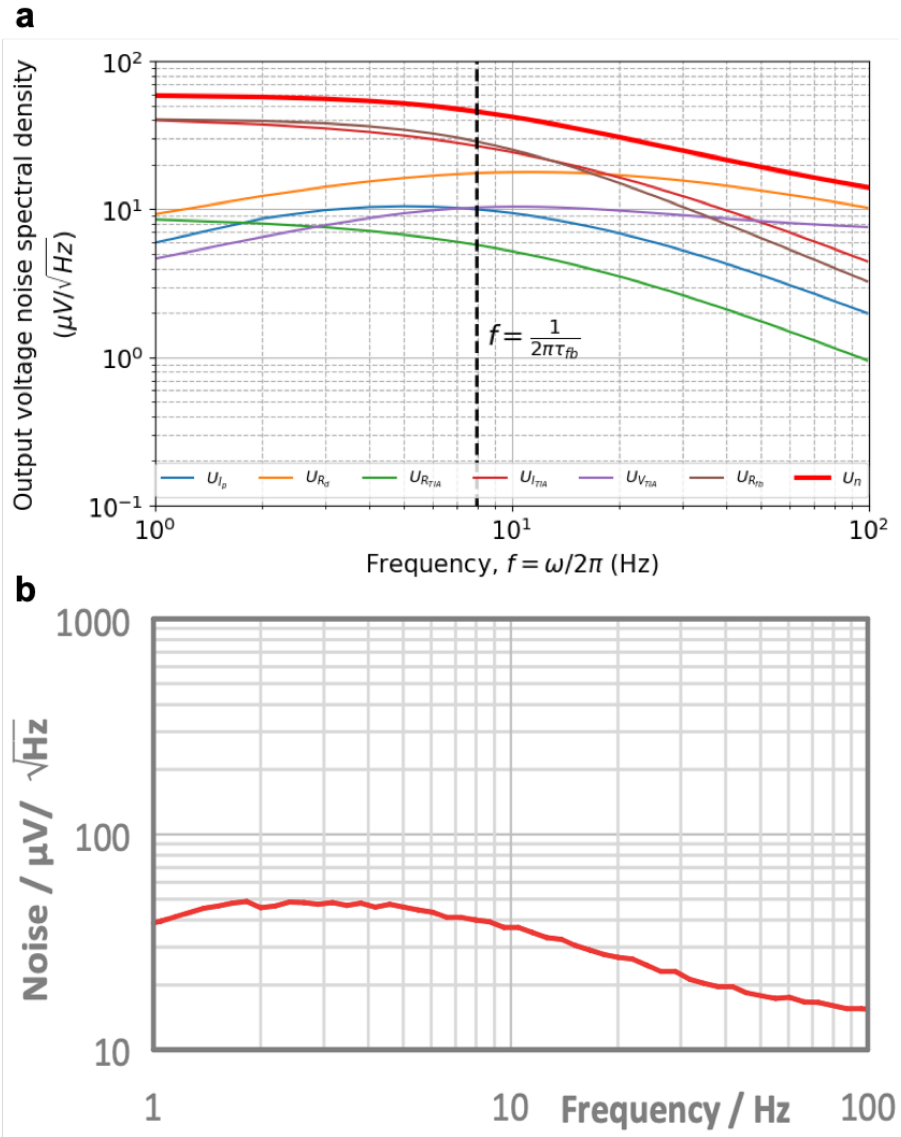


Figure 3.14: (**a**) Calculated output voltage noise spectral density. The noise component $U_{V_{VF}}$ has a low spectral density (not plotted here). (**b**) Measured output voltage noise spectral density from [164].

3.3.2 Environmental Noise

Several environmental noise sources also inject noise into the detector. Since the used pyroelectric material also has the piezoelectric effect, microphonic noise can be produced by mechanical vibration and acoustic noise from the environment. Referring to equation (3.12), a fast change in ambient temperature will change the thermodynamics of the PIR sensor and generate a noise voltage. In addition, electromagnetic interference could be picked up by the sensor and its back-end circuit. A comprehensive study of these noise sources and their influence on system performance is beyond the scope of this paper.

As a qualitative study, Figure 3.15 shows measured noise in three different environments: screen anechoic chamber, as a low environmental noise reference; large air-conditioned office, as a typical indoor environment; and an outdoor environment in low wind conditions. The noise measurement is undertaken by recording the output voltage from the sensor over a period of 20 seconds. The environmental noise is most significant in the outdoor environment, and a noise peak centered at 50 Hz can be observed from both indoor environments, which is attributed to 50 Hz 'mains supply' picked-up.

3.3.3 Noise Reduction

Given the broad frequency spectrum of the intrinsic noise in Figure 3.14, the introduction of an anti-aliasing low-pass filter would provide a significant enhancement to the signal-to-noise ratio. For example, a simple anti-aliasing low-pass filter, having a 2.5 kHz cut-off frequency, was introduced for a sampling frequency of 5 kHz. The background noise was measured up to the Nyquist frequency, shown in Figure 3.16, with and without the filter. From Figure 3.16a, it can be seen that there is a factor of 10.02 reduction in noise voltage, corresponding to a 20 dB reduction in noise power. In practice, the anti-aliasing low-pass filter should be based on a Bessel approximation since a constant differential-phase group

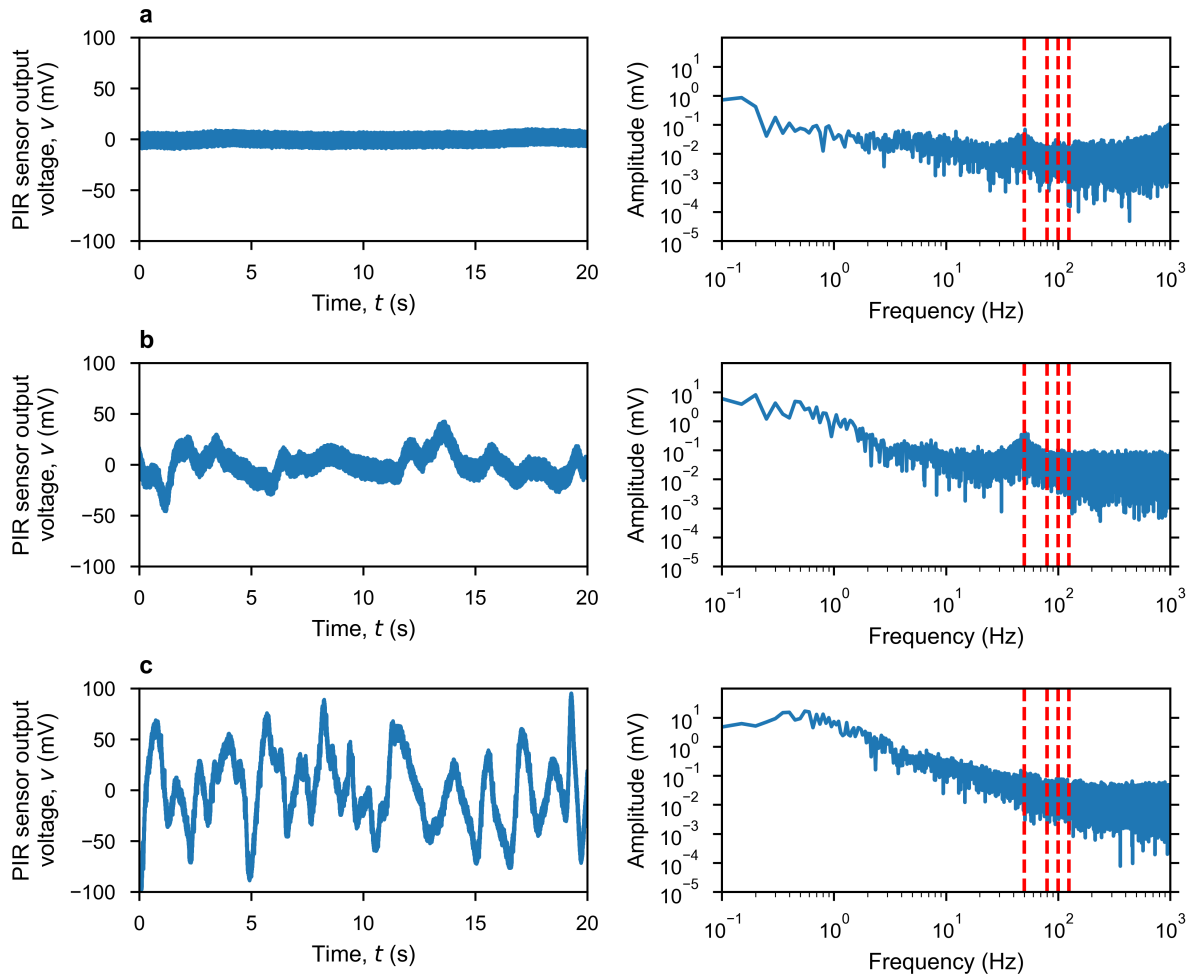


Figure 3.15: Measured noise and associated single-sided amplitude spectral density (dashed red lines indicate different symbol rates) in different environments. (**a**) Inside an electromagnetically-shielded microwave anechoic chamber. (**b**) Large air-conditioned room. (**c**) Outdoors.

delay is required within the signal baseband to maintain the shape of the measured signal. Further works towards an adaptive low-pass baseband filter can be seen in Section 5.2.

The environmental noise, which tends to dominate system performance, needs further investigation. As shown in Figure 3.8a, exploiting a pyroelectric compensation layer can potentially cancel the environmental noise when noises from the compensation layer and the sensor layer are correlated. In addition, the introduction of a 3D-printed shroud (See Figure 3.2) has already shown a significant effect on the reduction of the environmental noise. To mitigate the microphonic noise, anti-vibration material can be employed to

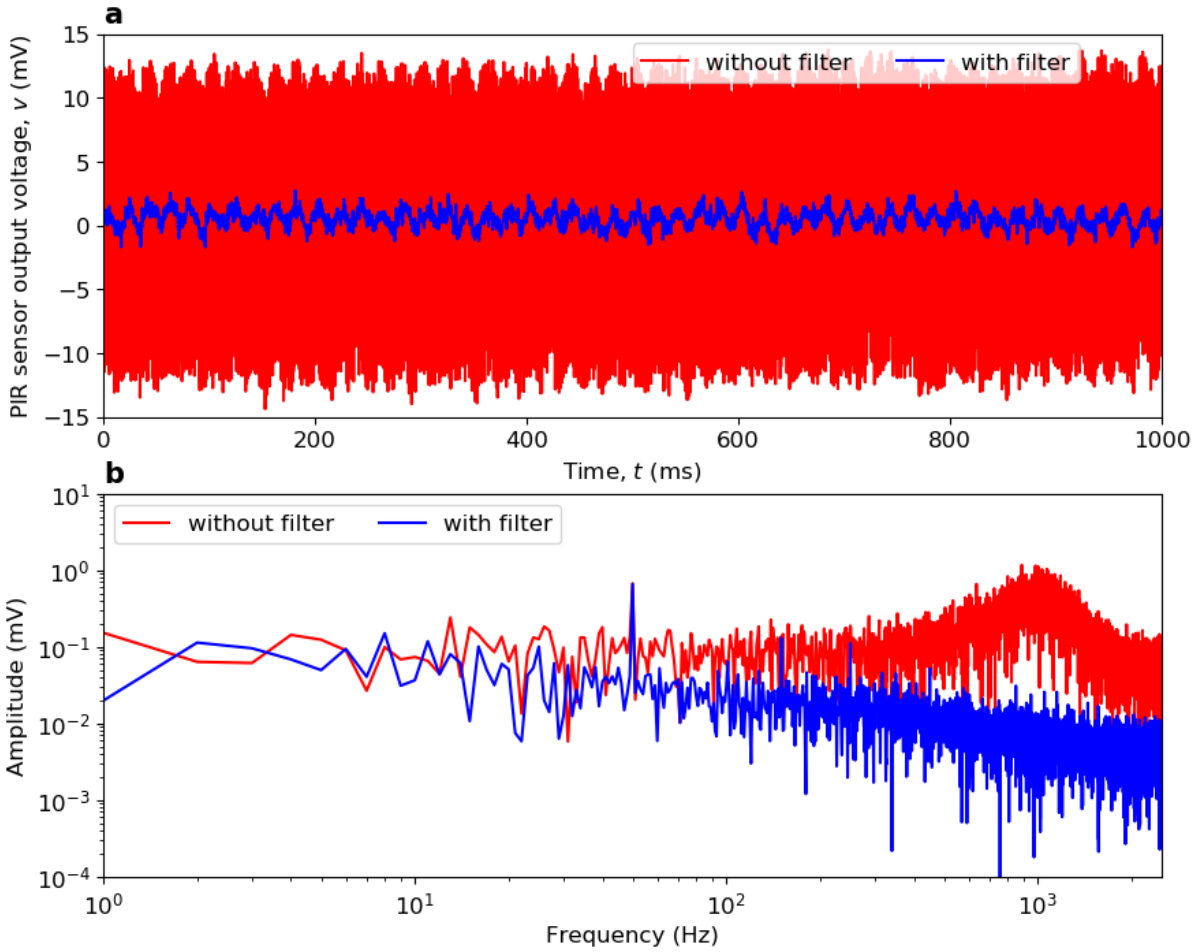


Figure 3.16: Measured background noise over a 1 second period in the laboratory environment with PIR sensor shrouded. (**a**) output noise voltage. (**b**) associated single-sided amplitude spectral density. The red plots represent unfiltered measurements and the blue plots represents the addition of an anti-aliasing filter, inserted between the sensor back-end circuits and ADC, having a cut-off frequency of 2.5 kHz.

package and mount the PIR sensor. In both Figure 3.15 and 3.16b, 'main supply' electromagnetic interference can be seen at 50 Hz. While a great deal of care went into shielding against electromagnetic interference, there is more scope for further investigation.

3.4 Summary

This chapter introduces of the 'THz Torch' wireless link and its system modelling. The channel architecture and an overview of its hardware/software implementations are first

presented. Then, the (thermodynamic) modelling of key building blocks, including a thermal emitter, free space channel and pyroelectric sensor, are undertaken. We focus on the generation, transmission and detection of the spectral radiation during a sequence of thermal transients, which enables the system to operate beyond the thermal time constant. Optimization-based channel estimators are also proposed to calibrate unknown parameters in the developed model, which facilitates the cognitive receiver design in the next chapter. Finally, the noise mechanisms of the sensor and its back-end electronics is carefully investigated. We conduct a quantitative study of the intrinsic noise by exploiting a circuit noise model and a qualitative study of potential environmental noise.

Chapter 4

Cognitive 'THz Torch' Receiver

Based on the thermodynamic model developed in Chapter 3, we introduce the cognitive 'THz Torch' receiver in this chapter. Section 4.1 introduces the receiver architecture including three function blocks: timing synchronization, channel estimation and demodulation. While the channel estimator has been introduced in Chapter 3, a hypothesis testing framework for synchronization and demodulation is given in Section 4.2, followed by two template-matching based algorithms. More advanced algorithms are then presented, including change-point detection for synchronization under parameter mismatch and LSTM-based demodulator for fast and accurate demodulation. Section 4.3 shows measured bit error rate (BER) performances for evaluating and comparing different algorithms in this chapter.

4.1 Receiver Architecture

Figure 4.1 shows the block diagram for the 'THz Torch' transceiver architecture. The upconverter and downconverter, commonly seen in conventional digital communications links, are implicitly included in the thermal emitter and PIR sensor blocks, respectively.

The analog-to-digital converter (ADC) is exploited as a fractionally spaced sampler, with its sampling rate chosen to be an integer multiple of the symbol rate. The timing synchronizer locates the temporal boundary for each predefined training sequence. The demodulator then processes the data frame signals to generate the received symbol sequence. The channel estimator implements the thermal emitter and PIR sensor estimation algorithms introduced in Chapter 3, updating their model parameters from synchronized training signals. The channel estimator's output is sent to the demodulator and the timing synchronizer, improving their future decision-making processes.

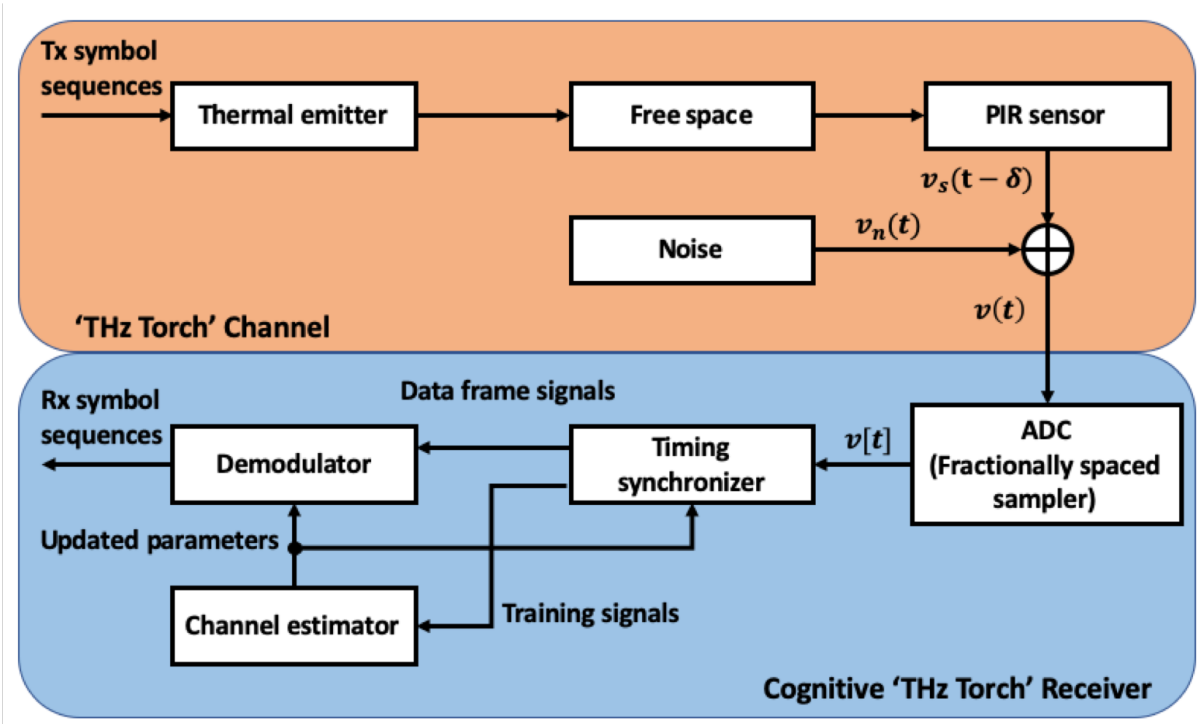


Figure 4.1: Block diagram for the 'THz Torch' transceiver architecture.

4.2 Cognitive Synchronization and Demodulation

4.2.1 Framework

The received discrete baseband signal in Figure 4.1 can be expressed as:

$$v[t] = v_s[t - \delta] + v_n[t] \tag{4.1}$$

where $v_s[t - \delta]$ is a delayed noiseless received signal corresponding to the transmitted symbols; δ represents the time delay; and $v_n[t]$ is the sampled noise. Although the noise mechanism is complicated in our channel (See Section 3.3), a reasonable approximation is that $v_n[t]$ is a sampled white Gaussian noise (WGN) with two-sided power spectral density (PSD) σ_n^2. Equivalently, $v_n[t]$ are a I.I.D. samples from a zero-mean Gaussian distribution $\mathcal{N}(0, \sigma_n^2)$.

Timing synchronization aims at estimating the time delay δ. It is achieved by matching the received signal to the expected noiseless signal (training signal) corresponding to a sequence of predefined symbols. The received signal for synchronization can be written as:

$$v[t] = v_{train}[t - \delta] + v_n[t] \tag{4.2}$$

where $v_{train}[t]$ is the training signal. Timing synchronization can be formulated under the hypothesis testing framework [166]. Given two hypotheses:

$$\begin{aligned} H_{train} &: v[t] = v_{train}[t - \delta] + v_n[t] \\ H_n &: v[t] = v_n[t] \end{aligned} \tag{4.3}$$

where H_{train} is the hypothesis corresponding to the signal model in equation (4.2) and H_n is a noise-only dummy hypothesis; The objective of timing synchronization is to maximize

a likelihood ratio w.r.t δ:

$$\delta^* = arg\max_{\delta} \frac{p_\delta(v|H_{train})}{p(v|H_n)} = arg\max_{\delta} \ log \frac{p_\delta(v|H_{train})}{p(v|H_n)} \tag{4.4}$$

There are three predefined training signals for timing synchronization in our 'THz Torch' wireless link: the sensor estimation signal, which is essentially the step response given in equation (3.18); the emitter estimation signal, which corresponds to a training sequence including four leading $S1$ followed by twenty $S0$, sent at 50 Baud; and the preamble signal, which corresponds to the fixed preamble $\{S1, S1, S1, S0\}$ in each data frame. Training signals for the emitter estimation and the frame preamble can be predicted by solving the differential equation (3.5), then the numerical integration (3.21), and finally the differential equation (3.19). In equation (3.5), W_e is switched between W_R and 0, according to the training sequence. Initial conditions are $T(0) = T_0$ for equation (3.5) and $v'(0) = v(0) = 0$ for equation (3.19).

Once the timing synchronization is established, δ can be removed from equation (4.1) by shifting the expected noiseless signal in time. The synchronized sensor and emitter estimation signals will be processed by the channel estimator to update channel model parameters, and the demodulator is exploited to retrieve the transmitted symbol sequence from each synchronized frame signal.

Assuming a transmitted data frame $\{s_1, s_2, \ ... \ s_N\}$, the overall received signal is:

$$v[t] = \sum_{i=1}^{N} v_{s_i}^{s_{1:(i-1)}}[t - (i-1) \times T_S] + v_n[t] \tag{4.5}$$

where T_S is samples per symbol interval and $v_{s_i}^{s_{1:(i-1)}}[t]$ is the expected noiseless signal of s_i conditioned on all previous symbols $s_{1:(i-1)}$. Given two symbol values $\{S0, \ S1\}$, there

are two hypotheses for $v[t]$ of s_i:

$$\begin{aligned} H_{S0} &: v[t] = v_{S0}^{s_{1:(i-1)}}[t] + v_n[t] \\ H_{S1} &: v[t] = v_{S1}^{s_{1:(i-1)}}[t] + v_n[t] \end{aligned} \tag{4.6}$$

A demodulator that exploits the maximum likelihood decision rule is represented by:

$$s_i^* = arg\max_{s_i}\ p(v|H_{s_i}) = arg\max_{s_i}\ log\ p(v|H_{s_i}) \tag{4.7}$$

The decision rule in equation (4.7) is applied iteratively to demodulate all the symbols in chronological order. Again, $v_{S0}^{s_1:(i-1)}[t]$ and $v_{S1}^{s_1:(i-1)}[t]$ can be obtained using equation (3.5), (3.21) and (3.19). Similarly, we have $W_e = 0$ for $v_{S0}^{s_1:(i-1)}[t]$ and $W_e = W_R$ for $v_{S1}^{s_1:(i-1)}[t]$ with the OOK modulation. Here, the initial conditions $T(0)$, $v(0)$ and $v'(0)$ are decided by all previous symbols $s_{1:(i-1)}$ within the same frame. Without knowing the true transmitted $s_{1:(i-1)}$, the demodulated symbols for $s_{1:(i-1)}$ are used instead.

The hypothesis testing framework for synchronization and demodulation is commonly used in digital receiver design. However, our concept of the cognitive receiver can be justified for the following two reasons.

- Conventional digital systems rely on linear memoryless modulation. In contrast, with our system, we have a complex memory and nonlinear modulation in which the expected noiseless signal is determined by the current symbol and all previous symbols within the same frame. The $v_{s_i}^{s_{1:(i-1)}}[t]$ term in equation (4.6) shows this dependency by its superscript. Our unique thermal-based transceiver physical layer naturally lends itself to this line code solution. Our solution constantly tracks the channel's thermodynamics to produce all possible hypotheses in equation (4.6).

- All expected noiseless signals used for synchronization and demodulation are implic-

itly dependent on the thermal emitter and PIR sensor parameters. By employing the channel estimator, our solution adaptively estimates these parameters using optimization approaches.

Following the framework developed here, several algorithms implemented in the cognitive 'THz Torch' receiver are introduced in the following sections.

4.2.2 Naive Template Matching

The first algorithm, called naive template matching (NTM), is intuitive. For synchronization, the following optimization problem is solved:

$$\delta^* = arg\min_{\delta} \frac{1}{T_H} \sum_{t=0}^{T_H-1} (v[t] - v_{train}[t-\delta])^2 \tag{4.8}$$

where T_H is an integer representing a sufficiently large time horizon so that the energy of $v_{train}[t-\delta]$ does not depend on the δ. An intuitive explanation for equation (4.8) is that the optimal time delay for timing synchronization minimizes the mean-square-error between the received signal and the delayed noiseless signal. Its counterpart for demodulation is given by:

$$s_i^* = arg\min_{s_i} \frac{1}{T_S} \sum_{t=0}^{T_S-1} (v[t] - v_{s_i}^{s_{1:(i-1)}}[t])^2 \tag{4.9}$$

where T_S is an integer that represents the number of samples per symbol. Equation (4.9) finds the optimal $i-$th symbol s_i^* which minimizes the mean-square-error between the received signal $v[t]$ and the expected noiseless signal corresponding to s_i.

Equation (4.8) and (4.9) can be derived from equation (4.4) and (4.7), respectively. Assuming $v_{train}[t_1]$ and $v_{train}[t_2]$ are independent for $\forall\ t_1, t_2 \in [0, T_H)$, equation (4.4) can be

written as:

$$\begin{aligned}
\delta^* &= arg\max_{\delta}\ log\ \frac{p_\delta(v|H_{train})}{p(v|H_n)} \\
&= arg\max_{\delta}\ \sum_{t=0}^{T_H-1} log\ \mathcal{N}(v[t]|v_{train}[t-\delta],\sigma^2) - \sum_{t=0}^{T_H-1} log\ \mathcal{N}(v[t]|0,\sigma^2) \\
&= arg\max_{\delta}\ \sum_{t=0}^{T_H-1} log\ \mathcal{N}(v[t]|v_{train}[t-\delta],\sigma^2) \\
&= arg\max_{\delta}\ \sum_{t=0}^{T_H-1} \frac{1}{\sqrt{2\pi\sigma^2}} exp\ \left[-\frac{(v[t]-v_{train}[t-\delta])^2}{2\sigma^2}\right] \\
&= arg\min_{\delta}\ \frac{1}{T_H}\sum_{t=0}^{T_H-1}(v[t]-v_{train}[t-\delta])^2
\end{aligned} \tag{4.10}$$

Following the same independent assumption, for equation (4.7), we have:

$$\begin{aligned}
s_i^* &= arg\max_{s_i}\ log\ p(v|H_{s_i}) \\
&= arg\max_{s_i}\ \sum_{t=0}^{T_S-1} log\ \mathcal{N}(v[t]|v_{s_i}^{s_{1:(i-1)}}[t],\sigma^2) \\
&= arg\max_{s_i}\ \sum_{t=0}^{T_S-1} \frac{1}{\sqrt{2\pi\sigma^2}} exp\ \left[-\frac{(v[t]-v_{s_i}^{s_{1:(i-1)}}[t])^2}{2\sigma^2}\right] \\
&= arg\min_{s_i}\ \frac{1}{T_S}\sum_{t=0}^{T_S-1}(v[t]-v_{s_i}^{s_{1:(i-1)}}[t])^2
\end{aligned} \tag{4.11}$$

Figure 4.2 illustrates the demodulation operation of the naive template matching algorithm. Two expected noiseless signals $v_{S0}^{s_1:(i-1)}[t]$ and $v_{S1}^{s_1:(i-1)}[t]$ from equation (3.19) and their intermediate results are shown in black and red, respectively. Timing synchronization using equation (4.12) is shown in Figure 4.4.

When operating in an noisy environment, the mean-square-error in equation (4.8) and (4.9) can be replaced by a mean-absolute-error. Equivalently speaking, the sampled noise $v_n[t]$ now follows a Laplace distribution. Compared with the Gaussian distribution, the Laplace distribution has a heavier tail and is thus more robust to unmodeled noise.

Derivations for this naive template matching assume that any two timestamps in the expected noiseless signal are independent. This assumption does not consider the fact that there are only two possible expected noiseless signals and, thus, timestamps in one expected signal are closely dependent on each other. To overcome this shortcoming, we adapt the signal space and matched filter concepts used in conventional digital communications to our 'THz Torch' system in the next section.

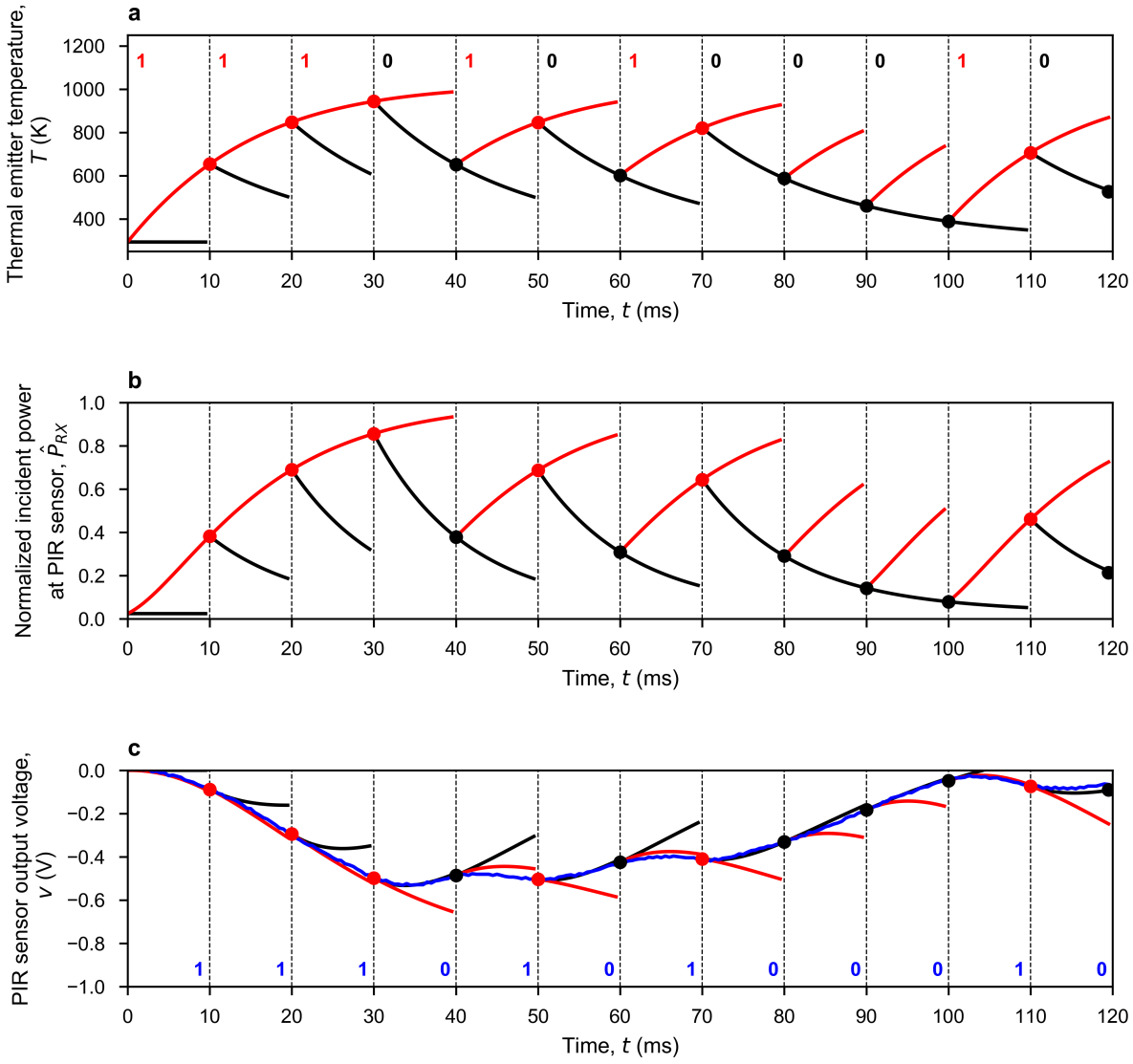


Figure 4.2: Demodulation using the naive template matching algorithm demonstrated for the 2 m single-channel 'THz Torch' wirless link. The transmitted data frame, including the fixed preamble, is a '111010100010' symbol sequence sent at 100 baud. (**a**) Expected thermal emitter temperature, using equation (3.6). (**b**) Expected normalized incident power at the PIR sensor, using equation (3.21). (**c**) Expected received noiseless signals (black for $v_{S0}^{s_1:(i-1)}[t]$ and red for $v_{S1}^{s_1:(i-1)}[t]$) and received signal with noise (blue). The resulting demodulated symbol sequence shows no errors.

4.2.3 Matched Filter

The matched filter (MF), as a workhorse in digital communication receivers, can be used in our 'THz Torch' receiver with only minor modifications. The matched filter based synchronization and demodulation are expressed in equation (4.12) and (4.13), respectively.

$$\delta^* = arg\max_{\delta} (v * \mathcal{M}_{train})[\delta] = arg\max_{\delta} \langle v[t], v_{train}[t-\delta] \rangle \tag{4.12}$$

where $\mathcal{M}_{train}[t] = v_{train}[-t]$ is the matched filter for $v_{train}[t]$; $(*)$ is the convolution operator; and $\langle , \rangle$ is the inner product operator.

$$\begin{aligned} s_i^* &= arg\max_{s_i} (v * \mathcal{M}_{s_i}^{s_{1:(i-1)}})[0] - \frac{\langle v_{s_i}^{s_{1:(i-1)}}[t], v_{s_i}^{s_{1:(i-1)}}[t] \rangle}{2} \\ &= arg\max_{s_i} \langle v[t], v_{s_i}^{s_{1:(i-1)}}[t] \rangle - \frac{\| v_{s_i}^{s_{1:(i-1)}} \|^2}{2} \end{aligned} \tag{4.13}$$

where $\| \cdot \|^2$ represents the energy of a signal. Unlike conventional matched filters, $\mathcal{M}_{s_i}^{s_{1:(i-1)}}[t]$ in equation (4.13) now varies with the previously transmitted symbols. Furthermore, all matched filters can perceive the system variation by employing the estimated sensor and emitter parameters.

The matched filter algorithm is essentially an extension of the naive template matching to a signal space. Since there are only two possible expected noiseless signals, a low dimensional signal space can be constructed, and each hypothesis in equation (4.3) and (4.6) can be projected to a Gaussian distribution in the signal space. Conditional likelihoods in equation (4.4) and (4.7) are simplified to probabilities under these projected Gaussian distributions. Any noise signal component, which is orthogonal to the signal space, has no contribution to the result and can, thus, be dropped. Besides, the matched filter remains optimal when there is a scaling factor between the predicted and the real expected noiseless signal.

Figure 4.3 illustrates the matched filter hypotheses in signal space. For synchronization,

the signal space is one-dimensional with a basis $\phi_{syn}[t] = \frac{v_{train}[t-\delta]}{\|v_{train}[t-\delta]\|}$. Two hypotheses H_{train} and H_n are projected to $\mathcal{N}(\|v_{train}[t-\delta]\|, \sigma_n^2)$ and $\mathcal{N}(0, \sigma_n^2)$, respectively. The projection of the received signal $v[t]$ onto the signal space is $\langle \phi_{syn}[t], v[t] \rangle$. Equation (4.12) is equivalent to maximizing the likelihood ratio w.r.t the time delay δ:

$$log\ \frac{p_\delta(v|H_{train})}{p(v|H_n)} = log\ \frac{\mathcal{N}(\langle \phi_{syn}[t], v[t] \rangle | \|v_{train}[t-\delta]\|, \sigma_n^2)}{\mathcal{N}(\langle \phi_{syn}[t], v[t] \rangle | 0, \sigma_n^2)} \tag{4.14}$$

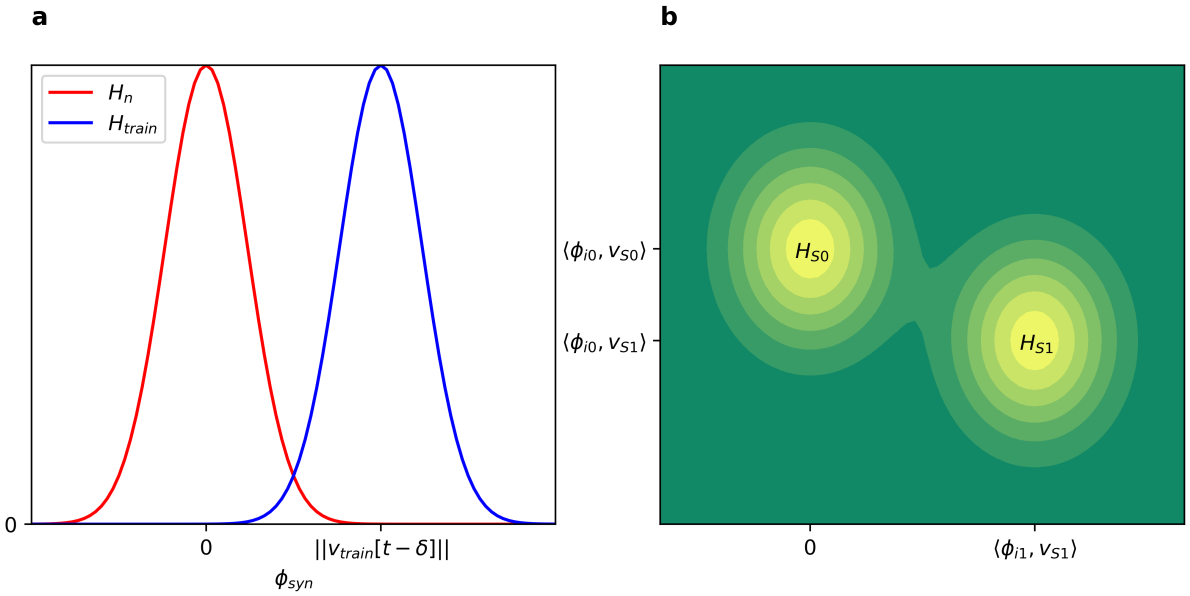


Figure 4.3: Matched filter hypotheses in signal spaces. (**a**) One dimensional signal space for synchronization. (**b**) Two dimensional signal space (varying from symbol to symbol) for demodulation.

For demodulating the $i-$th symbol, the signal space is two-dimensional with the basis $\phi_{i0}[t]$ and $\phi_{i1}[t]$, calculated using Gramm-Schmidt orthogonalization:

$$\begin{aligned}
\phi_{i0}[t] &= \frac{v_{S0}^{s_{1:(i-1)}}[t]}{\|v_{S0}^{s_{1:(i-1)}}[t]\|} \\
\phi'_{i1}[t] &= v_{S1}^{s_{1:(i-1)}}[t] - \langle v_{S1}^{s_{1:(i-1)}}[t], \phi_{i0}[t] \rangle \cdot \phi_{i0}[t] \\
\phi_{i1}[t] &= \frac{\phi'_{i1}[t]}{\|\phi'_{i1}[t]\|}
\end{aligned} \tag{4.15}$$

Hypotheses H_{S0} and H_{S1} in equation (4.6) are mapped to two Gaussian distributions:

$$\begin{aligned} H_{S0}: \ \mathcal{N}\Bigg(\begin{bmatrix} \langle \phi_{i0}[t], v_{S0}^{s_{1:(i-1)}}[t] \rangle \\ 0 \end{bmatrix}, \ \sigma_n^2 I \Bigg) \\ H_{S1}: \ \mathcal{N}\Bigg(\begin{bmatrix} \langle \phi_{i0}[t], v_{S1}^{s_{1:(i-1)}}[t] \rangle \\ \langle \phi_{i1}[t], v_{S1}^{s_{1:(i-1)}}[t] \rangle \end{bmatrix}, \ \sigma_n^2 I \Bigg) \end{aligned} \tag{4.16}$$

The projection of the received signal $v[t]$ onto the signal space is given by:

$$\begin{bmatrix} \langle \phi_{i0}[t], v[t] \rangle \\ \langle \phi_{i1}[t], v[t] \rangle \end{bmatrix} \tag{4.17}$$

The decision rule in equation (4.13) essentially chooses the hypothesis which assigns the largest probability to the received signal projection.

Figure 4.4 illustrates the synchronization achieved by the naive template matching and the matched filter. Compared with the former, the latter's objective in equation (4.12) tends to have a more steep peak at the optimal time delay. Their results are consistent in Figure 4.4a&b and deviate by 2 ms for data frame synchronization in Figure 4.4c.

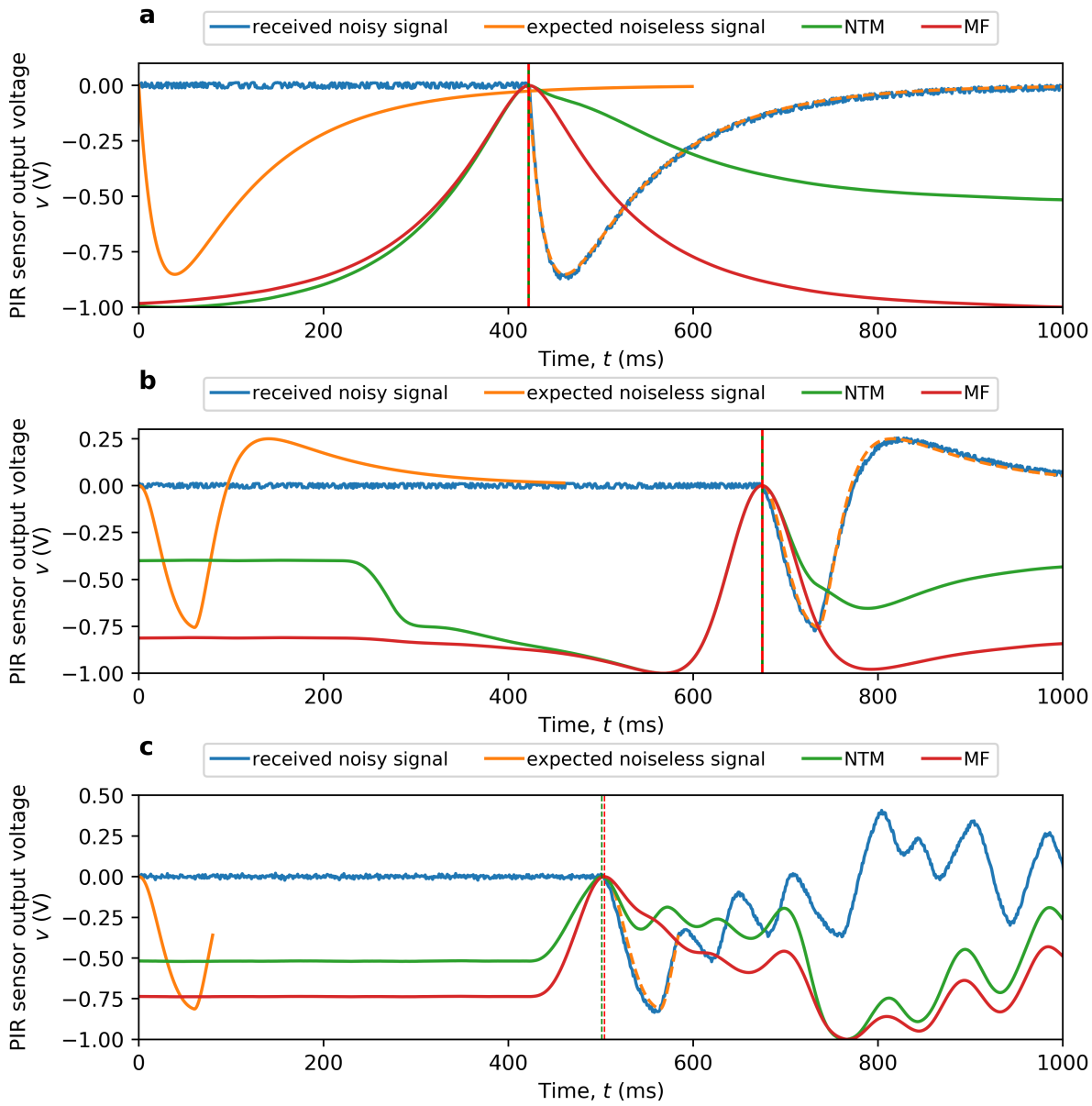


Figure 4.4: Timing synchronization for predefined training signals demonstrated for the 2 m single-channel 'THz Torch' wireless link. The naive template matching (NTM) objective in equation (4.8) and the matched filter (MF) objective in equation (4.12) are scaled and shifted to $[-1, 0]$ for visualization purposes. Each time delay estimation, indicated by a vertical dashed line, is obtained by locating the peak of its corresponding objective function. (**a**) Timing synchronization for PIR sensor estimation. The training sequence is a radiation step and the training signal is the step response of the sensor. (**b**) Timing synchronization for thermal emitter estimation. The training sequence includes four leading $S1$ followed by twenty $S0$, over 480 ms, sent at 50 Baud. (**c**) Timing synchronization for data frame. The training sequence is a fixed data frame preamble $\{S1, S1, S1, S0\}$, with random data following on.

4.2.4 Synchronization under Parameter Mismatch

Timing synchronization locates the temporal boundary for each received signal by searching for the optimal time delay δ. Poor synchronization misaligns the received signal to the transmitted symbol sequence and degrades the performance of channel estimation and demodulation. Two synchronization algorithms, the naive template matching and the matched filter, have been introduced in previous sections. Both are based on template matching and assume the training signal $v_{train}[t]$ corresponding to a predefined training sequence is accurate. However, producing an accurate expected noiseless signal relies on PIR senor and thermal emitter parameters updated by the channel estimator, which means the initial sensor and emitter estimation signals have to be synchronized under parameter mismatch. In this section, a change-point detection approach [167] is exploited to improve timing synchronization for this initial scenario.

Change-point detection for a signal aims at finding some key timestamps at which a pre-defined pattern of the signal shows an abrupt change. It can be formulated as an optimization problem:

$$\min_{\mathcal{I}} \sum_{k=0}^{K-1} c(v[\mathcal{I}_k : \mathcal{I}_{k+1}]) \tag{4.18}$$

where $\mathcal{I}$ is a set of ordered timestamps $\{\mathcal{I}_k\}_{k=0}^{K}$, representing a specific way of segmentation; v is the complete discrete signal of length T_H; while $v[\mathcal{I}_k : \mathcal{I}_{k+1}]$ is one of the segments under $\mathcal{I}$ that includes $v[\mathcal{I}_k]$ and excludes $v[\mathcal{I}_{k+1}]$. For conciseness, $\mathcal{I}_0$ and $\mathcal{I}_K$ are fixed to 0 and T_H, respectively. Also, $c(\cdot)$ is a cost function that defines the changing pattern to be detected. Here, the number of change points $|\mathcal{I}|$ is set to a constant and the cost function is chosen to be:

$$c(v[\mathcal{I}_k : \mathcal{I}_{k+1}]) = \min_{\alpha,\beta} \sum_{t=\mathcal{I}_k}^{\mathcal{I}_{k+1}-1} (v[t] - \beta - \alpha t)^2 \tag{4.19}$$

This means that a piece-wise linear model, with a fixed number of knots, is fitted to the

signal, and these knots are assigned to be the change points.

The improved timing synchronization now includes two phases: the template-matching phase, which achieves coarse synchronization due to the inaccurate training signal produced by initial channel parameters; and the change-point detection phase. With the latter, the optimization problem in equation (4.18) is solved by dynamic programming to obtain a set of change points $\{\mathcal{I}_k^v\}_{k=0}^K$ from the received noisy signal pre-synchronized by the template-matching phase. The revised time delay can be simply decided by $\delta_{cp} = \delta_{tm} + \mathcal{I}_1^v$ where the index of the first change-point, as a correction, is added to the coarse time delay δ_{tm} from the template-matching phase.

The change-point detection phase is time-consuming and, thus, only used for initial sensor and emitter estimation. With the initially estimated channel parameters, the training signals will be accurate enough for simple template-matching based timing synchronization.

Figure 4.5 illustrates the operation of the improved timing synchronization. The emitter and sensor parameters are reset to their initial values when predicting the expected noiseless signal. Due to parameter mismatch, the time delay δ_{tm} given by template-matching based algorithms deviate from the optimal δ^* showed in Figure 4.4a&b. The deviation is then corrected by the change-point detection phase. In Figure 4.5a, $\delta_{tm} = 411$ ms, $\delta_{cp} = 424$ ms and $\delta^* = 422$ ms. In Figure 4.5b, $\delta_{tm} = 669$ ms and $\delta_{cp} = \delta^* = 675$ ms. It shows that the change-point detection is capable of achieving ideal timing synchronization under parameter mismatch.

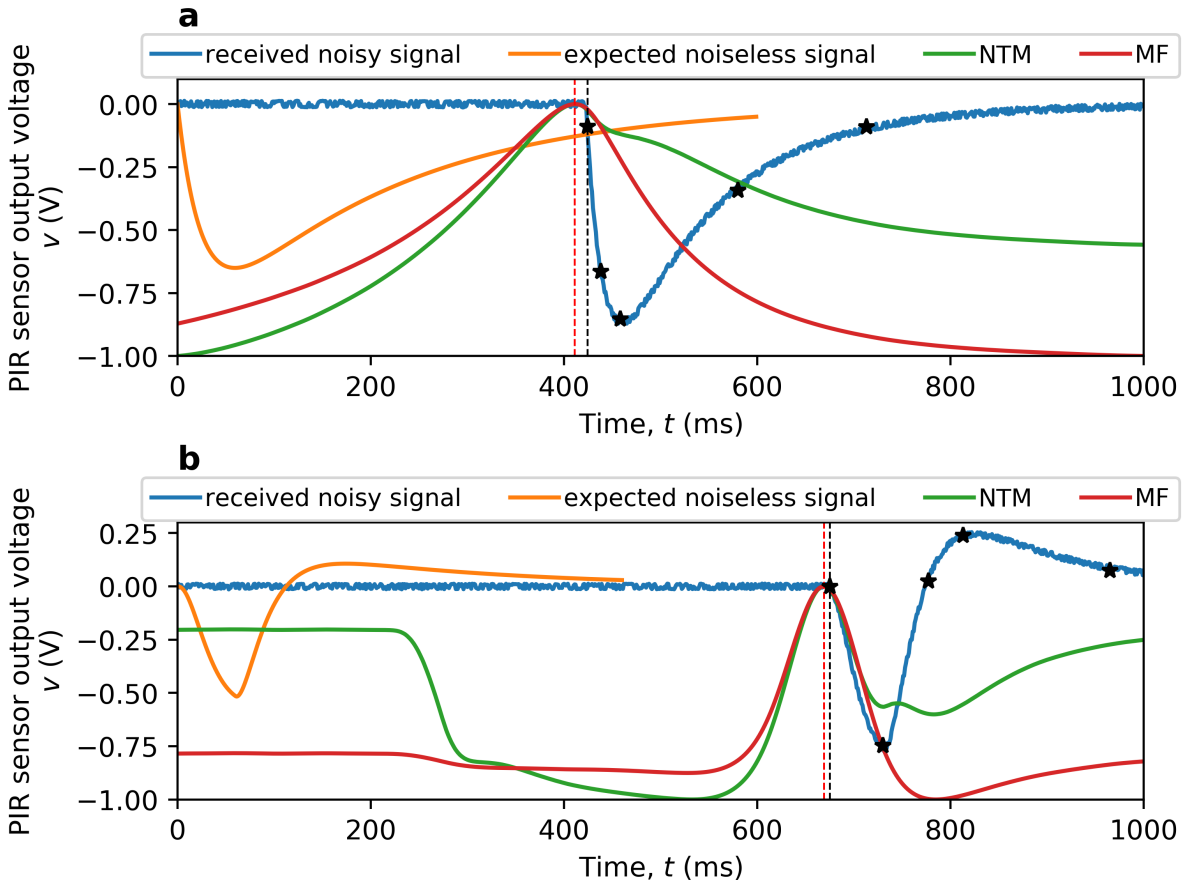


Figure 4.5: Improved timing synchronization using change-point detection demonstrated on the 2 m single-channel 'THz Torch' wireless link. Compared with Figure 4.4a&b, the expected noiseless signal (training signal) in orange is produced by the mismatched emitter and sensor parameters. The coarse time delay δ_{tm} decided by the template-matching phase is indicated by the red dashed line. Black stars represent the detected five change points $\{\mathcal{I}_k^v\}_{k=1}^5$, and the black dashed line indicates the improved timing synchronization δ_{cp} after the change-point detection phase. (**a**) Timing synchronization for initial PIR sensor estimation. The training sequence is a step radiation and the training signal is the step response of the sensor. (**b**) Timing synchronization for initial thermal emitter estimation. The training sequence includes four leading $S1$ followed by twenty $S0$, over 480 ms, sent at 50 Baud.

4.2.5 LSTM-based Demodulator

Combined with thermodynamics-based modelling, template-matching based demodulators introduced in Section 4.2.2 and 4.2.3 are capable of significantly improving the operational figure of merit (Range × Bit Rate) for 'THz Torch' wireless communications links. However, these solutions have several shortcomings:

- As given in equaiton (4.1), the received signal $v[t] = v_s[t - \delta] + v_n[t]$ is distorted by the noise term $v_n[t]$. Due to unmodelled behaviour (e.g., environmental noise) and parameter mismatch (e.g., channel estimation error), the equivalent $v_n[t]$ may not closely follow the WGN assumption, which ultimately degrades the BER performance.

- When predicting expected noiseless signals $v_{S0}^{s_{1:(i-1)}}$ and $v_{S1}^{s_{1:(i-1)}}$, for demodulating the i-th symbol s_i, initial conditions are decided by the demodulation results of its previous symbols $s_{1:(i-1)}$. A error in $s_{1:(i-1)}$ will give the wrong initial condition, which may cause a chain of errors within the sequence.

- When solving differential equations and integrals for $v_{S0}^{s_{1:(i-1)}}$ and $v_{S1}^{s_{1:(i-1)}}$ numerically, there is a trade-off between computational complexity and accuracy. Although real-time communication is achieved with low symbol rates, a more lightweight algorithm is preferred, making it possible to further ease computational hardware requirements.

To address all these shortcomings, we introduce a long short-term memory (LSTM)-based demodulator in this section, which combines the developed thermodynamics-based modelling with the deep learning technique. Unlike template-matching based algorithms, it exploits a maximum a posterior (MAP) rule, which directly approximates the posterior probability $p(s_i = S1|v)$ using a neural network.

Here, the neural network (NN) is essentially an expressive function approximator composed of manually designed, parameterized, and non-linear functions (layers). Since the NN is fully differentiable, its parameters can be learnt by the backpropagation algorithm, which is an application of the 'chain rule' in multivariable calculus. The recurrent neural network (RNN) [168] is a family of neural networks with a special structure tailored for time-series analysis. Input at each step is processed by a shared network, while a concise vectorized representation of the history is extracted and passed forward in time. Here, the Long-Short Term Memory (LSTM) [169], as a standard RNN architecture, is exploited. The complete LSTM-based cognitive demodulator is illustrated in Figure 4.6. Expressions for calculating the intermediate variables in Figure 4.6 are:

$$
\begin{aligned}
&f_i = Sigmoid\left(W_f\left[x_i,\ h_{i-1}\right] + b_f\right)\\
&i_i = Sigmoid\left(W_i\left[x_i,\ h_{i-1}\right] + b_i\right)\\
&g_i = tanh\left(W_g\left[x_i,\ h_{i-1}\right] + b_g\right)\\
&o_i = Sigmoid\left(W_o\left[x_i,\ h_{i-1}\right] + b_o\right)\\
&c_i = f_i \otimes c_{i-1} + i_i \otimes g_i\\
&h_i = o_i \otimes tanh(c_{i-1})\\
&p(s_i = S1|v[0:iT_S], p_s, p_e) = MLP([h_i, p_s, p_e]) =\\
&Sigmoid(W_3(ReLU(W_2(ReLU(W_1[h_i, p_s, p_e] + b_1)) + b_2)) + b_3)
\end{aligned}
\tag{4.20}
$$

where i is used to index symbols in the sequence and $x_i = v[(i-1)T_S : iT_S]$ represents the received noisy signal corresponding to the i-th symbol; $W_{f,i,g,o}$ and $b_{f,i,g,o}$ are internal parameters for the LSTM; $[x_i,\ h_{i-1}]$ represents the concatenation of x_i and h_{i-1}; $Sigmoid\left(x\right) = \left(1 + e^{-x}\right)^{-1}$ is the sigmoid function; and $\otimes$ represents the Hadamard product. For each symbol, the LSTM takes the corresponding synchronized received signal to update its cell state c_i and hidden state h_i from their previous states. While the updated states are passed to the next step, hidden state h_i is concatenated with emitter and sensor

parameters (p_e and p_s). The resulting vector $[h_i, p_e, p_s]$, which includes both the features of the channel and the previously received signal $v[0 : iT_S]$, is forwarded to a multi-layer perception (MLP) to make a probabilistic decision for the current symbol. In practice, we choose the LSTM hidden size (the dimension of h_i and c_i) as 128. The MLP is designed to have three layers: two hidden layers with hidden size 64 and ReLU [170] activation function; output layer with output size 1 and Sigmoid activation function.

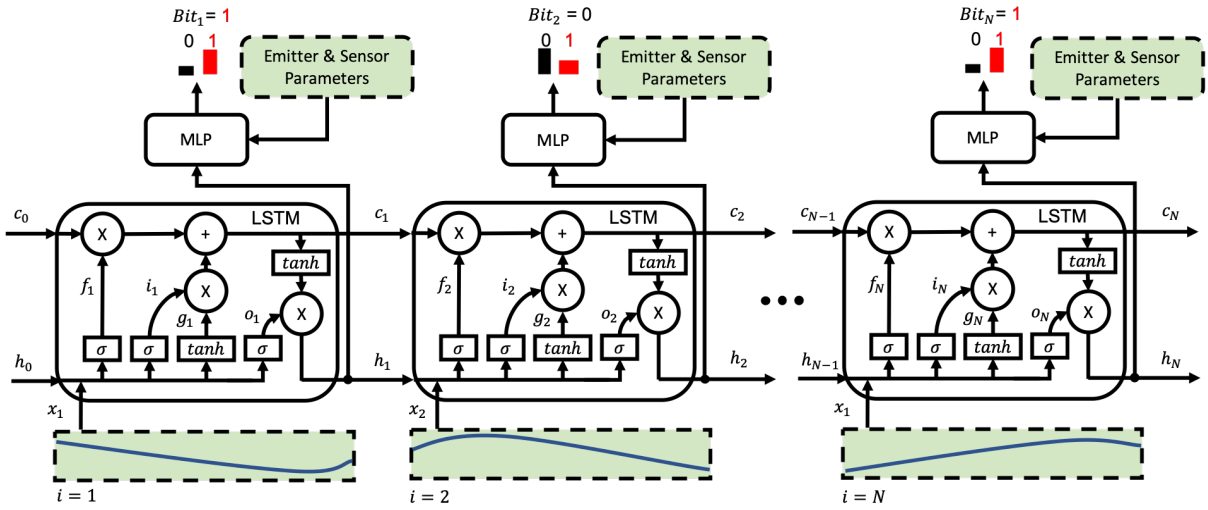


Figure 4.6: Unrolled computational graph for the complete LSTM-based cognitive demodulator with emitter and sensor parameter inputs and received noisy signal (cyan curve) input across a sequence of N symbols.

Two issues that prevent a direct application of the LSTM-based cognitive demodulator are overfitting [171] and domain-shift [172]. While LSTM has the potential to approximate sophisticated mapping from received noisy signals into symbols, it may be overfitted to the collected training dataset instead of capturing the real underlying mapping. The solution is to collect a large training dataset, but this can be time-consuming in a real system. Domain-shift occurs in the LSTM-based cognitive demodulator, as the 'THz Torch' wireless links have variant emitter and sensor parameter values. A conventional learning-based demodulator may work poorly on the channel with parameter values that are not covered by its training dataset. However, the thermodynamics-based model, introduced in Chapter 3, can be employed to solve both the overfitting and domain-shift

issues by building a training dataset through simulations.

Given a data frame containing a fixed preamble and 50 pseudo-randomly generated symbols, the expected noiseless signal $v_{frame}[t]$ can be simulated using our thermodynamics based model, having random values for the emitter and sensor parameters. This is followed by injecting additive white Gaussian noise and potential environmental noise into the simulated signal, giving a $v[t] = v_{frame}[t] + v_n[t]$ which attempts to mimic the received noisy signal from the PIR sensor. We also inject noise into the random-valued sensor and emitter parameters to simulate channel estimation errors. A demodulator training sample consists of the frame, the simulated noisy signal $v[t]$, and the channel parameters; 10,000 of these training samples make up the complete training dataset. Note that, for each training sample, the received noisy signal could be directly measured from the 'THz Torch' wireless link. This would have the advantage of being more realistic (i.e., real-world system, including both internal and external noise contributions). However, collecting the training dataset would be extremely time-consuming if random-valued channel parameters are chosen for each frame.

Once the training dataset has been prepared, all internal parameters are trained to minimize the well-known binary cross-entropy loss function:

$$Loss = -\sum_{n=1}^{N}\sum_{m=1}^{M} s_{n,m} \ln(\hat{s}_{n,m}) + (1 - s_{n,m}) \ln(1 - \hat{s}_{n,m}) \tag{4.21}$$

where N is the number of frames in the training dataset; M is the number of symbols per frame; $s_{n,m}$ is the ground-truth value ($S0$ or $S1$) of the m-th symbol in the n-th frame, while $\hat{s}_{n,m}$ is the corresponding predicted probability of $s_{n,m} = S1$. The gradient of this loss function w.r.t internal parameters can be obtained by applying the backpropagation through time (BPTT) algorithm [173].

The LSTM-based demodulator is trained on the simulated dataset for a maximum of 20 epochs. To prevent overfitting to the training dataset, 20% of the training samples are

reserved as a validation dataset for early stopping. A test dataset, collected from the 'THz Torch' wireless link, is used to evaluate the demodulation performance on the real system. The gradient-based ADAM optimizer [174] is employed with a learning rate of 3×10^{-4} and 100 samples per batch (with 100 batches per epoch in our case). Figure 4.7 shows the training progress for the LSTM-based demodulator. After each epoch, the cross-entropy loss in equation (4.21) and the BER are evaluated on all three datasets. For evaluating the BER, the demodulated symbol s_i can be simply decided by:

$$s_i = \begin{cases} S0, & \text{if } \hat{s}_i \leq 0.5 \\ S1, & \text{if } \hat{s}_i > 0.5 \end{cases} \tag{4.22}$$

As illustrated in Figure 4.7, performances on these datasets are consistent during the whole training procedure, showing no sign of overfitting. Furthermore, the training can be early stopped after the 15-th epoch since the BER evaluated on the validation set stops improving. After deploying the trained LSTM-based Demodulator to the real 'THz Torch' wireless link, its internal parameters for the LSTM and MLP can be further fine-tuned using training samples collected from the real system, which is known as transfer learning [172].

To understand the underlying decision process, operated by the trained LSTM-based demodulator, Figure 4.8 shows its decision boundaries for six arbitrarily sampled received symbols and makes a comparison with those from the matched filter. Each decision boundary for the matched filter is obtained by equalling the probabilities of the received signal in equation (4.17) under two Gaussian distributions in equation (4.16), while the LSTM decision boundary is estimated numerically by computing the $\hat{s}_i = p(s_i = S1|v_{s_i}^{s_{1:(i-1)}}[t])$ over a signal space grid. Being different from the matched filter boundary, which is always the mid-perpendicular of the line segment through $S0$ to $S1$, the local LSTM boundary resembles a straight line whose position and rotation vary from symbol to symbol. An-

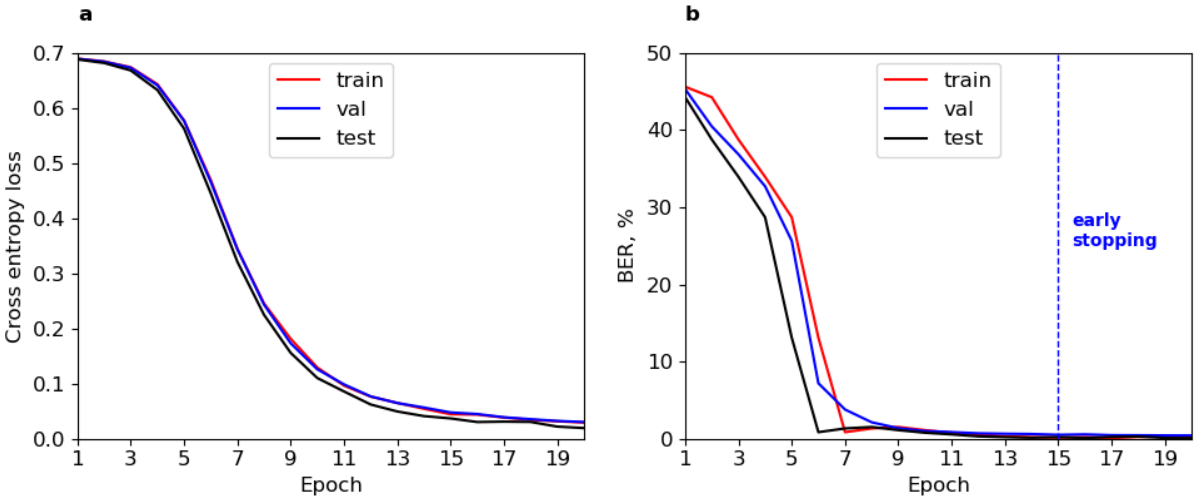


Figure 4.7: Training curve of a LSTM-based demodulator (**a**) Evaluated cross-entropy loss on training, validation and test datasets after each epoch. (**b**) Evaluated BER on training, validation and test datasets after each epoch.

other noticeable pattern is that the LSTM boundary tends to be parallel to the first basis ϕ_{i0} given in equation (4.15). It can be seen that the matched filter is always optimal with pure WGN. However, in practice, the channel noise does not closely follow this assumption, and it will be demonstrated in the next section that the LSTM-based demodulator gives better performance.

The LSTM-based Cognitive Demodulator overcomes the shortcomings of our template-matching based demodulators in several respects:

- The LSTM is independent of the emitter and sensor parameter values. The rationalé is that although these channel parameter values may vary between systems, the received signals have similar patterns for a particular symbol sequence. The LSTM will extract these meaningful patterns instead of being distracted by variations in channel parameter values. Therefore, demodulation can be less sensitive to channel estimation error.

- Noise is taken into account by adding tailored artificial noise to the training dataset. This improves the demodulator's resilience to noise.

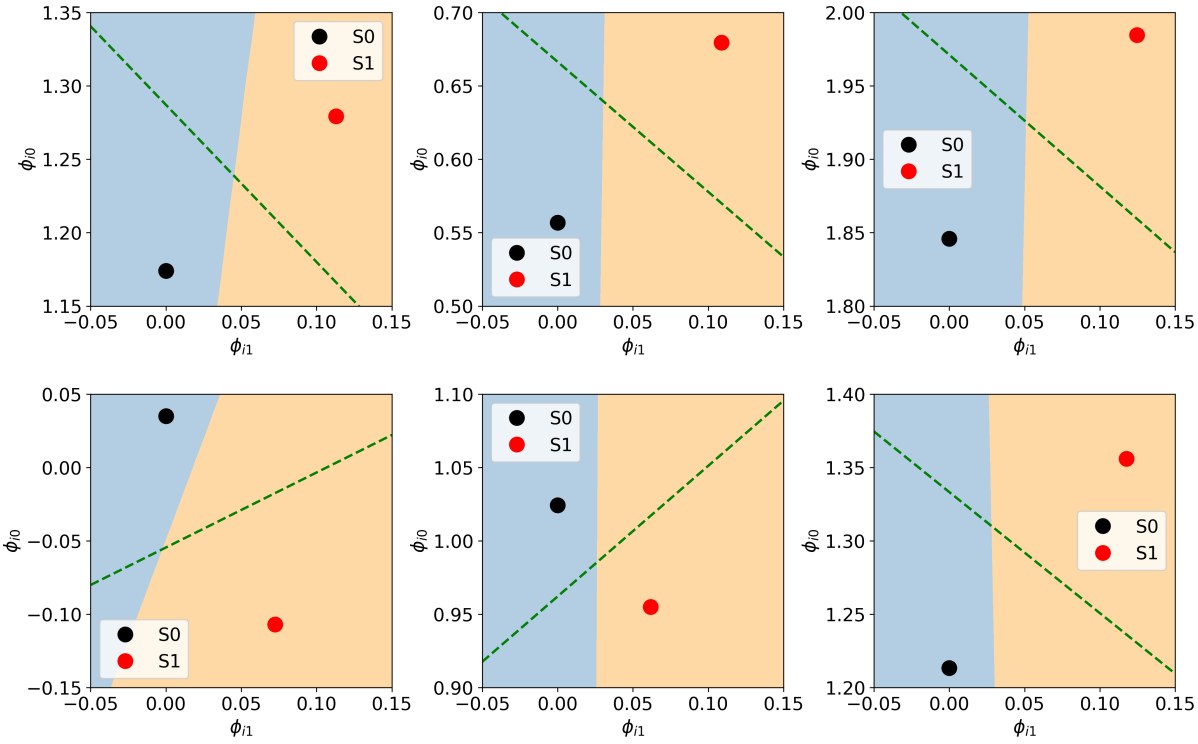


Figure 4.8: Signal space decision boundaries for the LSTM-based demodulator (between the two colours) and the matched filter (green dashed line, mid-perpendicular of the line segment through $S0$ and $S1$).

- Demodulation of the current symbol s_i is not directly dependent on the correct results of previous symbols $s_{1:(i-1)}$. Instead, the whole received signal until the i-th symbol $v[0 : iT_S]$ is used, eliminating the possibility for a chain of errors.
- The computational cost is significantly reduced to a simple forward pass of the LSTM.

Although artificial intelligence is exploited, the LSTM-based demodulator remains rooted in the thermodynamics-based model. When making the final decision, the demodulator still takes the channel parameters into consideration via the MLP. Furthermore, training is based on simulated data from the thermodynamics-based model. In other words, the cognitive demodulation process is distilled into the lightweight LSTM.

4.3 Performance

4.3.1 Enhanced performance demonstration

Figure 4.9 shows the operation of demodulation with three different algorithms introduced in this chapter. All the figures use the same test frame collected from a single-channel 2 m link transmitting at 125 bps and composed of a four-symbol preamble followed by 50 pseudo-randomly generated symbols. The received noisy signal $v[t]$ is showed in blue. For the naive template matching and the matched filter algorithms in Figure 4.9, two expected noiseless signals of each symbol s_i ($v_{S0}^{s_{1:(i-1)}}$ and $v_{S1}^{s_{1:(i-1)}}$) are showed in black and red, respectively. In each figure, the correctness of the demodulated symbols is indicated by a sequence of green circles and red crosses. To highlight the contribution from the channel estimator, we also compare two configurations for each algorithm. The configuration with estimated thermal emitter parameters is labelled with a prefix 'E' and that without the prefix employs initial emitter parameters.

An algorithm-level comparison reveals that the matched filter consistently outperforms the naive template matching. It is achieved by employing the signal space concept to eliminate the noise component that is orthogonal to the two-dimensional signal space. In contrast, with the LSTM-based demodulator, there is no need to dynamically predict the expected noiseless signals. In addition, the LSTM-based demodulator has an ideal performance, resulting in error-free transmission for this particular test frame. Moreover, both template-matching based algorithms (NTM and MF) show a chain of symbol errors. As explained in Section 4.2.5, this pattern is caused by the dependency of the currently expected signals $v_{S0}^{s_{1:(i-1)}}$ and $v_{S1}^{s_{1:(i-1)}}$ on previously demodulated symbols $s_{1:(i-1)}$. Moreover, the emitter estimation can significantly enhance both template-matching based algorithms by providing more accurate 'templates'. In contrast, with the LSTM-based demodulator, good resilience is shown to parameter mismatch in this test scenario since

the LSTM network is trained to extract common signal patterns shared between different channel parameters. BER measurements will show that combining the estimated emitter parameters through the MLP layers can further enhance the performance of the LSTM-based demodulator.

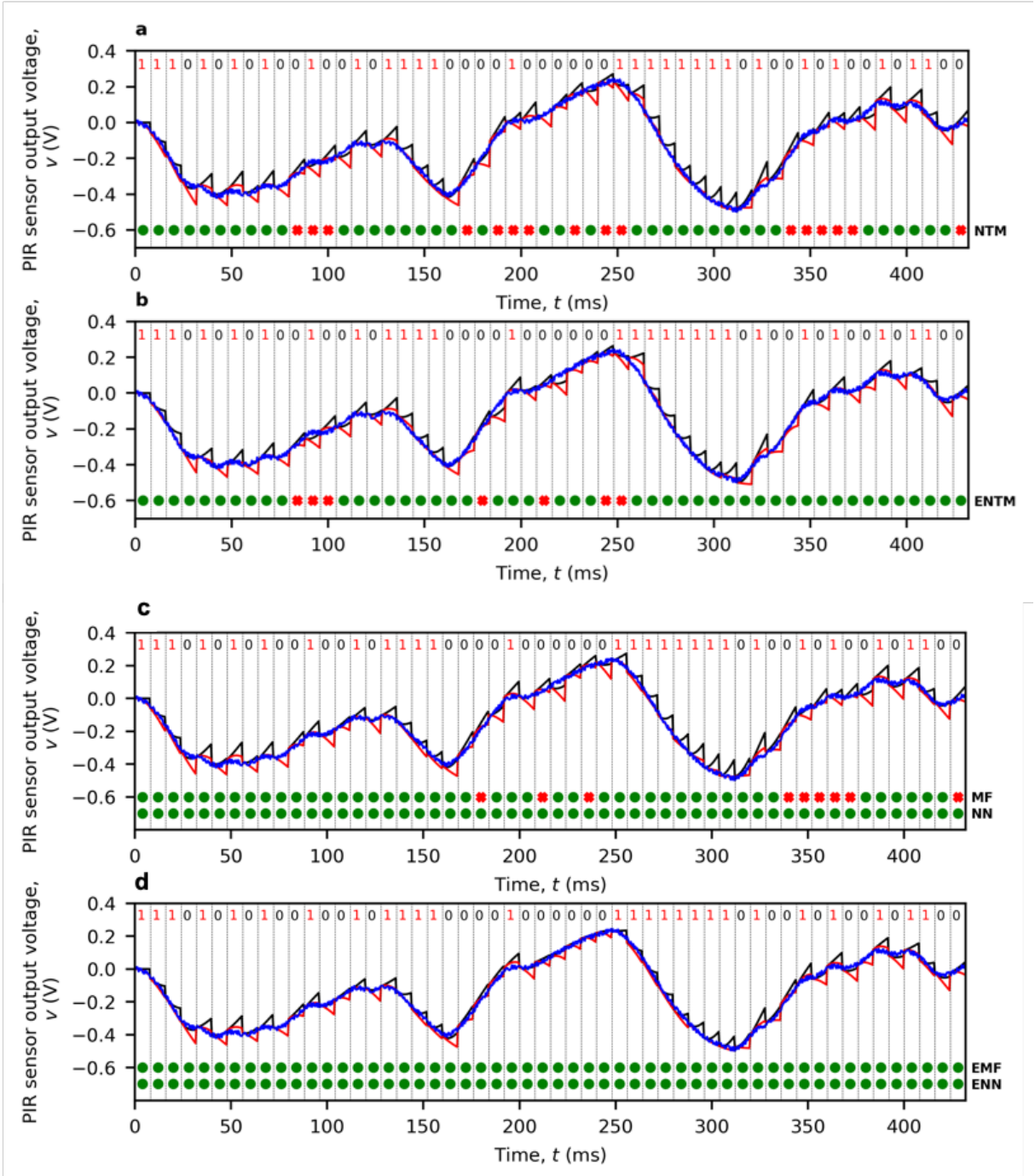


Figure 4.9: Operation of demodulation demonstrated for the 2 m single-channel 'THz Torch' wireless link field trial. (**a**) NTM with initial thermal emitter parameters (16 symbol errors). (**b**) NTM with estimated thermal emitter parameters (7 symbol errors). (**c**) MF with initial thermal emitter parameters (9 symbols errors). (**d**) MF with estimated thermal emitter parameters (error free). The LSTM-based demodulator with and without estimated thermal emitter parameters (error-free) is also shown in (c)(d). Here, the LSTM-based demodulator is only trained on the simulated dataset without any fine-tuning using data from the real system.

4.3.2 Bit Error Rate

Figure 4.10 and 4.11 show the measured raw bit error rate performances (without any additional error correction coding) for the single-channel 2 m wireless links in both laboratory and non-laboratory environments. These measurements are performed by sending 2,000 frames across the wireless link. Each frame has a fixed four-symbol preamble for timing synchronization and 50 pseudo-randomly generated symbols. The fractionally spaced sampler is set to 20 times the bit rate. The discrete PIR sensor output voltage signal for each frame is saved and then demodulated offline using our six algorithms for comparison: (E)NTM, (E)MF, (E)NN. Again, with the LSTM-based demodulator, (E)NN are only trained on the simulated dataset, without any fine-tuning using data from the real system.

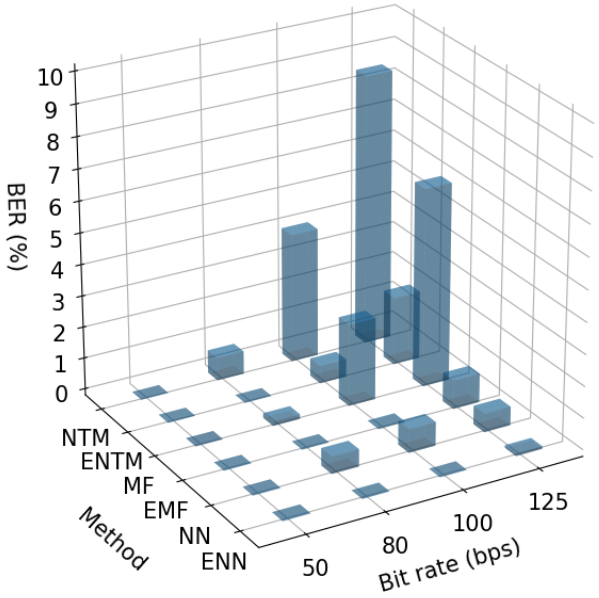


Figure 4.10: Measured BER performance for the single-channel 2 m link in a laboratory environment with optical bench and precision alignment rails, as shown in Figure 3.1b.

As a baseline, the NTM algorithm gives a BER of less than 9% at 125 bps. The ENTM algorithm maintains the BER to below 5%, which is still impractical for most applica-

tions. When operating at low bit rates, the EMF algorithm, enhanced by the thermal emitter estimation, shows a significantly improved performance. Introducing the LSTM provides a step-change reduction in the BER, down to 1%, even with mismatched emitter parameter values. Finally, the ENN algorithm that combines all enhancements techniques consistently outperforms the other algorithms at higher bit rates, with measured BER less than 0.16% at 125 bps. Compared to the NTM baseline, its BER is improved by a factor of 108 within the laboratory and 59 in the non-laboratory field trials. An additional non-laboratory experiment is performed over an extended 2.5 m link, which demonstrated error-free data transmission at 50 bps. Moreover, with a 1.5 m link, the ENN algorithm demonstrated a measured BER below 0.1% at 125 bps.

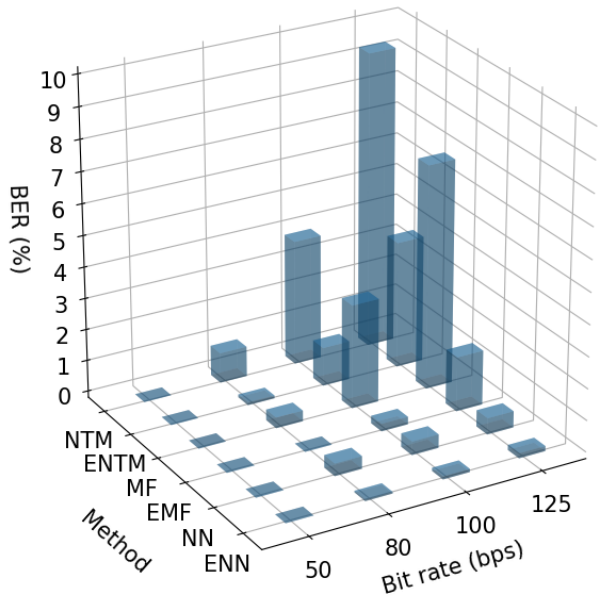


Figure 4.11: Measured BER performance for the single-channel 2 m link in a non-laboratory environment (office corridor) with laser alignment, as shown in Figure 3.2.

From the measurement results, we can conclude that:

- With the non-laboratory demonstrators, the performance is slightly degraded due to sub-optimal spatial alignment and possibly more environmental noise.

- From the algorithm-level comparison, the matched filter consistently outperforms naive template matching, while LSTM-based demodulation achieves the best performance in all test scenarios.

- Updated parameters from the channel estimator can enhance all three algorithms. The two template-matching based algorithms (NTM and MF) heavily rely on accurate parameters, while LSTM-based demodulation is more resilient to parameter mismatch.

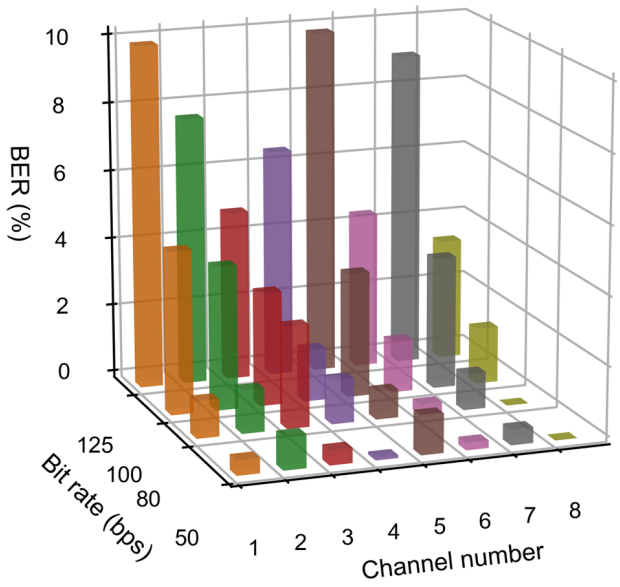


Figure 4.12: Measured NTM BER performance for the multi-channel 0.5 m link in a laboratory environment with optical bench and precision alignment rails, as shown in Figure 3.1b.

The NTM algorithm is also tested on a multi-channel wireless link over a range of 0.5 m. The eight non-overlapping sub-bands, corresponding to eight channels, have been shown in Figure 3.1a. With all advances introduces in this chapter, the reported BER performance in Figure 4.12 can be further improved. By dividing the thermal infrared band into sub-bands, 'THz Torch' wireless link has the potential to support more complex communication schemes, such as frequency-division multiplexing (FDM) and frequency-hopping spread-spectrum (FHSS).

From a batch test of 100 frames on an Intel Xeon 2.30 GHz CPU, with (E)NTM and (E)MF the time taken for demodulation is approximately 2.54 seconds per frame; while with (E)NN the time taken is only 0.256 milliseconds per frame. Therefore, introducing the LSTM speeds-up demodulation by a factor of 9,922, allowing for real-time demodulation while easing computational hardware requirements.

An implementation and performance summary comparison of the reported 'THz Torch' wireless links is given in Table 4.1. It can be seen that this work not only allows for truly asynchronous operation and low BER, but when sending arbitrary data, gives a five-fold increase in the operational figure of merit when compared to using an indirect modulation (mechanical chopper) and 10,000 fold increase when compared to using direct modulation (electronic modulation).

4.4 Summary

This chapter details the design of the cognitive 'THz Torch' receiver, rooted in the thermodynamic system modelling in the previous chapter. The receiver architecture, including the timing synchronizer, the channel estimator and the demodulator, is first introduced. Then we adapt the hypothesis testing framework and combine it with the developed system model, giving two template-matching-based algorithms (NTM and MF) for synchronization and demodulation purposes. Two algorithmic advances are further considered. The change-point detection method is proposed to refine the timing synchronization under model parameter mismatch while the LSTM-based demodulator is presented to mitigate the WGN assumption and the chain of error problem seen in template-matching based algorithms. The LSTM also speeds-up demodulation significantly, enabling real-time demodulation while easing computational hardware requirements. Our cognitive receiver design is verified using the measured BER from two experimental setups.

Table 4.1: Implementation and performance summary comparisons of reported 'THz Torch' wireless links

	Sep. 2011[11]	Dec. 2011[12]	Apr. 2013[16]	Jun. 2014[17]	May 2016[15]	This Work
Source Type	5×Eiko-8666 4.7 × 3.7 mm^2	5×Eiko-8666 4.7 × 3.7 mm^2	5×Eiko-8666 4.7 × 3.7 mm^2	5×Eiko-8666 4.7 × 3.7 mm^2	5×Eiko-8666 4.7 × 3.7 mm^2	INTX 17-0900 1.7 × 1.7 mm^2
Emitter DC Power (mW)	146	4×146 = 584	146	4×994 = 3,976	994	898 and 8×898 = 7,184
Number of Channels	1	4	1	4	1	1 and 8
3 dB Bandwidth (THz)	25	∼4×15 = 60	25	∼4×15 = 60	25	16 and ∼8×2.5
Modulation Mechanism	Electronic	Chopper	Chopper	Chopper	Chopper	Electronic
Transmitted Data	Clock	Clock	Clock	Arbitrary	Clock	Arbitrary
Operation	Record and post-process	Record and post-process	Record and post-process	Record and post-process	Record and post-process	Fully asynchronous
Tx-Rx Lens Pair	None	None	None	None	KBr ∅1.5 cm	ZnSe ∅2.5 cm
min ⇒ max Range (cm)	0.5 ⇒ 2.5	1.0	1.0	3 ⇒ 4	12 ⇒ 15	100 ⇒ 200 and 50
PIR Sensor	Voltage mode IRA-E710ST1	Voltage mode IRA-E710ST1	Current mode LME-553	Current mode LME-553	Current mode LME-553	Current mode LME-335
Total NRZ Bit Rate (bps)	10.2 ⇒ 1	4×20.6 = 82	760	4×640 = 2,560	2,000	125 and 8×125 = 1,000
Figure of Merit (cm × bps)	5.1	82	760	10,240	30,000	25,000 and 50,000
Bit Error Rate (%)	0 qualitative	0 qualitative	0 qualitative	0.11 ⇒ 15 quantitative	0.0018 ⇒ 18 quantitative	see Figure quantitative

Chapter 5

Conclusion and future work

5.1 Summary of thesis achievements

This thesis reports a 'THz Torch' wireless communications link characterized by its fully thermal-based physical layer. At the transmitter end, it exploits a thermally generated broadband noise carrier with direct OOK modulation. The receiver end mainly consists of a PIR sensor for power detection and a digital receiver for signal processing.

A thermodynamics-based channel model is developed for the 'THz Torch' wireless link. The temperature and radiated spectrum of the thermal emitter, under fast OOK modulation, is first studied. Outcomes include a piecewise polynomial for approximating the time-variant emitter temperature and the temperature-dependent power spectral density of the generated noise carrier. Free space propagation is then investigated, demonstrating the resilience of our 'THz Torch' channel to atmospheric attenuation. The modulated carrier power is detected by the PIR sensor, whose output voltage is modelled by combining thermodynamics, pyroelectric and circuit equations. The noise mechanism of the 'THz Torch' channel is analysed to support further noise reduction.

Based on the developed channel model, a cognitive 'THz Torch' receiver is reported. It consists of three core blocks: a channel estimator, a timing synchronizer, and a demodulator. The channel estimator, including a sensor and emitter estimators, exploits optimization-based approaches to updates the channel model parameters from predefined training signals. The second-order evolution strategy developed for emitter estimation can be scaled-up to estimate high-dimensional complex systems. Following the classic hypothesis test framework, two template-matching based algorithms (NTM and MF) are proposed for timing synchronization and demodulation. More advanced algorithms are introduced to further enhance the receiver's performance. Change-point detection can achieve ideal timing synchronization under parameter mismatch, while an LSTM-based demodulator outperforms template-matching based algorithms in both accuracy and speed.

The hardware and software for the proposed 'THz Torch' wireless link are implemented, and two test benches are set up to experimentally verify its performance. It is demonstrated that the wireless link, with direct electronic modulation, can support a data transfer up to 125 bps, over a single-channel 2 m link, with a BER below 0.16 %. Compared with previously reported 'THz Torch' wireless links [12–14, 16, 175], step-change improvements have been achieved.

5.2 Future work

Further work will focus on improving the signal-to-noise ratio (SNR) of the 'THz Torch' wireless link to advance the operational figure of merit and support M-ary amplitude shift keying signaling. To achieve this target, two potential directions are proposed as follows.

An adaptive low-pass baseband filter can be introduced between the PIR sensor and the ADC to reduce out-of-band noise and aliasing. The cut-off frequency of this filter should

be adapted to the bandwidth of the expected baseband signal. The fractional energy containment bandwidth f_B of the baseband signal is defined as:

$$\int_{-f_B}^{f_B} v_s^2(f)\ df = \mathcal{F} \int_{-\infty}^{\infty} v_s^2(f)\ df \tag{5.1}$$

where $v_s^2(f)$ is the power spectral density (PSD) of the expected noiseless signal $v_s(t)$ when transmitting at the given symbol rate; $\mathcal{F} \in (0, 1]$ is the fraction of energy contained in the band $[-f_B, f_B]$. Choosing a $\mathcal{F}$ close to 1.0, the f_B can be solved numerically, and the cut-off frequency of the filter should be above the f_B by a margin. One difficulty is that $v_s(t)$ is a baseband random process whose randomness comes from the random transmitted symbols. For a conventional linear modulation scheme, its PSD $v_s^2(f)$ can be derived based on some sufficient statistics of the transmitted symbols [166] and the symbol rate. As shown in Figure 5.1, $v_s^2(f)$ can be estimated empirically for our 'THz Torch' wireless link.

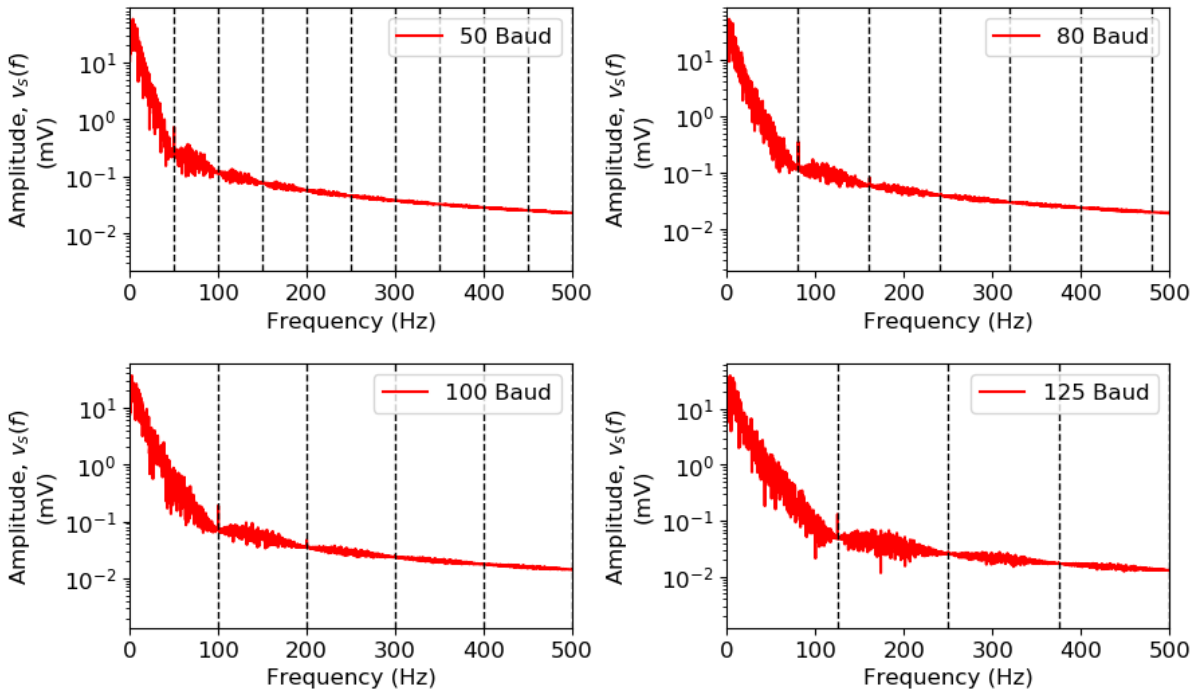


Figure 5.1: Empirical $v_s(f)$ of the expected noiseless received signal under different symbol rates.

For each symbol rate, the empirical amplitude spectral density $v_s(f)$ (square root of the PSD) is obtained by averaging the discrete Fourier transform of random data frames. A rule a thumb is to choose $f_B = 3 \times$ symbol rate so that at least 99.9 % signal power falls into the filter passband. Another requirement is that the low-pass filter should have a linear phase response to maintain the shape of the signal. A Bessel prototype can be employed to this end. Other methods for reducing baseband environmental noise have been suggested in Section 3.3.

The signal power can also be improved, which will increase both the channel range and symbol rate. For example, the miniature thermal emitter can be replaced by the more powerful Globar [176] (albeit with a longer thermal time constant). By scaling-up the effective area of the PIR sensor, the received signal power is supposed to increase. Since the signal power with our system varies from symbol-to-symbol and depends on the entire symbol sequence, it is worth investigating an optimized coding scheme for this thermal-based wireless link.

The cognitive receiver, consisting of an intelligent channel estimator, synchronizer, and demodulator, has been applied to the thermal-based emitter and sensor front-end hardware. This concept can potentially be adapted to any communications and sensor technologies. For example, the channel estimator based on gradient-free optimization can be scaled up to identify complex systems with non-analytical input-to-output functions. In addition, the idea of demodulating symbols from non-stationary signals can be extended to bolometers and even microbolometer arrays employed in terahertz/infrared cameras. These thermal sensors operating at room temperature usually suffer from low sampling rates (around 30 samples per second) limited by their thermal time constants. This weakness can be overcome by adapting our technique. Moreover, our engineered thermal source can be replaced by bodies that naturally emitted thermal radiation; monitoring for specific thermal transients can open-up new low-cost applications in non-destructive testing and remote sensing. For example, analysing temporal fluctuations in localized

body temperature could provide useful information in medical diagnostics. Within the aerospace sector, sensor arrays could be deployed for monitoring anomalous behaviour at a distance. An extreme example is with broadband (sub-)millimeter-wave astronomy, traditionally employing microbolometer arrays, where neural networks can be trained to detect the very early onset of astronomical events that can be modelled. Furthermore, underwater wireless communication can benefit from this work, since both share common difficulties, such as time variations of the channel and small available bandwidth.

5.3 Publications from this work

- Hang Ren and Stepan Lucyszyn. "Thermodynamics-based Cognitive Demodulation for 'THz Torch' Wireless Communications Links". In: *Scientific Reports* 10.1 (Apr. 2020), p. 6259. ISSN: 2045-2322. DOI: 10.1038/s41598-020-62234-1. URL: https://doi.org/10.1038/s41598-020-62234-1

- Hang Ren, Sang-Hee Shin, and Stepan Lucyszyn. "Enhanced cognitive demodulation with artificial intelligence". In: *Scientific Reports* 10.1 (Nov. 2020), p. 20298. ISSN: 2045-2322. DOI: 10.1038/s41598-020-77262-0. URL: https://doi.org/10.1038/s41598-020-77262-0

References

[1] Bogdan M Wilamowski and J David Irwin. *Industrial communication systems*. CRC Press, 2016.

[2] Joseph Carr. *Microwave and Wireless Communications Technology*. Elsevier, 1997.

[3] Theodore S Rappaport et al. "Millimeter wave mobile communications for 5G cellular: It Will Work!" In: *IEEE Access* 1 (2013), pp. 335–349.

[4] S Koenig et al. "Wireless sub-THz communication system with high data rate". In: *Nature photonics* 7.12 (2013), p. 977.

[5] Ian F Akyildiz, Josep Miquel Jornet, and Chong Han. "Terahertz band: Next frontier for wireless communications". In: *Physical Communication* 12 (2014), pp. 16–32.

[6] Aleksandar Jovicic, Junyi Li, and Tom Richardson. "Visible light communication: opportunities, challenges and the path to market". In: *IEEE Communications Magazine* 51.12 (2013), pp. 26–32.

[7] Patrick J Megowan, David W Suvak, and Charles D Knutson. "IrDA infrared communications: An overview". In: *Counterpoint Systems Foundry, INC* 96 (1996).

[8] Helmut Budzier and Gerald Gerlach. *Thermal infrared sensors: theory, optimisation and practice*. John Wiley & Sons, 2011.

[9] Gilbert Gaussorgues and Seweryn Chomet. *Infrared thermography*. Vol. 5. Springer Science & Business Media, 2012.

[10] Benjamin S Williams. "Terahertz quantum-cascade lasers". In: *Nature photonics* 1.9 (2007), p. 517.

[11] Stepan Lucyszyn, Hanchao Lu, and Fangjing Hu. "Ultra-low cost THz short-range wireless link". In: *IEEE MTT-S International Microwave Workshop Series on Millimeter Wave Integration Technologies*. IEEE. 2011, pp. 49–52.

[12] Fangjing Hu and Stepan Lucyszyn. "Ultra-low cost ubiquitous THz security systems". In: *Asia-Pacific Microwave Conference 2011*. IEEE. 2011, pp. 60–62.

[13] Fangjing Hu and Stepan Lucyszyn. "Modelling miniature incandescent light bulbs for thermal infrared 'THz Torch' applications". In: *Journal of Infrared, Millimeter, and Terahertz Waves* 36.4 (2015), pp. 350–367.

[14] Fangjing Hu et al. "Systems analysis for thermal infrared 'THz Torch' applications". In: *Journal of Infrared, Millimeter, and Terahertz Waves* 36.5 (2015), pp. 474–495.

[15] Fangjing Hu and Stepan Lucyszyn. "Advances in front-end enabling technologies for thermal infrared 'THz Torch' wireless communications". In: *Journal of Infrared, Millimeter, and Terahertz Waves* 37.9 (2016), pp. 881–893.

[16] Fangjing Hu and Stepan Lucyszyn. "Improved 'THz Torch' technology for short-range wireless data transfer". In: *2013 IEEE International Wireless Symposium*. IEEE. 2013, pp. 1–4.

[17] Xiaoxin Liang et al. "Secure thermal infrared communications using engineered blackbody radiation". In: *Scientific Reports* 4 (2014), p. 5245.

[18] Hang Ren and Stepan Lucyszyn. "Thermodynamics-based Cognitive Demodulation for 'THz Torch' Wireless Communications Links". In: *Scientific Reports* 10.1 (Apr. 2020), p. 6259. ISSN: 2045-2322. DOI: 10.1038/s41598-020-62234-1. URL: https://doi.org/10.1038/s41598-020-62234-1.

[19] SS Dhillon et al. “The 2017 terahertz science and technology roadmap”. In: *Journal of Physics D: Applied Physics* 50.4 (2017), p. 043001.

[20] *Workshop on Terahertz Communications — IEEE International Conference on Communications - IEEE ICC 2020*. https://icc2020.ieee-icc.org/workshop/ws-12-workshop-terahertz-communications.

[21] *SURA — The Science of Collaborative Research*. http://www6.sura.org/.

[22] RA Lewis. “A review of terahertz detectors”. In: *Journal of Physics D: Applied Physics* 52.43 (2019), p. 433001.

[23] Roger A Lewis. “A review of terahertz sources”. In: *Journal of Physics D: Applied Physics* 47.37 (2014), p. 374001.

[24] Kaushik Sengupta, Tadao Nagatsuma, and Daniel M Mittleman. “Terahertz integrated electronic and hybrid electronic–photonic systems”. In: *Nature Electronics* 1.12 (2018), pp. 622–635.

[25] Vesna Radisic et al. “Demonstration of a 311-GHz fundamental oscillator using InP HBT technology”. In: *IEEE transactions on microwave theory and techniques* 55.11 (2007), pp. 2329–2335.

[26] Munkyo Seo et al. “InP HBT IC technology for terahertz frequencies: Fundamental oscillators up to 0.57 THz”. In: *IEEE Journal of Solid-State Circuits* 46.10 (2011), pp. 2203–2214.

[27] J Yun et al. “645-GHz InP heterojunction bipolar transistor harmonic oscillator”. In: *Electronics Letters* 53.22 (2017), pp. 1475–1477.

[28] Tsuyoshi Takahashi et al. “Maximum frequency of oscillation of 1.3 THz obtained by using an extended drain-side recess structure in 75-nm-gate InAlAs/InGaAs high-electron-mobility transistors”. In: *Applied Physics Express* 10.2 (2017), p. 024102.

[29] Imran Mehdi et al. “THz diode technology: status, prospects, and applications”. In: *Proceedings of the IEEE* 105.6 (2017), pp. 990–1007.

[30] ER Brown et al. “Oscillations up to 712 GHz in InAs/AlSb resonant-tunneling diodes”. In: *Applied Physics Letters* 58.20 (1991), pp. 2291–2293.

[31] Hidetoshi Kanaya et al. “Fundamental oscillation up to 1.31 THz in resonant tunneling diodes with thin well and barriers”. In: *Applied Physics Express* 5.12 (2012), p. 124101.

[32] Takeru Maekawa et al. “Oscillation up to 1.92 THz in resonant tunneling diode by reduced conduction loss”. In: *Applied Physics Express* 9.2 (2016), p. 024101.

[33] H Eisele. “InP Gunn devices for 400–425 GHz”. In: *Electronics letters* 42.6 (2006), pp. 358–359.

[34] H Eisele. “480 GHz oscillator with an InP Gunn device”. In: *Electronics letters* 46.6 (2010), pp. 422–423.

[35] Eunyoung Seok et al. “A 410GHz CMOS push-push oscillator with an on-chip patch antenna”. In: *2008 IEEE International Solid-State Circuits Conference-Digest of Technical Papers*. IEEE. 2008, pp. 472–629.

[36] H Rücker, B Heinemann, and A Fox. “Half-terahertz sige bicmos technology”. In: *2012 IEEE 12th topical meeting on silicon monolithic integrated circuits in RF systems*. IEEE. 2012, pp. 133–136.

[37] Ullrich R Pfeiffer et al. “14.5 A 0.53 THz reconfigurable source array with up to 1mW radiated power for terahertz imaging applications in 0.13 μm SiGe BiCMOS”. In: *2014 IEEE International Solid-State Circuits Conference Digest of Technical Papers (ISSCC)*. IEEE. 2014, pp. 256–257.

[38] Antti Räisänen and Mikko Sironen. “Capability of schottky-diode multipliers as local oscillators at 1 THz”. In: *Microwave and Optical Technology Letters* 4.1 (1991), pp. 29–33.

[39] Alain Maestrini et al. “A frequency-multiplied source with more than 1 mW of power across the 840–900-GHz band”. In: *IEEE transactions on microwave theory and techniques* 58.7 (2010), pp. 1925–1932.

[40] José V Siles and Jesús Grajal. “Physics-based design and optimization of Schottky diode frequency multipliers for terahertz applications”. In: *IEEE Transactions on Microwave Theory and Techniques* 58.7 (2010), pp. 1933–1942.

[41] Zeshan Ahmad, Mark Lee, et al. “20.5 1.4 THz,- 13dBm-EIRP frequency multiplier chain using symmetric-and asymmetric-CV varactors in 65nm CMOS”. In: *2016 IEEE International Solid-State Circuits Conference (ISSCC)*. IEEE. 2016, pp. 350–351.

[42] Tadao Nagatsuma. “Terahertz technologies: present and future”. In: *IEICE Electronics Express* 8.14 (2011), pp. 1127–1142.

[43] P Uhd Jepsen, Rune Hylsberg Jacobsen, and SR Keiding. “Generation and detection of terahertz pulses from biased semiconductor antennas”. In: *JOSA B* 13.11 (1996), pp. 2424–2436.

[44] Masahiko Tani et al. “Emission characteristics of photoconductive antennas based on low-temperature-grown GaAs and semi-insulating GaAs”. In: *Applied optics* 36.30 (1997), pp. 7853–7859.

[45] Nathan M Burford and Magda O El-Shenawee. “Review of terahertz photoconductive antenna technology”. In: *Optical Engineering* 56.1 (2017), p. 010901.

[46] A Rice et al. “Terahertz optical rectification from 110 zinc-blende crystals”. In: *Applied physics letters* 64.11 (1994), pp. 1324–1326.

[47] PY Han et al. “Use of the organic crystal DAST for terahertz beam applications”. In: *Optics Letters* 25.9 (2000), pp. 675–677.

[48] Reza Safian, Galia Ghazi, and Nafiseh Mohammadian. "Review of photomixing continuous-wave terahertz systems and current application trends in terahertz domain". In: *Optical Engineering* 58.11 (2019), p. 110901.

[49] ER Brown et al. "Photomixing up to 3.8 THz in low-temperature-grown GaAs". In: *Applied Physics Letters* 66.3 (1995), pp. 285–287.

[50] Cyril C Renaud et al. "Antenna integrated THz uni-traveling carrier photodiodes". In: *IEEE Journal of Selected Topics in Quantum Electronics* 24.2 (2017), pp. 1–11.

[51] Yujie J Ding. "High-power tunable terahertz sources based on parametric processes and applications". In: *IEEE Journal of selected topics in quantum electronics* 13.3 (2007), pp. 705–720.

[52] Kodo Kawase, Jun-ichi Shikata, and Hiromasa Ito. "Terahertz wave parametric source". In: *Journal of Physics D: Applied Physics* 35.3 (2002), R1.

[53] Yuzo Sasaki et al. "Terahertz-wave surface-emitted difference frequency generation in slant-stripe-type periodically poled LiNbO3 crystal". In: *Applied Physics Letters* 81.18 (2002), pp. 3323–3325.

[54] Wei Shi et al. "Single-frequency terahertz source pumped by Q-switched fiber lasers based on difference-frequency generation in GaSe crystal". In: *Optics letters* 32.8 (2007), pp. 949–951.

[55] G Dodel. "On the history of far-infrared (FIR) gas lasers: Thirty-five years of research and application". In: *Infrared physics & technology* 40.3 (1999), pp. 127–139.

[56] Jerome Faist et al. "Quantum cascade laser". In: *Science* 264.5158 (1994), pp. 553–556.

[57] Yu Yao, Anthony J Hoffman, and Claire F Gmachl. "Mid-infrared quantum cascade lasers". In: *Nature Photonics* 6.7 (2012), pp. 432–439.

[58] Benjamin S Williams. "Terahertz quantum cascade lasers". In: *Asia Optical Fiber Communication and Optoelectronic Exposition and Conference*. Optical Society of America. 2008, SuG3.

[59] Benjamin S Williams et al. "Operation of terahertz quantum-cascade lasers at 164 K in pulsed mode and at 117 K in continuous-wave mode". In: *Optics express* 13.9 (2005), pp. 3331–3339.

[60] Sushil Kumar et al. "Continuous-wave operation of terahertz quantum-cascade lasers above liquid-nitrogen temperature". In: *Applied physics letters* 84.14 (2004), pp. 2494–2496.

[61] Dominic Bachmann et al. "Short pulse generation and mode control of broadband terahertz quantum cascade lasers". In: *Optica* 3.10 (2016), pp. 1087–1094.

[62] Mikhail A Belkin et al. "Room temperature terahertz quantum cascade laser source based on intracavity difference-frequency generation". In: *Applied Physics Letters* 92.20 (2008), p. 201101.

[63] Mikhail A Belkin and Federico Capasso. "New frontiers in quantum cascade lasers: high performance room temperature terahertz sources". In: *Physica Scripta* 90.11 (2015), p. 118002.

[64] VM Zolotarev et al. "Spectral emissivity of a Globar lamp in the 2-50-μm region". In: *Journal of Optical Technology* 74.6 (2007), pp. 378–384.

[65] RA Friedel and AG Sharkey Jr. "Comparison of Glower and Globar Sources for Infra-Red Spectrometry". In: *Review of Scientific Instruments* 18.12 (1947), pp. 928–928.

[66] K Charrada, Georges Zissis, and M Aubes. "Two-temperature, two-dimensional fluid modelling of mercury plasma in high-pressure lamps". In: *Journal of Physics D: Applied Physics* 29.9 (1996), p. 2432.

[67] Hao Xin et al. “THz thermal radiation enhancement using an electromagnetic crystal”. In: *IEEE transactions on antennas and propagation* 56.9 (2008), pp. 2970–2980.

[68] W Becker, R Fettig, and W Ruppel. “Optical and electrical properties of black gold layers in the far infrared”. In: *Infrared Physics & Technology* 40.6 (1999), pp. 431–445.

[69] Sinan Li et al. “A survey, classification, and critical review of light-emitting diode drivers”. In: *IEEE Transactions on Power Electronics* 31.2 (2015), pp. 1503–1516.

[70] Edwin J Koerperick et al. “Cascaded superlattice InAs/GaSb light-emitting diodes for operation in the long-wave infrared”. In: *IEEE Journal of Quantum Electronics* 47.1 (2010), pp. 50–54.

[71] Olaleye Ajakaiye et al. “Wafer-scale fabrication of infrared detectors based on tunneling displacement transducers”. In: *Sensors and Actuators A: Physical* 134.2 (2007), pp. 575–581.

[72] ST Liu and Donald Long. “Pyroelectric detectors and materials”. In: *Proceedings of the IEEE* 66.1 (1978), pp. 14–26.

[73] Akram Hossain and Muhammad H Rashid. “Pyroelectric detectors and their applications”. In: *IEEE Transactions on industry applications* 27.5 (1991), pp. 824–829.

[74] PL Richards. “Bolometers for infrared and millimeter waves”. In: *Journal of Applied Physics* 76.1 (1994), pp. 1–24.

[75] Frank Niklaus, Christian Vieider, and Henrik Jakobsen. “MEMS-based uncooled infrared bolometer arrays: a review”. In: *MEMS/MOEMS technologies and applications III*. Vol. 6836. International Society for Optics and Photonics. 2008, p. 68360D.

[76] Saffa B Riffat and Xiaoli Ma. "Thermoelectrics: a review of present and potential applications". In: *Applied thermal engineering* 23.8 (2003), pp. 913–935.

[77] RU Titz et al. "Investigation of GaAs Schottky barrier diodes in the THz range". In: *International journal of infrared and millimeter waves* 11.7 (1990), pp. 809–820.

[78] Jeffrey L Hesler and Thomas W Crowe. "Responsivity and noise measurements of zero-bias Schottky diode detectors". In: *Proc. ISSTT* (2007), pp. 89–92.

[79] Alain Maestrini et al. "Schottky diode-based terahertz frequency multipliers and mixers". In: *Comptes Rendus Physique* 11.7-8 (2010), pp. 480–495.

[80] Yousuke Nishida et al. "Terahertz coherent receiver using a single resonant tunnelling diode". In: *Scientific reports* 9.1 (2019), pp. 1–9.

[81] Michael Feiginov. "Frequency limitations of resonant-tunnelling diodes in sub-thz and thz oscillators and detectors". In: *Journal of Infrared, Millimeter, and Terahertz Waves* 40.4 (2019), pp. 365–394.

[82] Michael I Dyakonov and Michael S Shur. "Plasma wave electronics: novel terahertz devices using two dimensional electron fluid". In: *IEEE Transactions on Electron Devices* 43.10 (1996), pp. 1640–1645.

[83] W Knap et al. "Resonant detection of subterahertz and terahertz radiation by plasma waves in submicron field-effect transistors". In: *Applied physics letters* 81.24 (2002), pp. 4637–4639.

[84] YC Shen et al. "Generation and detection of ultrabroadband terahertz radiation using photoconductive emitters and receivers". In: *Applied Physics Letters* 85.2 (2004), pp. 164–166.

[85] A Takazato et al. "Terahertz wave emission and detection using photoconductive antennas made on low-temperature-grown InGaAs with 1.56 μm pulse excitation". In: *Applied physics letters* 91.1 (2007), p. 011102.

[86] Ajay Nahata, Aniruddha S Weling, and Tony F Heinz. "A wideband coherent terahertz spectroscopy system using optical rectification and electro-optic sampling". In: *Applied physics letters* 69.16 (1996), pp. 2321–2323.

[87] X-C Zhang, Y Jin, and XF Ma. "Coherent measurement of THz optical rectification from electro-optic crystals". In: *Applied physics letters* 61.23 (1992), pp. 2764–2766.

[88] S Verghese et al. "Generation and detection of coherent terahertz waves using two photomixers". In: *Applied Physics Letters* 73.26 (1998), pp. 3824–3826.

[89] Guillaume Ducournau et al. "Ultrawide-bandwidth single-channel 0.4-THz wireless link combining broadband quasi-optic photomixer and coherent detection". In: *IEEE transactions on terahertz science and technology* 4.3 (2014), pp. 328–337.

[90] Marco Rahm, Jiu-Sheng Li, and Willie J Padilla. "THz wave modulators: a brief review on different modulation techniques". In: *Journal of Infrared, Millimeter, and Terahertz Waves* 34.1 (2013), pp. 1–27.

[91] P Mukherjee and B Gupta. "Terahertz (THz) frequency sources and antennas-A brief review". In: *International Journal of Infrared and Millimeter Waves* 29.12 (2008), pp. 1091–1102.

[92] Thomas Kleine-Ostmann and Tadao Nagatsuma. "A review on terahertz communications research". In: *Journal of Infrared, Millimeter, and Terahertz Waves* 32.2 (2011), pp. 143–171.

[93] Peter H Siegel. "Terahertz technology". In: *IEEE Transactions on microwave theory and techniques* 50.3 (2002), pp. 910–928.

[94] Kumud Ranjan Jha and G Singh. "Terahertz planar antennas for future wireless communication: A technical review". In: *infrared physics & Technology* 60 (2013), pp. 71–80.

[95] John Federici and Lothar Moeller. "Review of terahertz and subterahertz wireless communications". In: *Journal of Applied Physics* 107.11 (2010), p. 6.

[96] Lorene A Samoska. "An overview of solid-state integrated circuit amplifiers in the submillimeter-wave and THz regime". In: *IEEE Transactions on Terahertz Science and Technology* 1.1 (2011), pp. 9–24.

[97] Arline M Melo et al. "Cross-shaped terahertz metal mesh filters: Historical review and results". In: *Advances in Optical Technologies* 2012 (2012).

[98] Bradley Ferguson and Xi-Cheng Zhang. "Materials for terahertz science and technology". In: *Nature materials* 1.1 (2002), pp. 26–33.

[99] P Uhd Jepsen, David G Cooke, and Martin Koch. "Terahertz spectroscopy and imaging–Modern techniques and applications". In: *Laser & Photonics Reviews* 5.1 (2011), pp. 124–166.

[100] PCM Planken, CEWM van Rijmenam, and RN Schouten. "Opto-electronic pulsed THz systems". In: *Semiconductor science and technology* 20.7 (2005), S121.

[101] H Park et al. "Terahertz near-field microscope". In: *2006 Joint 31st International Conference on Infrared Millimeter Waves and 14th International Conference on Teraherz Electronics*. IEEE. 2006, pp. 13–13.

[102] S Wang and XC Zhang. "Pulsed terahertz tomography". In: *Journal of Physics D: Applied Physics* 37.4 (2004), R1.

[103] Tze-An Liu et al. "Wireless audio and burst communication link with directly modulated THz photoconductive antenna". In: *Optics express* 13.25 (2005), pp. 10416–10423.

[104] Lothar Möller et al. "Data encoding on terahertz signals for communication and sensing". In: *Optics letters* 33.4 (2008), pp. 393–395.

[105] Ho-Jin Song and Tadao Nagatsuma. "Present and future of terahertz communications". In: *IEEE transactions on terahertz science and technology* 1.1 (2011), pp. 256–263.

[106] Tadao Nagatsuma, Guillaume Ducournau, and Cyril C Renaud. "Advances in terahertz communications accelerated by photonics". In: *Nature Photonics* 10.6 (2016), pp. 371–379.

[107] Dominic C O'brien et al. "Visible light communications: Challenges and possibilities". In: *2008 IEEE 19th International Symposium on Personal, Indoor and Mobile Radio Communications*. IEEE. 2008, pp. 1–5.

[108] Nicholas Karpowicz et al. "Comparison between pulsed terahertz time-domain imaging and continuous wave terahertz imaging". In: *Semiconductor Science and Technology* 20.7 (2005), S293.

[109] T Kleine-Ostmann et al. "Continuous-wave THz imaging". In: *Electronics Letters* 37.24 (2001), pp. 1461–1463.

[110] Babak Kateb et al. "Infrared thermal imaging: a review of the literature and case report". In: *NeuroImage* 47 (2009), T154–T162.

[111] Brian C Smith. *Fundamentals of Fourier transform infrared spectroscopy*. CRC press, 2011.

[112] Alex Svetlitza et al. "THz measurements and calibration based on a blackbody source". In: *IEEE Transactions on Terahertz Science and Technology* 4.3 (2014), pp. 347–359.

[113] Andrew C Jones and Markus B Raschke. "Thermal infrared near-field spectroscopy". In: *Nano letters* 12.3 (2012), pp. 1475–1481.

[114] Laurent Vabre, Arnaud Dubois, and A Claude Boccara. "Thermal-light full-field optical coherence tomography". In: *Optics letters* 27.7 (2002), pp. 530–532.

[115] Christopher M Bishop. *Pattern recognition and machine learning*. springer, 2006.

[116] Kevin P Murphy. *Machine learning: a probabilistic perspective*. MIT press, 2012.

[117] Ian Goodfellow et al. *Deep learning*. Vol. 1. MIT press Cambridge, 2016.

[118] Johan AK Suykens and Joos Vandewalle. "Least squares support vector machine classifiers". In: *Neural processing letters* 9.3 (1999), pp. 293–300.

[119] Jerome H Friedman. "Greedy function approximation: a gradient boosting machine". In: *Annals of statistics* (2001), pp. 1189–1232.

[120] William M Bolstad and James M Curran. *Introduction to Bayesian statistics*. John Wiley & Sons, 2016.

[121] Mikhail Belkin et al. "Reconciling modern machine-learning practice and the classical bias–variance trade-off". In: *Proceedings of the National Academy of Sciences* 116.32 (2019), pp. 15849–15854.

[122] Diederik P. Kingma and Max Welling. "Auto-Encoding Variational Bayes". In: *2nd International Conference on Learning Representations, ICLR 2014, Banff, AB, Canada, April 14-16, 2014, Conference Track Proceedings*. Ed. by Yoshua Bengio and Yann LeCun. 2014.

[123] Ian Goodfellow et al. "Generative adversarial nets". In: *Advances in neural information processing systems*. 2014, pp. 2672–2680.

[124] Richard S Sutton, Andrew G Barto, et al. *Introduction to reinforcement learning*. Vol. 135. MIT press Cambridge, 1998.

[125] Jianqing Fan et al. "A theoretical analysis of deep Q-learning". In: *Learning for Dynamics and Control*. PMLR. 2020, pp. 486–489.

[126] John Schulman et al. "Proximal policy optimization algorithms". In: *arXiv preprint arXiv:1707.06347* (2017).

[127] Yann LeCun et al. "Handwritten digit recognition with a back-propagation network". In: *Advances in neural information processing systems*. 1990, pp. 396–404.

[128] Yann LeCun. "1.1 Deep Learning Hardware: Past, Present, and Future". In: *2019 IEEE International Solid-State Circuits Conference-(ISSCC)*. IEEE. 2019, pp. 12–19.

[129] Karen Simonyan and Andrew Zisserman. "Very Deep Convolutional Networks for Large-Scale Image Recognition". In: *3rd International Conference on Learning Representations, ICLR 2015, San Diego, CA, USA, May 7-9, 2015, Conference Track Proceedings*. Ed. by Yoshua Bengio and Yann LeCun. 2015.

[130] Felix A Gers, Jürgen Schmidhuber, and Fred Cummins. "Learning to forget: Continual prediction with LSTM". In: (1999).

[131] Yaqing Wang et al. "Generalizing from a few examples: A survey on few-shot learning". In: *ACM Computing Surveys (CSUR)* 53.3 (2020), pp. 1–34.

[132] Quanshi Zhang, Ying Nian Wu, and Song-Chun Zhu. "Interpretable convolutional neural networks". In: *Proceedings of the IEEE Conference on Computer Vision and Pattern Recognition*. 2018, pp. 8827–8836.

[133] Nariman Farsad and Andrea Goldsmith. "Neural network detection of data sequences in communication systems". In: *IEEE Transactions on Signal Processing* 66.21 (2018), pp. 5663–5678.

[134] Nariman Farsad, Milind Rao, and Andrea Goldsmith. "Deep learning for joint source-channel coding of text". In: *2018 IEEE International Conference on Acoustics, Speech and Signal Processing (ICASSP)*. IEEE. 2018, pp. 2326–2330.

[135] Fabian Mentzer et al. "Conditional probability models for deep image compression". In: *Proceedings of the IEEE Conference on Computer Vision and Pattern Recognition*. 2018, pp. 4394–4402.

[136] Guo Lu et al. "Dvc: An end-to-end deep video compression framework". In: *Proceedings of the IEEE Conference on Computer Vision and Pattern Recognition*. 2019, pp. 11006–11015.

[137] Hengtao He et al. "Deep learning-based channel estimation for beamspace mmWave massive MIMO systems". In: *IEEE Wireless Communications Letters* 7.5 (2018), pp. 852–855.

[138] Chao-Kai Wen, Wan-Ting Shih, and Shi Jin. "Deep learning for massive MIMO CSI feedback". In: *IEEE Wireless Communications Letters* 7.5 (2018), pp. 748–751.

[139] Yuyang Wang, Murali Narasimha, and Robert W Heath. "MmWave beam prediction with situational awareness: A machine learning approach". In: *2018 IEEE 19th International Workshop on Signal Processing Advances in Wireless Communications (SPAWC)*. IEEE. 2018, pp. 1–5.

[140] Tian Wu. "CNN and RNN-based Deep Learning Methods for Digital Signal Demodulation". In: *Proceedings of the 2019 International Conference on Image, Video and Signal Processing*. 2019, pp. 122–127.

[141] Sarunas Kalade, Louise Crockett, and Robert W Stewart. "Using sequence to sequence learning for digital BPSK and QPSK demodulation". In: *2018 IEEE 5G World Forum (5GWF)*. IEEE. 2018, pp. 317–320.

[142] Shuai Ma et al. "Signal demodulation with machine learning methods for physical layer visible light communications: Prototype platform, open dataset, and algorithms". In: *IEEE Access* 7 (2019), pp. 30588–30598.

[143] Jin Li, Min Zhang, and Danshi Wang. "Adaptive demodulator using machine learning for orbital angular momentum shift keying". In: *IEEE Photonics Technology Letters* 29.17 (2017), pp. 1455–1458.

[144] Lanting Fang and Lenan Wu. "Deep learning detection method for signal demodulation in short range multipath channel". In: *2017 IEEE 2nd International Conference on Opto-Electronic Information Processing (ICOIP)*. IEEE. 2017, pp. 16–20.

[145] Tobias Gruber et al. "On deep learning-based channel decoding". In: *2017 51st Annual Conference on Information Sciences and Systems (CISS)*. IEEE. 2017, pp. 1–6.

[146] Eliya Nachmani et al. “Deep learning methods for improved decoding of linear codes”. In: *IEEE Journal of Selected Topics in Signal Processing* 12.1 (2018), pp. 119–131.

[147] Sebastian Dörner et al. “Deep learning based communication over the air”. In: *IEEE Journal of Selected Topics in Signal Processing* 12.1 (2017), pp. 132–143.

[148] Fayçal Ait Aoudia and Jakob Hoydis. “End-to-end learning of communications systems without a channel model”. In: *2018 52nd Asilomar Conference on Signals, Systems, and Computers*. IEEE. 2018, pp. 298–303.

[149] Chunxiao Jiang et al. “Machine learning paradigms for next-generation wireless networks”. In: *IEEE Wireless Communications* 24.2 (2016), pp. 98–105.

[150] Timothy O’Shea and Jakob Hoydis. “An introduction to deep learning for the physical layer”. In: *IEEE Transactions on Cognitive Communications and Networking* 3.4 (2017), pp. 563–575.

[151] Jingye Sun, Fangjing Hu, and Stepan Lucyszyn. “Predicting atmospheric attenuation under pristine conditions between 0.1 and 100 THz”. In: *IEEE Access* 4 (2016), pp. 9377–9399.

[152] SG Porter. “A brief guide to pyroelectric detectors”. In: *Ferroelectrics* 33.1 (1981), pp. 193–206.

[153] Ananth Ranganathan. “The levenberg-marquardt algorithm”. In: *Tutoral on LM algorithm* 11.1 (2004), pp. 101–110.

[154] Hans-Georg Beyer and Hans-Paul Schwefel. “Evolution strategies–A comprehensive introduction”. In: *Natural computing* 1.1 (2002), pp. 3–52.

[155] Tim Salimans et al. “Evolution strategies as a scalable alternative to reinforcement learning”. In: *arXiv preprint arXiv:1703.03864* (2017).

[156] Joel Lehman et al. "ES is more than just a traditional finite-difference approximator". In: *Proceedings of the Genetic and Evolutionary Computation Conference*. 2018, pp. 450–457.

[157] John C Raisbeck et al. "Evolution Strategies Converges to Finite Differences". In: *arXiv preprint arXiv:2001.01684* (2019).

[158] Mohammed Amin Abdullah et al. "Wasserstein robust reinforcement learning". In: *arXiv preprint arXiv:1907.13196* (2019).

[159] *Pyroelectic Infrared Detectors*. Tech. rep. DIAS Infrared Systems. URL: http://www.dias-infrared.com/pdf/basics_eng.pdf.

[160] *Detector Basics*. Tech. rep. InfraTec. URL: https://www.infratec.co.uk/downloads/en/sensor-division/application-notes/application_detector_basics.pdf.

[161] *Advanced LinCMOS rail-to-rail, very low-power operational amplifiers*. Texas Instruments. URL: https://www.ti.com/lit/ds/sgls188b/sgls188b.pdf?ts=1609344120284&ref_url=https%253A%252F%252Fwww.google.com%252F.

[162] *LinCMOS low-power operational amplifiers*. Texas Instruments. URL: https://www.ti.com/lit/ds/slos154b/slos154b.pdf?ts=1609395588953&ref_url=https%253A%252F%252Fwww.google.com%252F.

[163] *OPAx22x High precision, low noise operational amplifiers*. Texas Instruments. URL: https://www.ti.com/lit/ds/symlink/opa227.pdf?ts=1609342958784&ref_url=https%253A%252F%252Fwww.google.com%252F.

[164] *LME-335 Single channel pyroelectric detector*. InfraTec. URL: https://www.infratec.co.uk/downloads/en/sensor-division/detector_data_sheet/infratec-datasheet-lme-335-_.pdf.

[165] *Pyroelectric application library*. Tech. rep. InfraTec. URL: https://s3-eu-central-1.amazonaws.com/centaur-wp/theengineer/prod/content/uploads/2012/11/19155900/application_library.pdf.

[166] Upamanyu Madhow. *Fundamentals of digital communication*. Cambridge University Press, 2008.

[167] Charles Truong, Laurent Oudre, and Nicolas Vayatis. "Selective review of offline change point detection methods". In: *Signal Processing* 167 (2020), p. 107299.

[168] David E Rumelhart, Geoffrey E Hinton, and Ronald J Williams. *Learning internal representations by error propagation*. Tech. rep. California Univ San Diego La Jolla Inst for Cognitive Science, 1985.

[169] Sepp Hochreiter and Jürgen Schmidhuber. "Long short-term memory". In: *Neural computation* 9.8 (1997), pp. 1735–1780.

[170] Abien Fred Agarap. "Deep Learning using Rectified Linear Units (ReLU)". In: *CoRR* abs/1803.08375 (2018). URL: http://arxiv.org/abs/1803.08375.

[171] Warren S Sarle. "Stopped training and other remedies for overfitting". In: *Computing science and statistics* (1996), pp. 352–360.

[172] Wouter M Kouw and Marco Loog. "An introduction to domain adaptation and transfer learning". In: *arXiv preprint arXiv:1812.11806* (2018).

[173] Paul J Werbos. "Backpropagation through time: what it does and how to do it". In: *Proceedings of the IEEE* 78.10 (1990), pp. 1550–1560.

[174] Diederik P. Kingma and Jimmy Ba. "Adam: A Method for Stochastic Optimization". In: *3rd International Conference on Learning Representations, ICLR 2015, San Diego, CA, USA, May 7-9, 2015, Conference Track Proceedings*. Ed. by Yoshua Bengio and Yann LeCun. 2015.

[175] Fangjing Hu and Stepan Lucyszyn. "Emerging thermal infrared 'THz Torch' technology for low-cost security and defence applications". In: *THz and Security Applications*. Springer, 2014, pp. 239–275.

[176] Erik Bründermann, Heinz-Wilhelm Hübers, and Maurice FitzGerald Kimmitt. *Terahertz techniques*. Vol. 151. Springer, 2012.

[177] Hang Ren, Sang-Hee Shin, and Stepan Lucyszyn. "Enhanced cognitive demodulation with artificial intelligence". In: *Scientific Reports* 10.1 (Nov. 2020), p. 20298. ISSN: 2045-2322. DOI: 10.1038/s41598-020-77262-0. URL: https://doi.org/10.1038/s41598-020-77262-0.

Appendix A: Code Overview

The code review for the 'THz Torch' software is organized according the software diagram in Figure 3.3. Code files are mapped to the transceiver blocks in Figure 3.3. The function of each code file will be briefly introduced. Declarations and comments for functions implemented in each file are also provided.

THz Torch Transmitter

File name	Description	Functions
bulb_driver_ir.ino corresponding to block: **Modulator Driver on Arduino**	Driver for Arduino Due	• **void** calibrate(void): use optical shutter and thermal emitter to generate step radiation. • **void** send_frame(byte frame[], unsigned int len): switch thermal emitter according to the sent data frame. • **void** send_bit(byte x): switch thermal emitter according to the sent symbol (bit). • **void** setup(): initialize all devices and shake hand with the Tx User Interface. • **void** loop(): receive command from Tx User Interface, execute the command and send reply message.
THzTransmitter.py corresponding to block: **Tx User Interface**	Transmitter user interface and encoder	• **def** _com_read(self): read reply message from Arduino Due. • **def** _com_write(self, raw_str): send command to Arduino Due. • **def** send_data(self, frame): send data frame command to Arduino Due. • **def** send_calibration(self): send calibration command to Arduino Due. • **def** send_bitrate(self, br): send new symbol rate to Arduino Due. • **def** __init__(self, com='/dev/tty.usbmodem14101'): initialize USART, shake hand with Arduino Due. • **def** main(): receive user input and send corresponding commands.

THz Torch Receiver

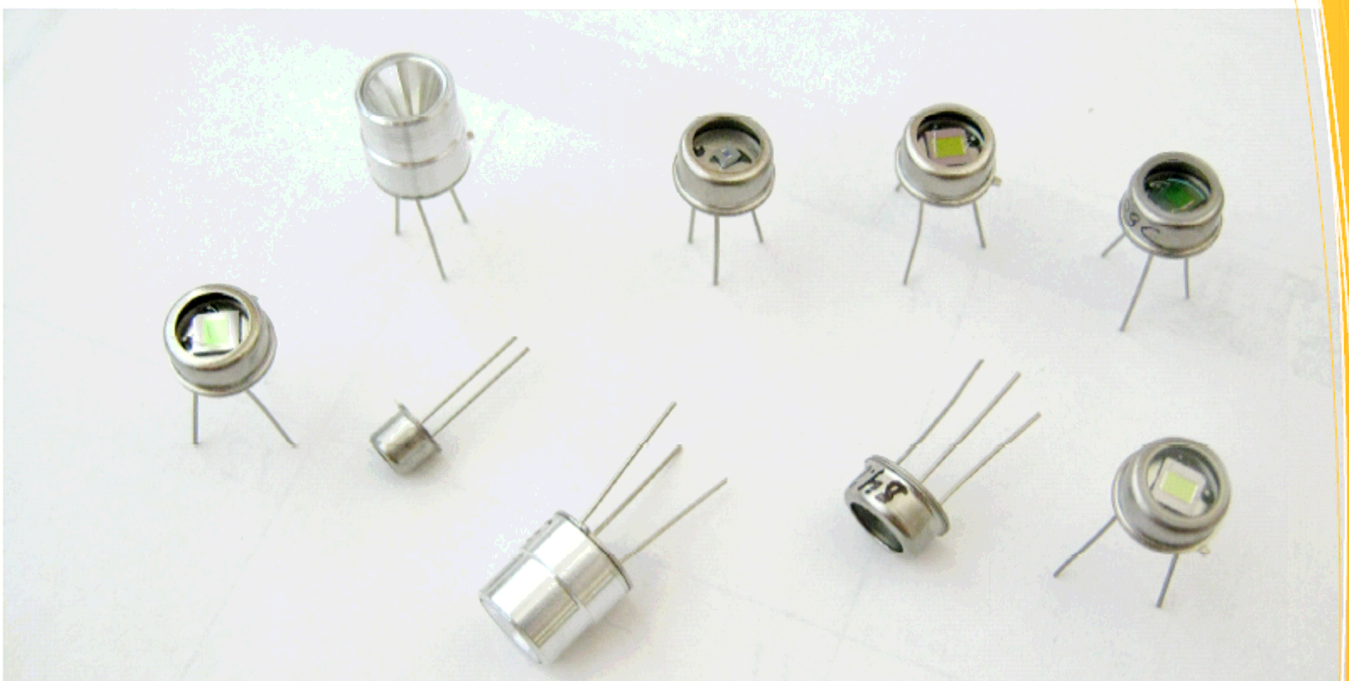
File name	Description	Functions
ThzReceiver.py corresponding to block **Rx User Interface**	Top level receiver and user interface	• **def** __init__(self, fs, bit_rate, frame_header, frame_bits, channel_id, channel_range, version): initialize the receiver with input configurations. • **def** console(self): receive user input and send corresponding commands to receiver • **def** start(self): create receiver building blocks in separate processes (including console, ADC, synchronizer, estimator and demodulator); create queues for inter-process communications.
NiAdc.py corresponding to block **ADC Interface**	Interface for NI ADC	• **def** __init__(self, device='Dev1', ch='ai0', vmax=2.0, sample_freq=1E3, event_freq=1E2): Initialize the ADC with input configurations. • **def** EveryNCallback(self): read sampled signal into an internal ADC buffer and send it to the synchronizer through a queue.
Synchronizer.py corresponding to block **Synchronizer**	Implementation of timing synchronizing algorithms and send synchronized signal to demodulator and calibrator.	• **def** __init__(self, sample_freq=1e3, mode='data'…): initialize the synchronizer with input configurations. • **def** _synchronizer(self): receive command from ThzReceiver and switch itself between different modes. • **def** get_v_header(self): receive feedback from calibrator. • **def** cal_synchronizer(self): timing synchronization for calibration signals; send result to the calibrator. • **def** frame_synchronizer(self): timing synchronization for data frame signals; send result to the demodulator. • **def** align_by_cpd(self, s1, s2): improved timing synchronization with extra change-point-detection phase.
Demodulator.py corresponding to blocks:	Implementation of channel estimator and demodulation algorithms.	• **def** __init__(self, header_queue, sample_freq=1e3…): initialize the demodulator and calibrator with input parameters. • **def** demodulate(self): receive commands and synchronized signals from the

Channel Estimator and Demodulator		synchronizer and invoke corresponding subroutines. • **def** tx_cal_demodulate(self, frame, num_iter=15, npop=20, alpha=1e-2): calibrate the thermal emitter parameters using the first-order ES algorithm. • **def** tx_cal_demodulate_new(self, frame, num_iter=10, npop=30, alpha=2e-2, order=2, sigma=0.1): calibrate the thermal emitter parameters using the second-order ES algorithm. • **def** tx_cal_fd(self, frame, num_iter=10, alpha=30.0, order=1): calibrate the thermal emitter parameters using the finite-difference algorithm. • **def** header_update(self): send feedback data to the synchronizer. • **def** cal_demodulate(self, frame): calibrate the pyro sensor parameters. • **def** record_demodulate(self, frame, save_to=None): record the data for offline experiements. • **def** sample_params(self): sample random system parameters. • **def** simulate_frame(self, n_frame, save_to, add_noise=True): simulate data frame with artificial noise for neural network training. • **def** data_demodulate(self, frame, display=True): demodulate data frame with template-matching based algorithms. • **def** offline_data_demodulate(self, datafile, path): demodulate signals saved in a local file. • **def** sequence_matching(self, vr, v1, v0, mode='mf'): implementation of naïve template-matching and matched filter for demodulation. • **def** bit_predict(self, t, T0, v0, dvdt0, We, ke, Ce, dt=1e-4, torch_solver='ode', pyro_params=None): predict the expected noiseless signal given system parameters, initial conditions and thermal emitter input power. • **def** torch_ode(self, T, t, We, ke, Ce): the thermodynamics of the emitter.

		• **def** torch_ode_series_solv(self, t, T0, We, ke, Ce, order=3): power series approximation to the torch_ode solution. • **def** torch_ode_piecewise_series_solv(self, t, T0, We, ke, Ce, order=3, piece=3e-3): piecewise power series approximation to the torch_ode solution. • **def** get_channel_info(self): read channel metadata from file. • **def** planck_equ(self, wl, T): planck equation. • **def** get_rx_power(self, T, integrate_method='trapz'): estimate the received radiation power. • **def** get_normalized_rx_power_func(self, dT=0.5): estimate the normalized received radiation power. • **def** pyro_v_step(x, p0, p1, p2, p3): the closed-form step response of the sensor. • **def** pyro_ode(self, x, t, dpdt, pyro_params=None): the thermodynamics of the sensor.

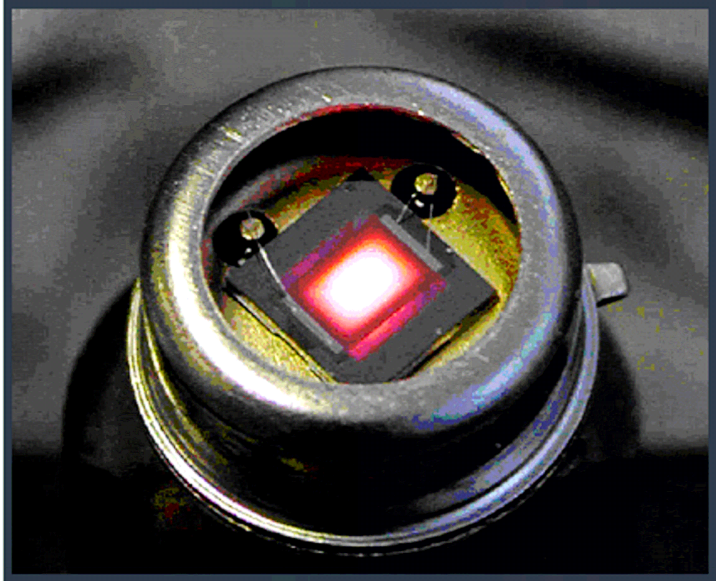
Appendix B: Thermal Emitter Datasheet

The datasheet of the thermal emitter used in our 'THz Torch' wireless links is appended here for reference.



Silicon MEMS Optical Technology

Infrared Emitters



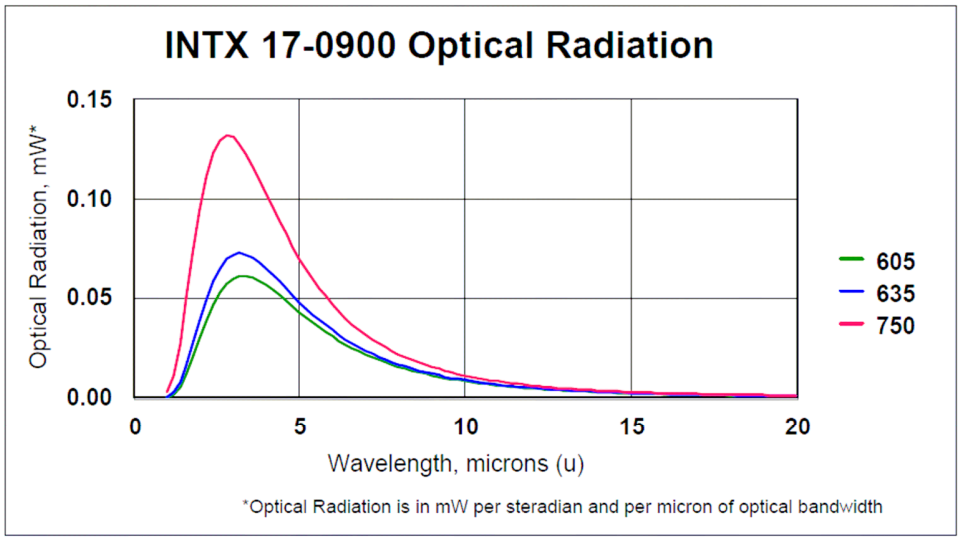
Electronic modulation to 140 Hz

750 C maximum operating temperature

2 ohm hot – cold resistance change

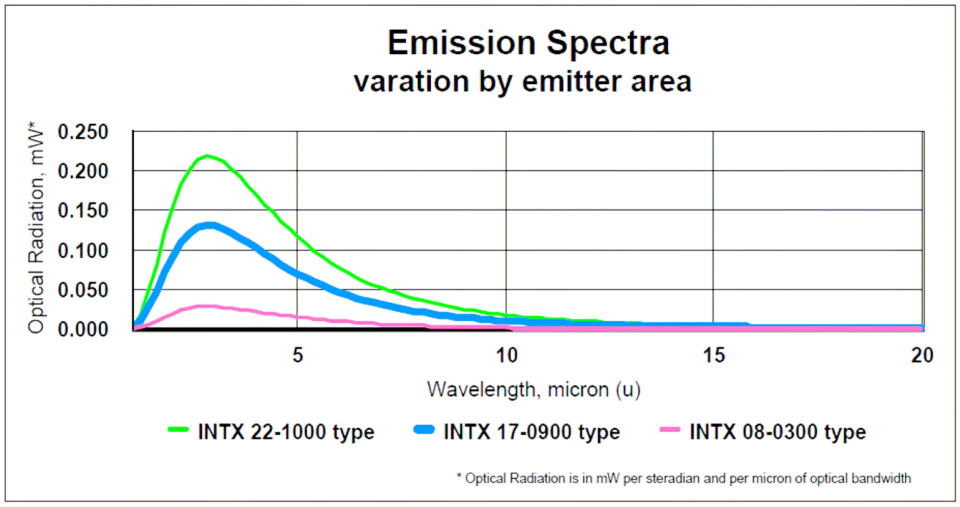
Emission Spectra and Temperature

Intex's pulsed infrared (IR) light sources are thermal sources emitting infrared energy over a wavelength range of 1-20 microns. The energy output at each wavelength is given by Planck's law so the optical energy density at any wavelength is known based on the temperature, size and emissivity of the emitter. All Intex Emitters are designed and specified to operate up to 750° C. Operation at lower temperatures is possible. Many present applications are operating at 605° C. The graph below shows the optical radiation delivered by the INTX 17-0900 series when operated from 605° C to 750° C. Notice that the peak emission shifts slightly to shorter wavelengths as the temperature increases. However, a higher temperature delivers a higher energy output at all wavelengths.



Emission Spectra and Area

Intex's pulsed infrared (IR) light sources have three different emitting area sizes. Increasing membrane area gives increased optical output and a small increase in input power. Plotted below is the energy output from the different size emitters operating at 750° C. The output at every wavelength is affected the same by a change in emission area. Selecting the proper size device is a matter of system optical aperture, S/N ratio desired and energy available to power the emitter.



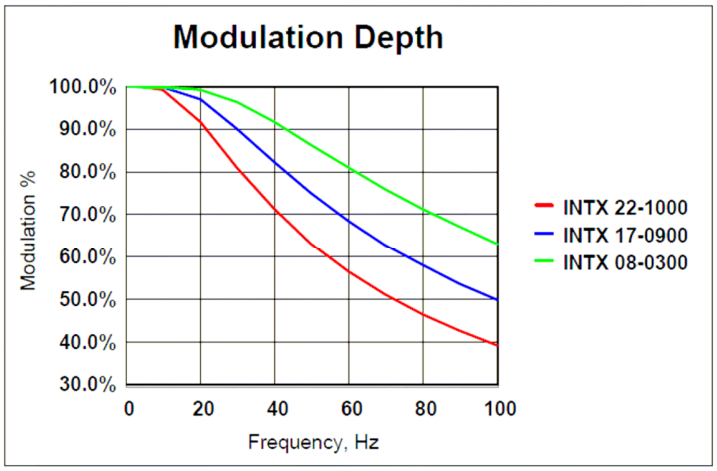
Modulation Depth

The thermal time constant of the Emitter's membrane is the time it takes to heat and cool one complete cycle. This time constant restricts how much the device will modulate when electrically "chopped". It is an exponential function described by the equation:

$$dT = dT_o \exp(-T/Tau)$$

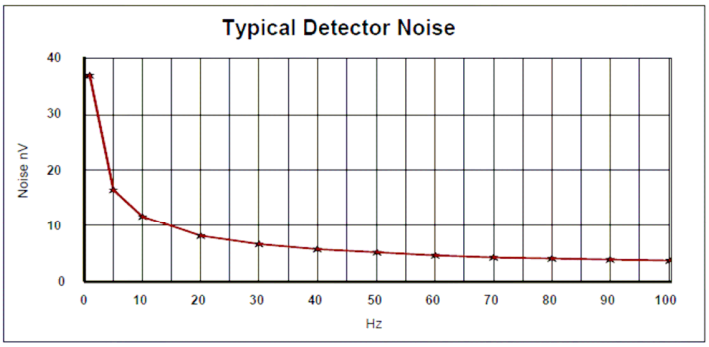
dT = membrane temperature at time T
dT_o = membrane temperature at time Zero
T = time since Zero
Tau = thermal time constant

One feature of the Intex technology, Vs. typical competitors, is a low thermal time constant which results in high modulation depth at high chopping frequencies.



The "slowest" Intex part INTX 22-1000 can be chopped at up to 70 Hz before the modulation depth goes below 50%. The fastest, INTX 08-0300 can be electronically chopped up to 140 Hz. with modulation above 60%.

High chopping frequencies can improve system Signal to Noise ratio (S/N) by overcoming detector 1/f noise. Consider a popular thermopile detector that has a noise specification of 37 nV/ Sqrt Hz. Operating at 40 Hz as opposed to 5 Hz will lower the noise figure from 16.5 nV to 5.8 nV .

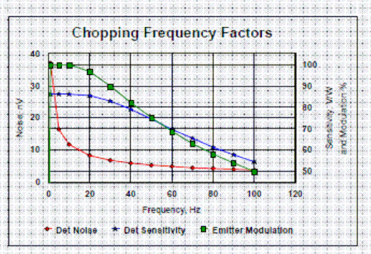


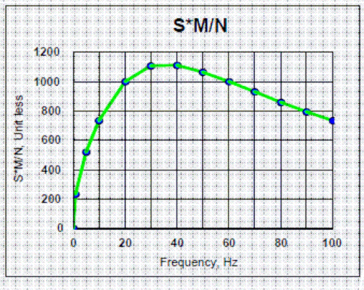
Optimal Chopping Frequency

System designers need to balance electronic chopping frequency with emitter modulation depth, detector sensitivity and detector noise level which all decrease with increasing chopping frequency, but not at the same rate. The optimum electronic chopping frequency is chosen to maximize signal-to-noise ratio.

An approach to optimizing the chopping frequency is to generate a unit-less function, the product of detector sensitivity and emitter modulation depth divided by detector noise floor. That function will peak near the optimal operating frequency.

A typical case using the INTX 17-0900 emitter and a thermopile detector with a noise figure of 37 nV/ sqrt Hz and a detector response time constant of 10 mS yields an optimal chopping rate near 40 Hz, graphed below.





	INTX 17-0900			INTX 22-1000			INTX 08-0300 Preliminary		
Description	**Basic Product**			**Larger Area and Power**			**Small Area with Lower Power 2.5 Volt Drive**		
Thermal Time Constant	14.4 mS typ.			20.0 mS typ.			10.0 mS typ.		
Operating Temperature	605° C Typical / 750° C Max.								
Heated Membrane Area	2.89 mm^2 1.7x1.7 mm			4.80 mm^2 2.2 X 2.2 mm			0.64mm^2 0.8 X 0.8 mm		
Drive Power, mW	690 Typical /900 Max.			767 Typical / 1,000 Max.			230 Typical / 300 Max.		
Emissivity	.80						.90		
Spectral Range	1 – 20 microns typical								
Modulation Frequency	1-100 Hz. Typical						1-200 Hz. Typical		
Frequency at 50% Modulation	100 Hz.			70 Hz.			140 Hz.		
Resistance at Operating Temperature (750 C) ohms	**Min.**	**Typical**	**Max.**	**Min.**	**Typical**	**Max.**	**Min.**	**Typical**	**Max.**
	40	50	60	35	45	55	16	21	26
Resistance at Room Temperature (25 C) ohms	48 Typical			43 Typical			14 Typical		
Drive Voltage at Operating Temperature (750 C) volts	5.9 Typical / 6.7 Max.			5.9 Typical / 6.7 Max.			2.2 Typical / 2.5 Max.		
Drive Current at Operating Temperature (750 C) mA	117 Typical / 134 Max.			130 Typical / 149 Max.			105 Typical / 120 Max.		
Average Lifetime, at 10 Hz, 50% duty cycle	100,000 hrs at 605° C 5,000 hrs at 750° C						TBD		
Package	**Type Code - P**			**ANSI #**			**Type Code - P**		**ANSI #**
	1			TO-5			3		TO-18
	2			TO-39					

A Range of Emitters

The INTX 17-0900 was our first emitter, introduced in 2005. With an emission area of 1.7 mm X 1.7mm and a 900 mW maximum drive power it is still very popular.

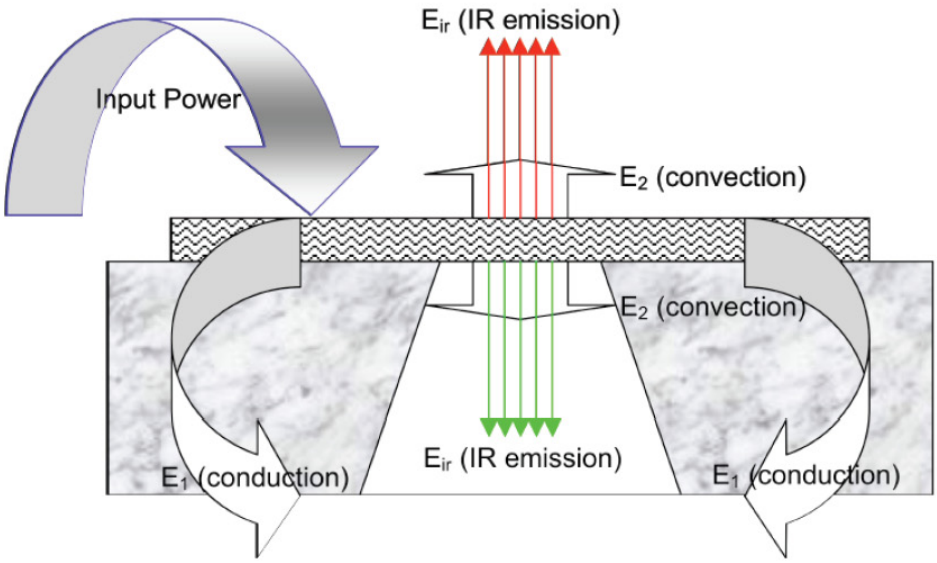
In response to requests for more power, for instance to illuminate larger detector arrays, the INTX 22-1000 was developed. It's emission area is 2.2 mm X 2.2 mm and it has a maximum drive power of 1000 mW.

In 2011, a 5.0 Volt version of the INTX 22-1000 is planned to accommodate single supply systems.

In response to requests for low-cost, low-power devices, we are also developing the model INTX 08 -0300. With a smaller 0.8 mm X 0.8 mm emission area, it has a maximum power consumption of only 300 mW. Drive voltage will be typically 2.2-2.5 volts. This device is targeted at high-volume potentially battery-powered, sensor devices.

Various optical windows as well as reflector options are available.

Power Dissipation of the Infrared Emitter



The power E_0, input electrically, is dissipated by the Emitter in three ways,

$$\mathbf{Eo = Eir + E_1 + E_2}$$

Eir =infrared radiation, the desired optical output of the emitter
E_1 = conduction through the silicon substrate, wasted energy
E_2 = convection through air, wasted energy

The magnitude of the infrared radiation is a function of the surface area, emissivity and temperature.

$$\mathbf{Eir = € \cdot £ \cdot T^4 \cdot A}$$

€ = emissivity of the surface, typically 0.8 in Intex Emitters
£ = $5.67 \cdot 10^{-8}$ [$W \cdot m^{-2} \cdot K^{-4}$]
T = Kelvin Temperature, typically 1023° K , (750° C max) in Intex Emitters
A = Area of the emitting surface, $meter^2$, $2.89 \cdot 10^{-6}$ in INTX 17-0900

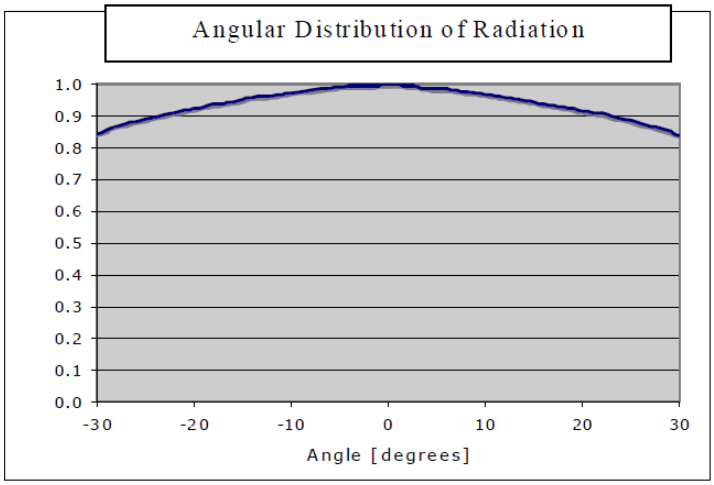
Eir = 144 mW, per side of the emitter

Typically the backside radiation is not projected toward the detector array and it contributes to wasted heat. For calculation purposes we lump this wasted energy into the conduction losses. Typical power dissipation is shown below. Notice 16% is converted into useful, forward projected, optical infrared radiation.

Typical Power Dissipation of an INTX 17-0900 type emitter at 750° C		
Input Power	900 mW	100%
Eir – Radiation power (forward)	144 mW	16%
E_1 – Conduction and rear surface radiation loss	215 mW	24%
E_2 – Convection loss	541 mW	60%

Angular Distribution of Radiation

The Intex Emitter has a flat surface and from that surface the angular distribution of the radiation follows a cosine function, peaking at normal incidence.

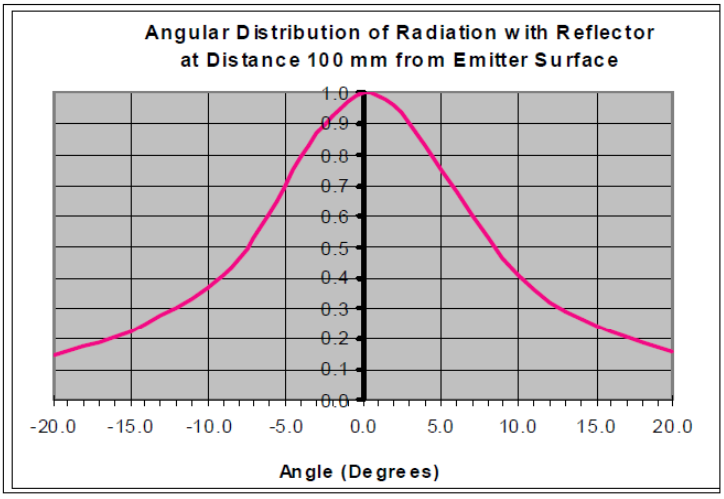


Some system designs cannot locate the detector plane very close to the emitter and a significant amount of energy falls outside of the detector collection "field of view".

To improve the energy collimation, Intex offers a parabolic reflector option that can be fitted to the emitters.



With the reflector the Emitter's energy is kept within a much tighter solid angle. The distribution of an INTEX source with a parabolic reflector is shown below.



Options

Intex Emitters are rugged and are typically operated exposed to ambient atmosphere. Intex can provide Emitters with windows which can help define a sample compartment in certain applications. Window materials available are:

Calcium Fluoride
Sapphire
Barium Fluoride
Antireflective Coated Silicon

Some system integrators want even more flexibility in packaging. Available configurations are:

TO-5
TO-39
TO-18

Surface mounted Emitters can be supplied under special order.

The ultimate in low overhead packaging is DIE. We can supply cut or wafer level.

To assist customers in getting project concepts proven, and our components "designed in", we offer limited in house feasibility modeling and proof of principal prototyping. It is our goal to be of assistance throughout the entire product life cycle.

Please contact us to discuss your project.

State of the Art Technology

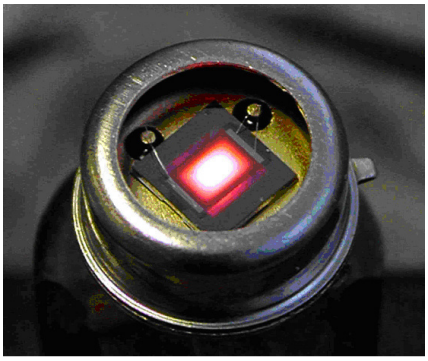
Intex's unique quasi-black body pulsed infrared (IR) light sources can operate at higher frequencies and temperatures than the competition, delivering higher Signal to Noise Ratio in your application.

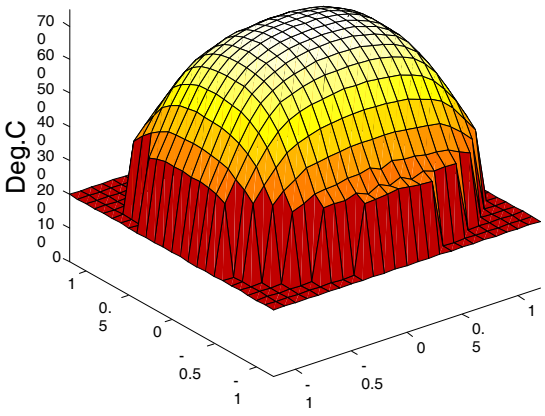
The Sources are made of patented, thin-membrane thermo resistive elements using MEMS technology at lower costs.

Modulation of the light output is achieved by modulating the input electrical power, eliminating the need for optical choppers and allowing precise control over the output spectral range in critical applications.

The temperature distribution of a membrane is shown in the figures below where the temperature in the center is 750°C, the maximum operating temperature.

The nanostructure carbon membrane defines the emission area and overlaps a silicon frame. The radiant area of the membrane is responsible for the spectral emission described by Planck's Equation.





www.intexworld.com

Document: MKT 2001 IR Emitters Rev A2 paged
Copyright 2011 Intex inc.

Appendix C: Pyroelectric Sensor Datasheet

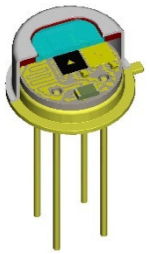
The datasheet of the pyroelectric sensor used in our 'THz Torch' wireless links is appended here for reference.

LME-335-#

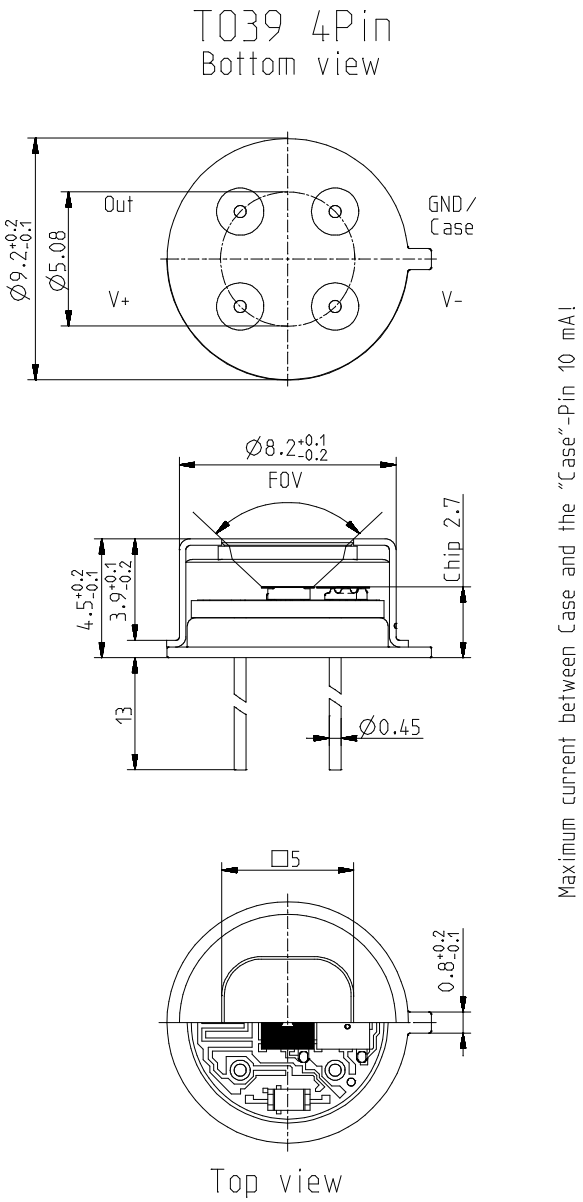
Single channel pyroelectric detector

Description:

single channel; TO39 housing; medium chip size; thermal compensation; low Micro; OpAmp; current mode; feedback 100 GOhm;

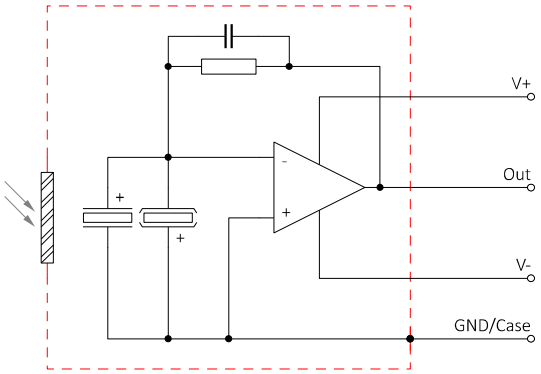


Housing:

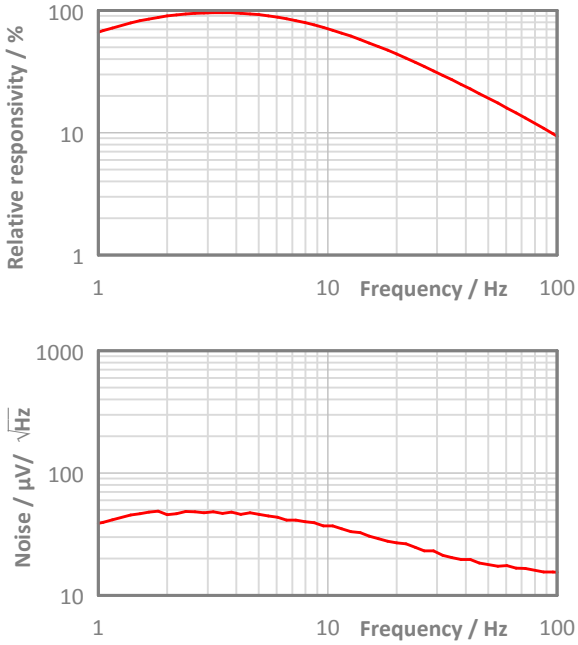


Maximum current between Case and the "Case"-Pin 10 mA!

Pin Assigment:

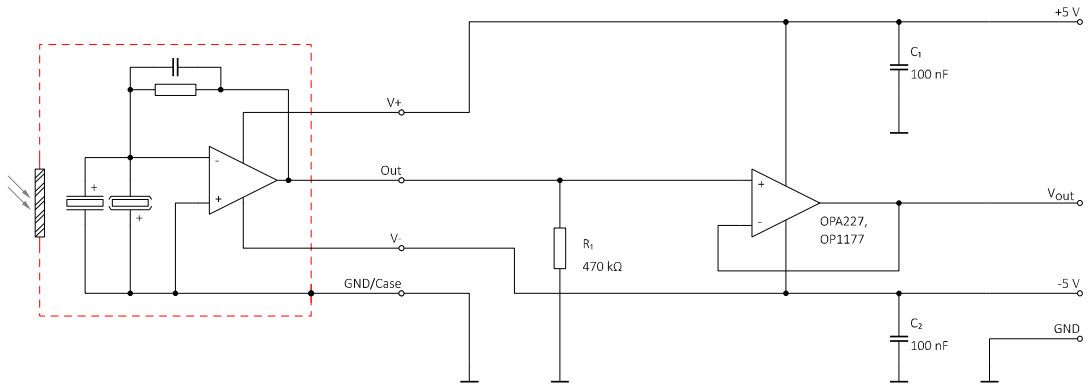


Frequency Response:



InfraTec GmbH
Infrarotsensorik und Messtechnik
Dresden / GERMANY
www.InfraTec.de

Test Circuit:



Parameters:

Aperture size	nom	□ 5.0 mm
Element size / type	nom	2.0 × 2.0 mm² lithium-tantalate with black layer
Thermal time constant	typ	150 ms
Feedback resistor	nom	100 GΩ ±20 %
Feedback capacitor	nom	0.2 pF ±0.1 pF
Polarity	nom	Negative signal by positive IR flux change
Voltage responsivity (rms) {500 K, 10 Hz, 25 °C, without filter/window}	min	85,000 V/W
Noise density (rms) {10 Hz, BW 1 Hz, 25 °C}	max	45 µV/√Hz
Detectivity {500 K, 10 Hz, 1 Hz, 25 °C, without filter/window}	typ	6.0E+08 cm√Hz/W
Acceleration response {5 ... 200 Hz}	typ	300 µV/g; g = 9.81 m/s²
CMOS operational amplifier	nom	OpAmp2
Supply voltage V+ - V-	max	16 V
Operating supply voltage V+ / V-		+2.2 ... 8.0 V / -2.2 ... -8.0 V
Recommended supply voltage V+ / V-	nom	V+ = +5 V; V- = -5 V
Supply current {output load 1 MΩ}	max	150 µA
Offset voltage {25 °C; output load 1 MΩ}		-5 mV ... +5 mV
Optimal output load	nom	470 kΩ
Absolute output current	max	±0.4 mA
Operating / Storage temperature	nom	-40 ... +85 °C
IR filter		All InfraTec windows and filters are available (except KBr and CsI). Customized filters upon request.
Filter sizes	nom	Rectangular filters: (5.25 × 5.25) mm +0/-0.05 mm Circular filters: ø6.5 mm ±0.1 mm Standard thickness: 0.50 mm +0.2/-0.1 mm Thickness range 0.70 ... 1.10 mm on request
Field of View	min	CaF2 or BaF2; 0.4 mm thick: 80° Silicon substrate; 0.5 mm thick: 90°

InfraTec reserves the right to change these specifications at any time without notification.